Modulation of the sphingolipid metabolism with the sphingosine kinase inhibitor SKI-II to overcome hypoxia-induced chemotherapy resistance in glioblastoma cells

Dissertation

Zur Erlangung des Grades

Doktor der Naturwissenschaften

Am Fachbereich Biologie

Der Johannes Gutenberg-Universität Mainz

Nádia Sousa Menk

Geb. am 14.12.1989 in Seixal (Portugal)

Mainz, den 26.01.2022

Dekan: Prof. Dr. Eckhard Thines
Institut für Molekulare Physiologie
Johannes Gutenberg-Universität Mainz

1. Berichterstatter: PD Dr. Anne Régnier-Vigouroux
Institut für Entwicklungsbiologie und Neurobiologie
Johannes Gutenberg-Universität Mainz

2. Bericherstatter: Prof. Dr. Christian Behl
Institut für Pathobiochemie
Universitäts-medizin der Johannes Gutenberg-Universität Mainz

Tag der mündlichen Prüfung:

This work was supported by a doctoral fellowship awarded to me by the
Bischöfliche Studienförderung Cusanuswerk

Abstract

Glioblastoma patients commonly develop resistance to temozolomide (TMZ) chemotherapy. Tumor hypoxia, which supports chemotherapy resistance, favors the expansion of glioblastoma stem cells (GSCs), contributing to tumor relapse. Because of a deregulated sphingolipid metabolism, glioblastoma tissues contain high levels of the pro-survival sphingosine-1-phosphate (S1P) and low levels of the pro-apoptotic ceramide. Ceramide can be metabolized to S1P by sphingosine kinase (SK) 1 that is overexpressed in glioblastoma. Thus, blocking SK might prevent this conversion and support the efficacy of TMZ. The small molecule SKI-II inhibits SK and dihydroceramide desaturase 1, which converts dihydroceramide to ceramide. Previous studies from the laboratory of Anne Régnier-Vigouroux reported that SKI-II combined with TMZ induces caspase-dependent cell death, preceded by dihydrosphingolipids accumulation and autophagy in normoxia. In the present study, I investigated the effects of a lower dose combination of TMZ and SKI-II under normoxia and hypoxia in human glioblastoma cells and patient-derived GSCs.

I observed that TMZ resistance of glioblastoma cells was increased under hypoxia. However, combination of TMZ (48 µM) and SKI-II (2.66 µM) synergistically inhibited glioblastoma cell growth and potentiated glioblastoma cell death relative to single treatments under hypoxia. This lower dose combination did not induce dihydrosphingolipids accumulation, but a decrease in ceramide and its metabolites. It induced oxidative and endoplasmic reticulum stress and triggered caspase-independent cell death. It impaired the self-renewal capacity of TMZ-resistant GSCs, particularly under hypoxia. Furthermore, it decreased invasion of glioblastoma cell spheroids.

This study provides novel insights on the interplay between the sphingolipid metabolism and invasion, a hallmark of cancer, and cancer stem cells, key drivers of cancer. It demonstrates the therapeutic potential of approaches that combine modulation of sphingolipid metabolism with first-line agent TMZ in overcoming tumor growth and relapse by reducing hypoxia-induced resistance to chemotherapy and by targeting both differentiated and stem-like glioblastoma cells.

Zusammenfassung

Glioblastom-Patienten entwickeln häufig eine Resistenz gegen eine Temozolomid (TMZ)-basierte Chemotherapien. Die im Tumor vorherrschenden hypoxischen Bedingungen unterstützen die Chemotherapieresistenz und begünstigen die Expansion von Glioblastom-Stammzellen (GSCs), wodurch die Wahrscheinlichkeit eines Rezidivs erhöht wird. Aufgrund eines deregulierten Sphingolipidstoffwechsels enthält das Glioblastomgewebe hohe Konzentrationen des überlebensfördernden Metabolits Sphingosin-1-Phosphat und niedrige Konzentrationen pro-apoptotischer Ceramide. Ceramide können durch das Enzym Sphingosinkinase (SK) 1 zu Sphingosin-1-phosphat (S1P) metabolisiert werden, weshalb eine Inhibition von SK, und somit der Umwandlung von Ceramiden zu S1P, die Wirksamkeit von TMZ unterstützen könnte. Das kleine Molekül SKI-II hemmt SK und die Dihydroceramid-Desaturase 1, die Dihydroceramid in Ceramide umwandelt. Frühere Studien aus dem Labor von Anne Régnier-Vigouroux belegen, dass SKI-II in Kombination mit TMZ unter normoxischen Bedingungen einen Caspase-abhängigen Zelltod induziert, dem eine Akkumulation von Dihydrosphingolipiden und Autophagie vorausgeht. In der vorliegenden Arbeit werden die Auswirkungen einer niedrig dosierten Kombination von TMZ und SKI-II unter normoxischen und hypoxischen Bedingungen in humanen Glioblastomzellen und patienteneigenen GSC beschrieben.

Ich beobachtete, dass die TMZ-Resistenz von Glioblastomzellen unter Hypoxie erhöht war. Die Kombination von TMZ (48 µM) mit SKI-II (2,66 µM) hemmte jedoch synergistisch das Wachstum von Glioblastomzellen und potenzierte deren Zelltod im Vergleich zu Einzelbehandlungen unter Hypoxie. Diese niedrigere Dosiskombination induzierte keine Akkumulation von Dihydrosphingolipiden, sondern eine Abnahme von Ceramiden und seinen Metaboliten. Die Kombination induzierte oxidativen und endoplasmatischen Retikulumstress und löste den Caspase-unabhängigen Zelltod aus. Außerdem verminderte sie die Selbsterneuerungsfähigkeit von TMZ-resistenten GSCs, insbesondere unter Hypoxie. Darüber hinaus verringerte sie die Invasion von Glioblastom-Zellsphäroiden.

Diese Studie liefert neue Einblicke in das Zusammenspiel zwischen dem Sphingolipidstoffwechsel und der Invasionskapazität von Krebsstammzellen, den wichtigsten Treibern von Krebs. Außerdem demonstriert sie das therapeutische Potenzial von Ansätzen, die die Modulation des Sphingolipidstoffwechsels mit dem Erstlinienwirkstoff TMZ kombinieren, um Tumorwachstum und -rückkehr zu überwinden, indem sie die Hypoxie-induzierte Resistenz gegen Chemotherapie reduzieren und sowohl differenzierte als auch stammzellartige Glioblastomzellen ansprechen.

Table of Contents

1. INTRODUCTION

1.1. Classification of diffuse gliomas

Gliomas or the so-called “diffuse gliomas” comprise astrocytic and oligodendroglial tumors of the central nervous system (CNS) that typically infiltrate extensively in the neuropil, i.e. “the network of neuronal and glial cell processes in grey and white matter” [1]. In 2016, the World Health Organization (WHO) established a new classification of CNS tumors based on combined phenotypic and genotypic diagnostics. More specifically, it relies on histological evaluation and the presence of genetic mutations in the isocitrate dehydrogenase (IDH) 1/2 genes, and in the case of pediatric diffuse gliomas, K27M mutations in the histone H3 gene H3F3A (diffuse midline glioma). In this new classification, diffuse gliomas are categorized as: WHO grade II and III astrocytic tumors; grade II and III oligodendrogliomas; and grade IV glioblastomas and diffuse midline gliomas [2] (more detail in Table 1). The grading scheme of tumors (from I to IV) provides a malignancy scale, where IV represents the highest grade of malignancy, but also influences the decision on the therapeutic protocols and predicts patient prognosis [3].

Table 1 *- Grading of diffuse astrocytic and oligodendroglial tumors according to the 2016 World Health Organization Classification of Tumors of the Central Nervous System (adapted from [4])*

Diffuse Astrocytic and Oligodendroglial Tumors	Grade
Diffuse astrocytoma, IDH mutant	II
Anaplastic astrocytoma, IDH mutant	III
Glioblastoma, IDH-wildtype	IV
Glioblastoma, IDH-mutant	IV
Diffuse midline glioma, H3 K27M-mutant	IV
Oligodendroglioma, IDH-mutant and 1p/19q-codeleted	II
Anaplastic oligodendroglioma, IDH-mutant and 1p/19q-codeleted	III

1.2. Glioblastoma

According to the WHO 2016 classification, glioblastomas (GBs) are subdivided into GB IDH-wildtype, which corresponds to most cases (about 90%), and GB IDH-mutant. GB IDH-wildtype

is defined as primary GB, as it occurs without previous evidence of a less malignant precursor lesion and arises in patients over 55 years of age. GB IDH-mutant is defined as secondary GB, as it progresses from low-grade diffuse astrocytoma or anaplastic astrocytoma and occurs mostly in younger patients. The presence of necrosis and microvascular proliferation are hallmarks of glioblastoma (Figure 1). Secondary GBs present a lesser degree of necrosis and contain areas with oligodendroglioma-like components more frequently than in primary GBs[5]. People with secondary GB have a significantly longer mean overall survival (OS) (31 months *vs* 15 months) [6].

The statistical report on primary brain and other CNS tumors diagnosed in 2012–2016 from the Central Brain Tumor Registry of the United States (CBTRUS), stated GB has "the third most frequently reported CNS histology and the most common malignant tumor overall". GB accounted for 14.6% of all primary brain and other CNS tumors, 48.3% of primary malignant brain tumors and 57.3% of all gliomas. GB is most common in older adults (median age at diagnosis is 65 years old), particularly in White males. In children and adolescents (0-19 years of age), GB accounts for 3% of all brain and CNS tumors. The average annual age-adjusted incidence rate for GB is of 3.22 per 100,000 population in the US [7].

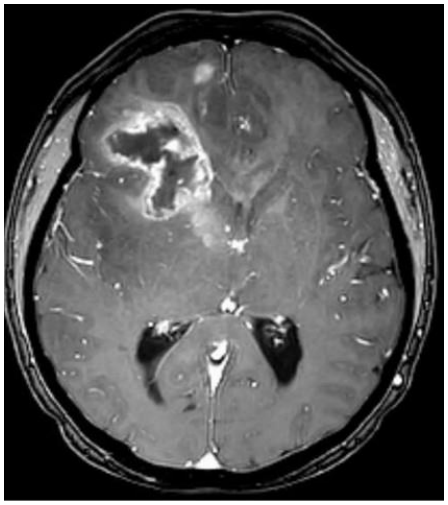

Figure 1 *- Brain MRI (magnetic resonance imaging) with T1-weighted contrast-enhanced (T1CE) showing a glioblastoma in the right frontal lobe* [8]*. Note the heterogeneous irregular peripheral enhancement with a central non-enhancing area, consistent with necrosis.*

1.2.1. IDH mutations and DNA hypermethylation

The human IDH protein is present in three isoforms: IDH1, IDH2 and IDH3. IDH1 is present in the cytoplasm and peroxisomes, whereas IDH2 and IDH3 are present in the mitochondria. IDH1 and IDH2 share a high degree of sequence similarity (70% in humans) and catalyze identical reactions [9]. Among other reactions and cellular functions, these enzymes catalyze the oxidative decarboxylation of isocitrate to form α-ketoglutarate (α-KG) using NADP+ as a cofactor to generate NADPH.

Mutations in the IDH1/2 genes have been associated with an improved prognosis in GB. The most frequent IDH1 and IDH2 mutation is R132H (83% to 91%) and R172K, respectively [6]. Mutations in the IDH3 gene are rare in GB [10]. IDH1/2 mutations are gain-of-function mutations that not only reduce the enzyme's ability to produce α-KG, but also increase the production of 2-hydroxyglutarate (2HG) from the NADPH-dependent reduction of α-KG (Figure 2).

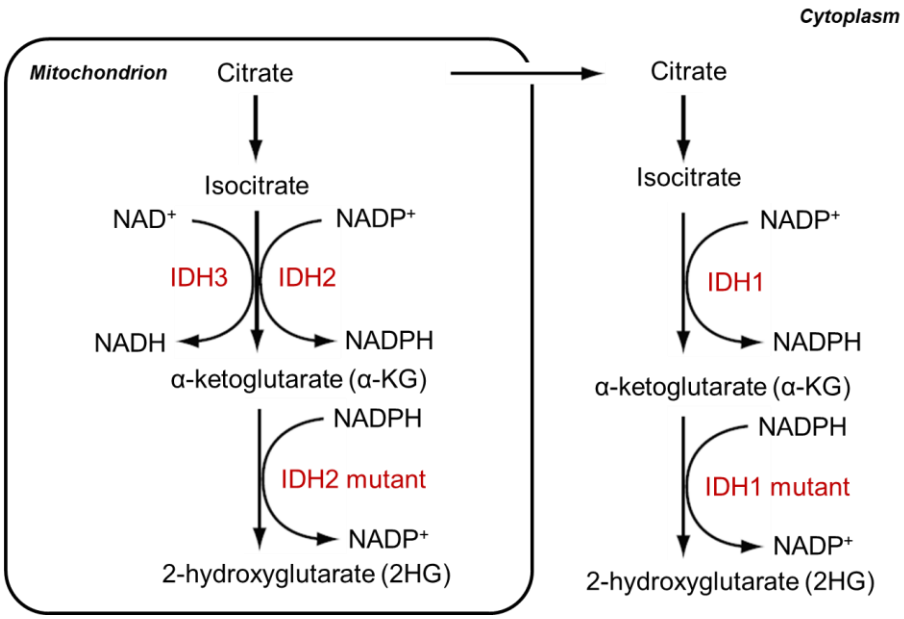

Figure 2 *- Neomorphic enzyme activity of mutant IDH1/2 enzymes. Wild-type (WT) IDH1/2 catalyzes the oxidative decarboxylation of isocitrate to generate αKG, whereas IDH1/2 mutant catalyzes the conversion of αKG into 2HG. Adapted from* [11]

Tumors with IDH1-mutant can have over 100-fold more 2HG than IDH1-wildtype tumors [12]. 2HG is able to inhibit αKG-dependent dioxygenases, such as histone demethylases, increasing the trimethylation of multiple histone lysine residues [13]. In lower grade gliomas and secondary GB, the cytosine-phosphate-guanine (CpG) island methylation phenotype (G-CIMP) is associated with IDH mutations and a better patient prognosis [14]. This raised the question of whether IDH mutations and 2HG are directly responsible for aberrant DNA methylation. Turcan *et al*. showed that an IDH1 mutation (R132H) established the G-CIMP by remodeling the methylome and transcriptome and interfering with the differentiation state [15]. Lu *et al.* reported that 2HG-producing IDH-mutants prevented histone demethylation and blocked differentiation of non-transformed cells [16]. Moreover, DNA demethylation seems to be linked to glioma progression, as in G-CIMP-positive tumors decrease in methylation levels are related with recurrence and increased tumor grade [17].

1.2.2. Transcriptional subtypes of glioblastoma

Efforts have been put into defining GB subtypes based on their genetic profile in a way that better predicts survival and therapy response [18–20]. Phillips *et al.* identified three high-grade glioma (GB and anaplastic astrocytoma) subtypes based on the expression of survival-related genes: proneural, proliferative and mesenchymal. The proneural subtype correlated with a longer mean survival in comparison with the other subtypes and activated genes associated with neurogenesis. The proliferative and mesenchymal subtypes showed high expression of genes related to cell proliferation and angiogenesis, respectively. Additionally, the authors observed a proneural or proliferative shift to the mesenchymal subtype upon recurrence while analyzing matched pairs of primary and recurrent tumors [21]. However, more recently, this was not observed when different regions of the same tumor were analyzed [22].

The proneural and the mesenchymal have been the subtypes with more unanimity in the literature. In 2010, Verhaak *et al.* together with the Cancer Genome Atlas Research Network described the proneural, neural, classical and mesenchymal subtypes. The proneural subtype presented features associated with secondary GBs, such as younger age, PDGFRA abnormalities and IDH1 and TP53 mutations. Additionally, a high expression of proneural development genes in this subtype was observed, as previously mentioned [21]. The authors postulate that proneural tumors may arise from clinically silent lower grade lesions and, therefore, appear to be primary or, alongside with their oligodendrocytic signature, these tumors may arise from a progenitor or neural stem cell that can also originate oligodendrogliomas. The classical subtype exhibited the most common genomic alterations observed in GB: chromosome 7

amplifications and chromosome 10 deletions, EGFR amplification, and homozygous deletion covering the Ink4a/ARF locus. The mesenchymal subtype was characterized by NF1 mutation/deletion and low level of NF1 expression, and high expression of mesenchymal (YKL40 and MET) and astrocytic (CD44 and MERTK) markers, as previously observed [21]. Moreover, there was higher evidence of necrosis and associated inflammatory infiltrates in mesenchymal tumors. The neural subtype revealed association with oligodendrocytic and astrocytic differentiation but typically expressed neuron markers such as NEFL, GABRA1, SYT1 and SLC12A5. Additionally, the authors reported that all GB subtypes were found in recurrent tumors included in the analyzed primary-recurrent pairs [23]. In 2017, the neural subtype was suggested to be non-tumor specific and likely to originate from contamination because this subtype was associated with the margins of tumors, where normal neural tissue is more likely to be detected [24]. This would additionally explain why this subtype lacks typical genetic abnormalities [25].

Table 2 *- Main features of the molecular subtypes of primary glioblastoma.*

	Proneural	**Classical**	**Mesenchymal**
Methylation	G-CIMP$^+$ (1)		
Mutations	IDH1 (2), TP53 (2)	EGFRvIII (2)	NF1 (2)
Copy Number Alterations	PDGFRA amp. (2)	EGFR amp. (2)	NF1 del. (2)
Immuno-environment			macrophages/microglia (2,3)
Median Survival (months)	17.0 (3)	14.7 (3)	

(1) [26], (2) [27], (3) [28]

1.2.3. Standard of care for glioblastoma

The current typical treatment for newly diagnosed GB patients was established in 2005 after Stupp's landmark clinical trial (EORTC 26981/22981-NCIC CE3). After debulking surgery (partial or complete resection of the tumor), most patients undergo radiotherapy (60 Gy) plus concomitant temozolomide (TMZ) chemotherapy (75 mg/m^2/day for ≤ 7 weeks) followed by 6 maintenance cycles of adjuvant TMZ (150–200 mg/m^2 on 5-day therapy every 28 days). Radiotherapy plus TMZ resulted in statistically significant improved median survival in comparison with radiotherapy alone (14.6 *vs* 12.1 months) [29].

Almost all GB patients experience disease relapse within 6 to 9 months after first-line treatment [30]. Yet, standards of care are not well defined at recurrence. Depending on the Karnofsky Performance Status (KPS - an index from 0 to 100 that represents the patient's ability to perform normal activity and the need for assistance), neurological function and prior treatment, patients with recurrence or progression can undergo: second surgery, chemotherapy, bevacizumab, re-irradiation or experimental therapy [31]. Only about 20-30% of patients can be considered to repeat surgery, and a subsequent good outcome will depend mostly on age, tumor volume and KPS score [32]. Re-irradiation allows palliation of symptoms in a selected group of patients, and in some cases provides an improvement in progression free survival (PFS) and overall survival (OS). Modern techniques such as stereotactic hypofractionated radiotherapy or single-fraction stereotactic radiosurgery improve the targeted delivery of radiotherapy and, therefore, limit toxicity by protecting surrounding normal tissue [33,34]. The most common practice for recurrent GB is TMZ rechallenge or change in dose regimen, but the use of alkylating drugs belonging to the group of chloroethyl-nitrosoureas (i.e., carmustine, lomustine and nimustine) in single or combination regimens is also an alternative. Nowadays, the implantation of biodegradable carmustine wafers (Gliadel, Arbor Pharmaceuticals, US) into the surgical cavity is only occasional [35]. In 2009, anti-angiogenic therapy with bevacizumab (Avastin, Genentech, US), a humanized monoclonal antibody that neutralizes the effect of the vascular endothelial growth factor A (VEGF-A), was approved by the U.S. Food Drug Administration (FDA) for its use alone and in combination with chemotherapy (irinotecan, a topoisomerase I inhibitor) for recurrent GB [36,37]. The efficacy results of a phase 2 clinical trial of combined temozolomide and bevacizumab were inferior to those observed with bevacizumab monotherapy or in combination with irinotecan [38]. In newly diagnosed GB, the addition of bevacizumab to adjuvant TMZ was shown not to improve overall survival and to increase the symptom burden of patients [39].

In 2011 and 2015, the U.S. FDA approved tumor-treating fields (TTFs) for the treatment of recurrent and newly diagnosed GB, respectively. TTFs represent an emerging non-invasive anticancer therapeutic modality that involves the transcutaneous delivery of low-intensity (1–3 V/cm), intermediate-frequency (100–300 kHz), alternating electric fields that exert biophysical force on charged and polarizable molecules known as dipoles [40].

1.2.3.1. Temozolomide chemotherapy

Temozolomide (TMZ), marked as Temodal® in Europe and Temodar® in the US, is a small lipophilic molecule (194 Da) able to cross the blood-brain barrier. At a physiological pH, TMZ is

spontaneously hydrolyzed to the highly unstable compound MTIC [5-(3-methyltria- zen-1-yl) imidazole-4-carboxamide]. MTIC rapidly degrades to AIC [5-aminoimidazole-4-carbox-amide] and methyldiazonium ion, which is responsible for the pharmacological activity of TMZ [41]. The methyldiazonium ion is an alkylating species that preferentially produces methyl adducts at the N^7 and O^6 sites on guanines (70% N^7-methylguanine and 6% O^6-methylguanine) and the O^3 site on adenines (9% N^3-methyladenine) in genomic DNA [41]. TMZ and other methylating and chloroethylating agents can induce 12 DNA base adducts and phosphotriester adducts (reaction with the oxygen atoms of the internucleotidic phosphodiester linkages) [42]. Despite being less frequent, O^6-methylguanine (O^6-MeG) adducts are considered the most cytotoxic, because they are more stable and can persist in the DNA in the absence of O^6-methylguanine-DNA methyltransferase (MGMT). O^6-MeG lesions lead to the insertion of a thymine instead of a cytosine opposite the methylguanine during the first cell cycle after treatment. The DNA mismatch repair system (MMR) excises thymine on the daughter strand, but O^6-MeG persists in the template strand. During the second cell cycle, DNA double-strand breaks are formed, leading to G_2/M cell cycle arrest and, ultimately, apoptosis. Some of the cells, holding unrepaired O^6-MeG lesions but recovering during the second cycle after treatment, undergo apoptosis during following replication cycles [43]. Therefore, temozolomide (or other agents that induce O^6-MeG lesions) only becomes cytotoxic in cycling cells and in those possessing an intact MMR.

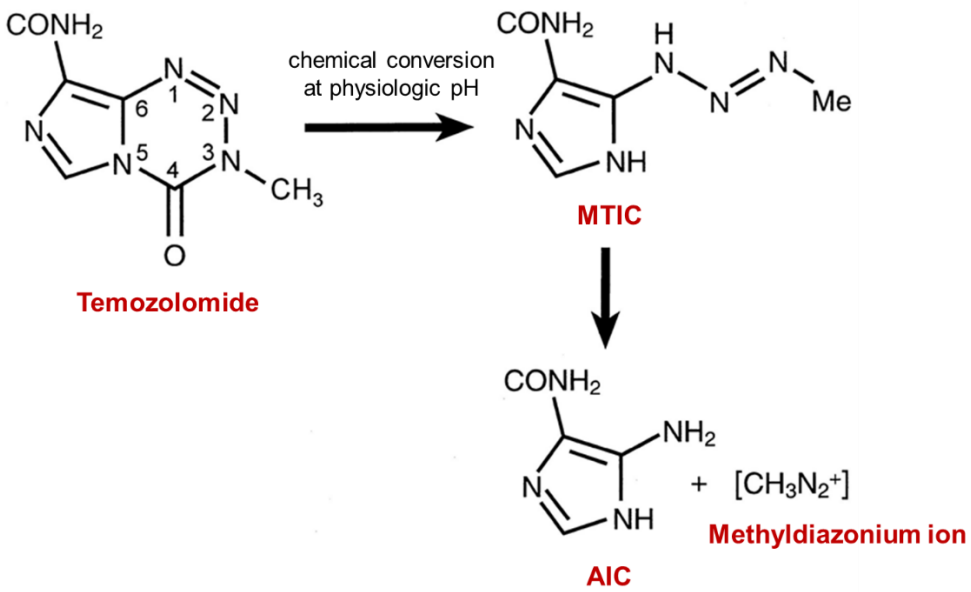

Figure 3 *- Chemical structure and conversion of temozolomide to the alkylating species methyldiazonium ion. Adapted from* [44].

Many tumors express MGMT, a DNA repair enzyme able to remove methyl adducts from the O^6-position of guanine by transferring the methyl group from the oxygen in the DNA to a cystein residue in the catalytic pocket of MGMT - thereby inactivating MGMT. In this way, MGMT antagonizes TMZ activity leading to resistance towards death induction.

MGMT activity is epigenetically regulated. A hypermethylation of its promoter leads to silencing of the gene and thus reduced protein concentrations. Reduced MGMT protein concentrations result in decreased ability of DNA repair, and therefore is associated with improved outcome in patients. Several clinical trials and cohort studies have shown that MGMT promoter methylation is associated with prolonged progression-free and overall survival in patients with glioblastoma who are being treated with alkylating drug chemotherapy. Thus, the methylation status of MGMT became an important prognostic marker for glioblastoma patients.

1.2.4. Hypoxia and glioblastoma stem cells in treatment resistance

Tumor hypoxia results from an inadequate supply of oxygen (O_2) due structurally and functionally disturbed microcirculation within the tumor. Oxygen levels in the brain range from approximately 0.5% to 8% depending on the region[45]. Brain tumors have been shown to contain 1.25% O_2, with the peritumoral area containing approximately 2.5% O_2[46]. Hypoxia is a hallmark of GB and other solid tumors and is associated with tumor cell survival, invasion into the brain parenchyma, therapy resistance and a poorer patient outcome [47].

Hypoxia and TMZ were shown to favor the expansion of the glioblastoma stem cell (GSC) population – these are undifferentiated cancer cells with unlimited self-renewal capability and propensity to promote intratumoral heterogeneity [48,49]. GSCs are considered important drivers of tumor relapse after initial treatment [50]. Thus, prevention of GB recurrence may require the combined therapeutic targeting of differentiated GB cells and GSCs.

1.3. The sphingolipid metabolism in cancer

Studies indicate that alterations in the sphingolipid metabolism play an important role in GB progression and malignant properties [51]. Sphingolipids are a membrane and intracellular family of lipids involved in key cellular processes such as cell growth, adhesion, migration, senescence and cell death. Sphingosine kinases (SK), SK1 and SK2, are enzymes controlling the balance between the sphingolipids sphingosine-1-phosphate (S1P) and ceramide. S1P can be exported

into the extracellular milieu, stimulate five G-protein-coupled receptors (S1PR1-5) and regulate pro-survival intracellular signaling pathways involved in proliferation, invasion, angiogenesis and stem cell properties [52]. In contrast, ceramide is known for its pro-death activities [53]. Ceramide can be generated from sphingosine via ceramide synthases, but also synthetized *de novo* from dihydroceramide via dihydroceramide desaturase 1 (DES1) or generated from the hydrolysis of sphingomyelin via sphingomyelinase. This ability to determine the cell's fate has put sphingolipid metabolism in the spotlight of cancer research, including therapy resistance [54].

SK1 is overexpressed in several cancers such as GB, thyroid cancer, head and neck squamous cell carcinoma, breast cancer, gastric cancer and lung cancer. GB tissue specimens contain higher S1P and lower ceramide levels relative to normal tissue, and high SK1 expression correlated with a shorter survival time of GB patients [55]. Furthermore, several studies revealed that high SK1 expression may confer resistance to chemotherapeutics. On the contrary, SK1 inhibition or knockdown sensitized cells to drug treatment in acute myelogenous leukemia cells, colon cancer cells, and ovarian carcinoma cells. Many chemotherapeutic agents trigger tumor cell death by favoring the production of ceramide [56]. However, SK overexpression can cause the increased ceramide to be metabolized to S1P. Blocking SK might prevent this conversion and support the efficacy of TMZ.

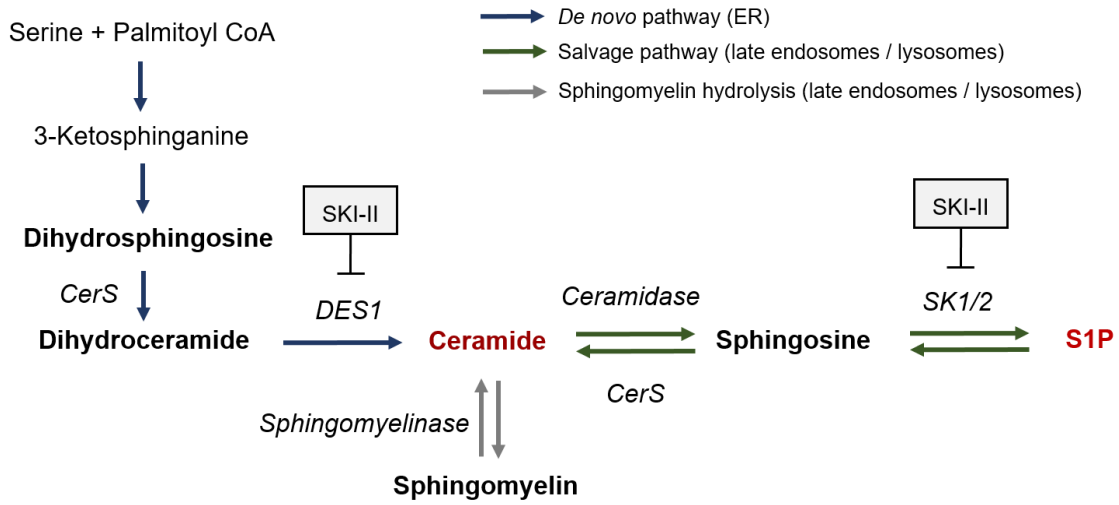

Figure 4 *- The sphingolipid metabolism. There are three major pathways for the generation of ceramide: the de novo, the sphingomyelinase, and the salvage pathway. In the de novo pathway, ceramides are generated from palmitate and serine in the endoplasmic reticulum (ER). In the sphingomyelinase pathway, sphingomyelin is hydrolyzed by sphingomyelinase. In the salvage*

pathway, ceramides are formed from the sphingolipid metabolite sphingosine by ceramide synthase (CerS). Sphingosine-1-phosphate (S1P) is formed when ceramide is broken down by ceramidase and the resulting sphingosine molecule is phosphorylated by the enzyme sphingosine kinase (SK). The sphingosine kinase inhibitor SKI-II inhibits SK1 and SK2, as well as dihydroceramide desaturase 1 (DES1). Adapted from [57].

1.3.1. Pharmacological inhibition of sphingosine kinases

First-generation sphingosine kinase inhibitors, such as D,L-threodihydro- sphingosine (safingol), have been investigated as potential anticancer agents. While these agents did not appear to have significant anti-tumor activity alone, there was evidence that they might potentiate the anticancer effects of known chemotherapy drugs, such as cisplatin[58] and doxorubicin[59]. The dual sphingosine kinase inhibitor SKI-II is orally bioavailable and showed significant *in vivo* antitumor activity without displaying toxicity [60]. Although first described as a sphingosine kinase inhibitor, it was later demonstrated to have off-target effects on DES1[61]. Reported inhibition constants (Ki) indicate a stronger effect of SKI-II on DES1 (Ki = 0.3 μM) rather than on SK1 (Ki = 16 μM) [62] and SK2 (Ki = 7.9 μM). ABC294640, a SK2-selective inhibitor (Ki = 9.8 μM), demonstrated antitumor activity *in vitro* and *in vivo*, and entered clinical testing. The second-generation PF543 is the most potent and selective SK1 inhibitor (Ki = 3.6 μM) described to date. However, it demonstrated a poor pharmacokinetic profile *in vivo*.

Given their key role in controlling cell fate, sphingosine kinases are prime targets to modulate sphingolipid metabolism and have been the focus of many *in vitro* and *in vivo* studies in the past twenty years. [63]

1.4. Autophagy

The term “autophagy” (from Greek, meaning self-eating) was firstly coined in 1963 by Christian De Duve (Nobel Prize winner in 1974) to introduce the concept of lysosomes as a degradative organelle. Currently, the concept of autophagy is firmly established as a highly conserved intracellular degradation process that plays a critical role in cellular homeostasis through the continuous renewal of proteins, carbohydrates, lipids and organelles.

External or internal stress signals such as starvation and hypoxia can induce autophagy beyond basal levels of turnover, so that all nutrients are recycled for biosynthesis or energy production.

Additionally, autophagy can serve as an intracellular quality control system by selectively targeting protein aggregates and damaged or surplus organelles for degradation. In mammalian cells there are three different types of autophagy: macroautophagy, microautophagy and chaperone-mediated autophagy. All these three distinct pathways lead ultimately to the delivery of cargo to the lysosomes for degradation and recycling. Macroautophagy, the most prevalent form of autophagy and, therefore commonly referred as autophagy, requires the formation of double-membrane autophagosomes derived from other cell compartments such as the endoplasmic reticulum (ER), Golgi complex and mitochondria. After a membrane cistern, known as phagophore or isolation membrane, has elongated and engulfed a portion of cytoplasm or a specific cargo, autophagosomes fuse with late endosomes to form amphisomes. Finally, fusion with lysosomes, referred as autolysosomes, delivers the enclosed contents to hydrolytic degradation.

The dynamic process of autophagosome formation, fusion with lysosomes and recycling of lysosomes is called the autophagic flux. Autophagic flux is often inferred on the basis of LC3-II turnover, measured by western blot in the presence and absence of lysosomal or vacuolar degradation (via bafilomycin A1, a specific inhibitor of the vacuolar type H(+)-ATPase (V-ATPase), which inhibits the fusion of autophagosomes with lysosomes). LC3 is a soluble protein that is expressed ubiquitously in mammalian cells. During autophagy, the cytosolic form (LC3-I) is conjugated to phosphatidylethanolamine forming LC3-phosphatidylethanolamine conjugate (LC3-II), which subsequently is recruited into the autophagosomal membrane. LC3-II therefore serves as a marker for autophagosome formation and hence for autophagy. In addition to LC3, p62/SQSTM1 can also be used as protein markers. p62 becomes incorporated into the completed autophagosome and is degraded in autolysosomes, thus serving as an index of autophagic degradation. This means, decreased p62 levels are associated with autophagy activation.

1.5. Cell death mechanisms

Cell death plays a pivotal role in embryonic development, homeostasis and elimination of damaged cells. Understanding cell death in disease is important because it may not only provide insights into the pathogenesis but also leave clues on how the disease could be treated. Cell death was initially divided into type I cell death (apoptosis), type II cell death (autophagy) and type III cell death (necrosis). As the field continues to progress, several novel cell death modalities have been identified and characterized concerning their corresponding stimuli, molecular mechanisms and morphologies. In 2018, the Nomenclature Committee on Cell Death listed

multiple cell death types focusing on molecular and essential aspects of the cell death process. Later in 2020, Yan et al., provided a simpler classification system categorized according to signal-dependency, morphological characteristics and molecular mechanisms (Figure 5) [64].

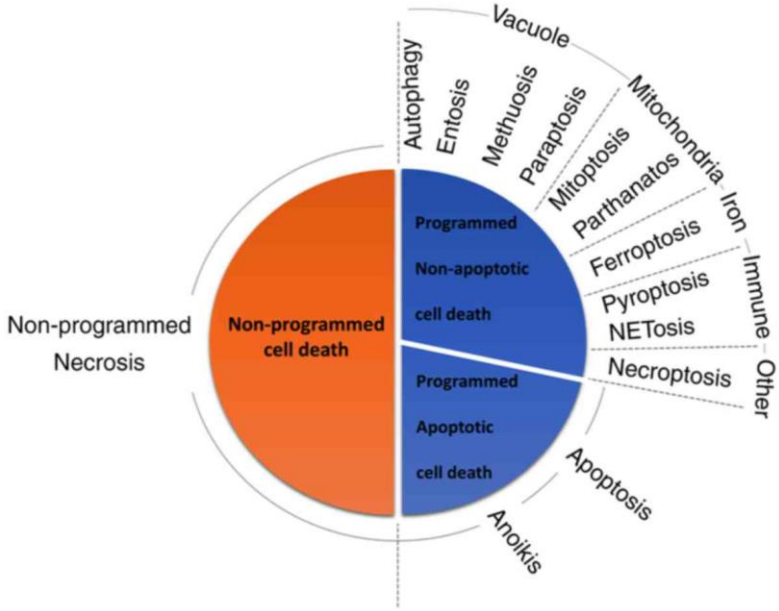

Figure 5 *– Classification of cell death mechanisms by [64]. The pie area in the figure does not represent the frequency of occurrence of each cell death modality.*

1.5.1. Apoptosis

The term "apoptosis" (from Greek, meaning "dropping off, refers to the falling of leaves from trees in autumn) is used to describe the situation in which a cell actively pursues a course toward death upon receiving certain stimuli. Apoptosis is characterized by cell shrinkage, membrane blebbing, and condensation of the chromatin (pyknosis)[65]. It can be further defined as cell death accompanied by the activation of caspase proteases [66]. Two major signaling pathways trigger apoptotic cell death: the mitochondrial (the intrinsic) pathway and the death receptor (the extrinsic) pathway. Both pathways culminate in the activation of caspase proteases and the cleavage of intracellular proteins, ultimately leading to the dismantling of the cell. The intrinsic pathway of apoptosis is triggered upon loss of integrity of the mitochondrial outer membrane, which allows the release of proapoptotic factors, such as cytochrome c, from the mitochondria into the cytosol. This process is controlled by the Bcl2 protein family. Once in the cytosol, cytochrome *c* induces the assembly of a caspase-activation complex: the apoptosome. Caspase-9 is then recruited and

activated by the apoptosome. Active caspase-9 cleaves and activates the executioner caspases-3 and -7. The extrinsic pathway can be activated by another cell that carries a ligand for special death receptors (TRAIL-R, TNF-R, Fas) present at the surface of the target cell. Ligand binding to the receptor causes its aggregation and the recruitment of adaptor proteins to its cytosolic tail. These adaptor proteins recruit procaspase-8 molecules which can activate each other due to their proximity. Active caspase-8 then cleaves procaspase-3 resulting in the destruction of essential cellular proteins and subsequently cell death.

1.5.2. Autophagy in cell death

The term “autophagic cell death,” which was coined in the 1970s in a purely morphological context to refer to cell death with autophagic features (especially the presence of numerous secondary lysosomes); this was sometimes taken to suggest a role of autophagy in the cell death mechanism, but death-mediation was not part of the definition. Based on recent nomenclature guidelines, the roles of autophagy in cell death can be defined as: (i) autophagy-associated cell death, where by the induction of autophagy coincides with the induction of apoptosis (or other cell death pathways), where autophagy simply accompanies the cell death process and does not have an active role in it; (ii) autophagy-mediated cell death, where autophagy induction triggers apoptosis; and (iii) autophagy-dependent cell death, a distinct mechanism of cell death that occurs independently of apoptosis or necrosis.

1.5.3. Necrosis and necroptosis

Necrosis is characterized by cell swelling and plasma membrane rupture, and a loss of organellar structure without chromatin condensation. Although necrosis can occur passively as a consequence of irreparable cell damage, it can also occur in a programmed manner, from a directed signaling cascade. The best-characterized form of programmed necrosis is RIP-kinase-dependent necrosis, also referred to as “necroptosis”. This form of cell death is engaged by several signaling pathways that all converge on the activation of receptor-interacting protein kinase 3 (RIP3). RIP3 is activated upon recruitment to macromolecular complexes downstream from various cell-surface receptors: DRs, Toll-like receptors (TLRs), and the T-cell receptor (TCR). Additionally, DNA damage can directly induce the formation of a RIP3-activation platform, independently of cell-surface receptor ligation. Finally, RIP3-dependent necrosis is also triggered

by the cytosolic DNA sensor, DNA-dependent activator of interferon (DAI) regulatory factors, following virus infection and the presence, in the cytosol, of double-stranded viral DNA**.**

2. OBJECTIVE

Sphingosine kinase inhibitors have been previously tested in combination with chemotherapeutic agents with the goal of increasing ceramides and potentiate cell death of tumor cells. Previous work in the laboratory of Dr. Anne Régnier-Vigouroux showed that 10 µM SKI-II combined with 500 µM TMZ under normoxia induced caspase-dependent cell death in human glioblastoma cells, preceded by accumulation of dihydrosphingosine and dihydroceramide, oxidative stress, endoplasmic reticulum (ER) stress, and autophagy. However, these results raised further questions: First, the TMZ concentration used does not represent what is administered in the clinic nor the concentrations detected in the serum and tumor of patients. Can these effects be seen at lower doses of TMZ and SKI-II? Does it change the way cells die? Secondly, considering that hypoxia is a hallmark of glioblastoma, responsible for TMZ resistance and increased aggressiveness, is SKI-II able to provide therapeutic benefit under this condition? Finally, targeting glioblastoma stem cells might delay or prevent tumor relapse, what is the effect of SKI-II and/or the combination in these cells?

Considering this, the goal of this study was to investigate the therapeutic potential of the sphingosine kinase inhibitor SKI-II in combination with TMZ at clinically relevant doses (≤100 µM) under conditions that better mimic the tumor microenvironment by exposing glioblastoma cells to hypoxia and analyzing its effect in the spheroid model (3D cultures that create oxygen and nutrient gradients). To investigate the therapeutic potential of the combination, I analyzed its effect in cell death, growth and invasion of glioblastoma cells, and the self-renewal capacity of glioblastoma stem cells.

3. MATERIALS

3.1. Reagents

Description	Manufacturer
ABC294640	Selleckchem, Catalog No. S7174
Accutase	Gibco
Acetic Acid	Carl Roth
AnnexinV-FITC, 10X Annexin Binding Buffer	Dianova
B27 Supplement 50X	Thermo Fisher Scientific
Camptothecin	Sigma Aldrich, Catalog No. C9911
Collagenase I, 125 U/ mL	Sigma Aldrich, Catalog No. C9891
Collagenase II, 125 U/ mL	Biochrom C2-28
Dispase, 1 U/ mL	Roche, Catalog No. 04942078001
DMEM high glucose	Gibco
DMEM/F12	Gibco
DMSO ≥99.9%	Sigma Aldrich
DNA Ladder, 100 bp	Biolabs
DNA Loading Dye 6X	Fermentas
DNase I, RNase Free, 79254	Qiagen
ECL Reagent, Western Lightning	Perkin Elmers
FCCP	Sigma Aldrich, Catalog No. C-2920
FeTPPS	Sigma Aldrich, Catalog No. 341492
GelRed Nucleic Acid Stain 10,000X	Biotium
Gentamicin 50 mg/mL	Life Technologies
Glycine	Carl Roth
Laminin 1mg/mL	Sigma
MEM (-Glutamine), 10X	Life Technologies
Methanol ≥99,9 %	Carl Roth
MitoStatus TMRE	BD Pharmingen, Catalog Nr. 564696
N2 Supplement, 100X	Thermo Fisher Scientific
Neurobasal Medium (-Glutamine, -Phenol)	Gibco
PF-543	Selleckchem, Catalog No. S7177
Ponceau AdvanStain	Biozym
Propidium Iodide	Sigma-Aldrich
Protease Inhibitor Cocktail	Roche

PureCol ® Bovine Collagen solution type I	Advanced Biomatrix
TaqMan® gene expression master mix	Life Technologies
Trypsin-EDTA 0.25%	Invitrogen
Glutamine	Life Technologies
Stain Buffer	BD Biosciences, Catalog No. 554656
Recombinant Human EGF, 500 µg	Peprotech
Recombinant Human FGF, 250 µg	Peprotech
SKI-II	Sigma Aldrich, Catalog No. S5696
Sulforhodamine B	Sigma Aldrich, Catalog No. 230162
Temozolomide	Sigma Aldrich, Catalog No. T2577
Z-VAD-FMK	Sigma Aldrich, Catalog No. 219007

3.2. Antibodies

Description	**Manufacturer**
Cleaved Caspase-3 FITC	BD Pharmingen
Isotype mouse	BD Pharmingen
Cleaved Caspase-3	Cell Signaling
LC3B rabbit	Cell Signaling
p62 rabbit	Cell Signaling
BNIP3 monoclonal mouse	Santa Cruz
GAPDH rabbit	Thermo Fischer Scientific
GAPDH mouse	BioLegend
SOX2 rabbit	Cell Signaling
Secondary anti-rabbit IgG	Cell Signaling
Secondary anti-mouse IgG	Jackson Immunoresearch

3.3. Primer IDs

All primers were from TaqMan (Thermo Fisher Scientific)

Gene	Primer ID
AQP4 (Aquaporin 4)	Hs00242342_m1
CA12 (Carbonic anhydrase 12)	Hs0180909_m1
CA9 (Carbonic anhydrase 9)	HS001154208_m1
CD133 / Prominin-1	Hs01009257_m1
DITT3 (DNA damage-inducible transcript 3)	Hs00358796_g1
CXCR4 (C-X-C Motif Chemokine Receptor 4)	Hs0060798_s1
DEGS1 (delta 4-desaturase)	Hs00186447_m1
GAPDH (glyceraldehyde-3-phosphate dehydrogenase)	Hs02758991_g1
MMP2 (Matrix metalloproteinase-2)	Hs01548727_m1
MMP9 (Matrix metalloproteinase-9)	Hs00957562_m1
NANOG (Nanog Homeobox)	Hs02387400_g1
NES (Nestin)	Hs04187831_g1
NEUROD1 (Neuronal Differentiation 1)	Hs01922995_s1
OCT4/ POU5F1 (POU class 5 homeobox 1)	Hs04260367_gH
OLIG2 (Oligodendrocyte transcription factor 2)	Hs00300164_s1
S1PR1 (Sphingosine-1-phosphate receptor 1)	Hs00173499_m1
SPHK1 (Sphingosine kinase 1)	Hs00184211_m1
SPHK1(Sphingosine kinase 2)	Hs01016543_g1
SNAIL1 (Snail family transcriptional repressor 1)	Hs00195591_m1
SOX2 (SRY-box transcription factor 2)	Hs00602736_s1
TGFβ1 (Transforming growth factor beta 1)	Hs00998133_m1
TWIST1 (Twist family bHLH transcription factor 1)	Hs01675818_s1
HIF1α (Hypoxia-inducible factor 1-alpha)	Hs00153153_m1

3.4. Equipment

Device	Type	Manufacturer
Chemiluminescence Imaging System	Fusion FX7 Spectra	PeqLab
Electrophoresis System	XCell Surelock	Thermo Fisher Scientific
Flow Cytometer	Attune NxT	Thermo Fisher Scientific
Microplate reader	Infinite M200 PRO	TECAN
Microscope	DMIL LED	Leica Microsystems
Microscope Camera	DFC 450-C	Leica Microsystems
Real-Time PCR System	StepOnePlus™	Thermo Fisher Scientific
Spectrophotometer	Nanodrop 2000c	Thermo Fisher Scientific
Thermocycler	peqSTAR	PeqLab
Voltage Power Supply	E0203 PeqPower	PeqLab

4. METHODS

4.1. Cell culture

The low-passage-number human glioblastoma cell line NCH82 was previously described [67]. The human glioblastoma cell line LN18 was acquired at the ATCC (Ref cell line). NCH82 and LN18 cells were cultured in complete DMEM (cDMEM) [Dulbecco's Modified Eagle Medium (Sigma, Schnelldorf, Germany),10% (vol/vol) fetal calf serum (Biochrom, Berlin), 2 mM L-glutamine (Life Technologies), gentamicin (50 µg/ml) (GIBCO, Karlsruhe, Germany)]. NCH82 cells were kept in culture for no longer than six passages after thawing.

The human glioblastoma stem cell (GSC) line No. 1080 derives from tumor tissue of a glioblastoma patient and has been previously described [68]. GSCs were cultured as spheres in complete Neurobasal medium (NeuroBasal medium (GIBCO, Catalog No.) supplemented with the B27 component (Invitrogen Life technologies), fibroblast growth factor (FGF) (Peprotech, Catalog No. 100-18B) and epidermal growth factor (EGF) (Peprotech, Catalog No. AF-100-15) 10 and 20 ng/mL, respectively (Biochrom GmbH, Merck KGaA, Germany). 1080 GSCs were selected with 100 µM TMZ (hereafter referred as TMZ-1080), and the respective DMSO control (hereafter referred as DMSO-1080).

The human glioblastoma cell line U3054MG (mesenchymal subtype) was established by the HGCC (Human Glioblastoma Cell Culture Resource) from a GB that recurred after the patient had undergone surgery and radiotherapy (50.4 Gy in total) [69]. Cells were cultured in laminin coated Primaria dishes (Corning) in Neurobasal and DMEM/F12 media (1:1 mix) containing N2 and B27 supplements (Invitrogen) and human recombinant FGF2 and EGF (10 ng/ml, PEPROTECH). The LN229-MGMTc12 cell line was generated by stable transfection of LN229 cells with a human MGMT cDNA expression vector and described previously [70,71].

All cell lines were cultured at 37°C, 5% CO_2 under normoxic (21% O_2) conditions. All treatments were performed in culture medium containing 5% FCS. Cell cultures were regularly tested for mycoplasma contamination (MycoAlert™, Lonza Bioscience). The NCH82, LN18 and 1080 cell lines were authenticated via Single Nucleotide Polymorphism (SNP)-profiling.

4.2. Isolation of the NCH82 stem-like cell population

A fresh stock of NCH82 cells (10^6 cells) was seeded in complete Neurobasal medium and incubated for 4 weeks at 37°C, 5% CO_2 under normoxic (21% O_2) conditions without media

exchange. The formed neurospheres (approximately 300 µm in diameter) were collected, dissociated and further cultured until they reached a size of 200-300 µm.

4.3. Sulforhodamine B assay

The sulforhodamine B (SRB) colorimetric assay is used for cell density determination, based on the measurement of cellular protein content. It was used to determine the dose-effect curves of each drug alone and assess the effect of drug combinations. NCH82 cells were seeded in 96-well plates (1,000 cells/well), allowed to attach for 24h and then treated with each drug and vehicle control (DMSO) in quadruplicates. The cells were further incubated for 5 days at 21% and 3% O_2 in dedicated incubators. The SRB assay was performed as described [72]. The absorbance (OD) of each well was read at 510 nm on a microplate reader (TECAN Infinite M200 PRO). Background absorbance was subtracted from all samples. Percentage of control cell growth was calculated using the formula: % of control cell growth = [(mean OD_{sample} at d5 – mean OD at d0) / (mean $OD_{control}$ at d5 – mean OD at d0)] x 100.

4.4. Drug combination analysis

The combination index (CI) theorem of Chou and Talalay was used to quantitatively determine synergism between combinations of TMZ and SKI-II [73–75]. A combination is considered to be synergistic when CI is below 1, antagonistic when CI is greater than 1, and to have an additive effect when CI equals 1. The CI was calculated via the third-generation software CompuSyn [76]. First, dose-effect curves of each drug alone were determined by exposing cells to 2-fold serial dilutions of TMZ and SKI-II for 5 days at 21% and 3% O_2. The percentage of cell growth was measured using the SRB assay as previously described. This allowed to determine the parameters D_m and m for each drug, which are required for CI calculation. D_m is the dose required to achieve a 50% effect level (ED50), and m depicts the shape of the dose-effect curve (m =1 hyperbolic; m>1 sigmoidal; m<1 negative sigmoidal). Additionally, the parameter r (linear correlation coefficient of the median effect plot) was obtained and refers to the conformity of the data to the mass-action law (for *in vitro* studies r > 0.95). Next, combinations of TMZ and SKI-II at non-constant ratios were tested for 5 days at 21% and 3% O_2. Two-fold serial dilutions below and above the determined ED50 (21% O_2) were performed for SKI-II, and for TMZ only below the ED50, since values above the ED50 (21% and 3% O_2) are clinically irrelevant.

4.5. Propidium iodide and Annexin V staining of NCH82 cells and GSC cells

Flow cytometry was used to assess drug-induced cell death by performing staining with propidium iodide (PI) and Annexin V-FITC (Dianova). NCH82 cells were seeded in 12-well plates (10,000 cells/well) and treated accordingly in duplicates 24h later. After 3 and 5 days of incubation at 21% and 3% O_2, adherent and floating cells were collected and washed twice with 1X Annexin V binding buffer (Dianova). Then, 5 µL of Annexin V-FITC and 1 µg/mL of PI were added to 100 µL of cell suspension and incubated for 15 min in the dark at room temperature. Finally, cells were analyzed with the Attune NxT Flow Cytometer (Thermo Fisher Scientific) at a sample flow rate of 100 µL/min. Flow cytometry data were analyzed with the software FlowJo. The following gating strategy was applied: doublets discrimination (SSC-A vs SSC-H); selection of the population of interest/debris elimination (SSC-H vs FSC-H) and application of the two-color gating/quadrant (BL2-H vs BL1-H).

Spheres of the DMSO-1080 and TMZ-1080 GSC cells were dissociated using Trypsin-EDTA 0,05% (Thermo Fischer Scientific) diluted at a 1:1 ratio in NeuroBasal medium, seeded in 12-well plates and treated accordingly in duplicates 24h later. After 5 days of incubation at 21% O_2 and 3% O_2, adherent and floating cells were collected and processed for staining and analysis at the flow cytometer as described for the NCH82 cells.

4.6. PrestoBlue assay

Cell viability was determined using the PrestoBlue™ Cell viability reagent (ThermoFisher Scientific, Waltham, MA, USA) as described in the manufacturers' protocol. After 72 h of treatment, the reagent was added directly to the wells in the culture medium. After 30 min of incubation at 37°C (5% CO_2) fluorescence was measured using an Infinite® 200 PRO multiplate reader (Tecan, Männedorf, Switzerland).

4.7. *In vitro* extreme limiting dilution assay

GSCs (DMSO-1080 and TMZ-1080) were seeded in 24-well plates in complete NeuroBasal medium at a density of 10 cells/mL and, subsequently, serial diluted until the theoretical cell density of 0.3125 cells/mL (final volume of 1mL). The number of wells used per cell density for each condition [DMSO, TMZ, SKI-II and (TMZ+SKI-II)] in every independent experiment was the following: 6 wells for 10 cells/mL; 12 wells for 5 cells/mL; 18 wells for 2.5 cells/mL; 18 cells for

1.25 cells/mL; 12 wells for 0.625 cells/mL.; and 6 wells for 0.3125 cells/mL. Cells were treated 24h later and further incubated for 4 weeks at 21% and 3% O_2. After the incubation period, the number of wells containing at least one sphere (positive cultures) was registered for each dose (number of cells/well).

The stem cell frequency was determined using the webtool ELDA provided by the Walter and Eliza Hall Institute Bioinformatics Division (https://bioinf.wehi.edu.au/software/elda/) [77].

4.8. Spheroid invasion assay

U3054 spheroids were generated for 48h in ultra-low attachment 96-well plates (CellCarrier Spheroid ULA 96-well Microplates, PerkinElmer) at a density of 8000 cells/40 µL/well. 400 µm diameter spheroids were embedded in a collagen mixture composed of 10X Minimum Essential Medium, 0.1 M NaOH, 3 mg/mL of PureCol® Bovine Collagen solution type I (Advanced Biomatrix) and respective treatment. After 1h incubation at 37°C, complete DMEM (5% FCS) containing the respective treatment was added on the surface of the polymerized collagen mixture and light microscopy images were collected from each spheroid (day 0). Embedded spheroids were further incubated at 21% O_2 or 3% O_2 and images were collected daily. See reference [78] for a detailed description of the method. The size of the spheroids (considering core, halo and invaded area) relative to day 0 was determined automatically via the software Spheroid Analyzer from CLADIAC [79].

4.9. Digestion of spheroids into a single cell suspension

U3054 spheroids embedded in a collagen matrix were isolated via enzymatic digestion. The spheroids were scooped from the collagen, collected into a 15 mL centrifuge tube and washed twice using one volume of PBS. A collagenase digestion mixture was made using 125 U/mL of collagenase I and II and 1 U/mL dispase. 1 mL of the mixture was added to each tube and incubated for 30 minutes at 37°C and 400 rpm in a thermomixer. The spheroids were washed, 1 U/mL dispase was added, and incubation proceeded for further 30 minutes (37°C and 400 rpm). The dispase reaction was stopped by adding 400 µL of cold PBS to each tube. The single cell suspension was washed 2 times with cold PBS. Cells pellets were stored at -80°C for long-term storage or -20°C for short-term storage.

4.10. Detection of activated caspase-3 in treated NCH82 cells and GSC cells

NCH82 cells were seeded in 12-well plates (20,000 cells/well) and treated accordingly in duplicates 24h later. After drug incubation time at 21% and 3% O_2, adherent and floating cells were collected and washed twice with cold 1X PBS, resuspended in BD Cytofix/Cytoperm solution (Catalog No. 554714) and incubated 20 min on ice. Then, cells were washed twice with 1X BD Perm/Wash buffer (Catalog No. 554714) at room temperature and incubated for 30 min with 30 µL of FITC Rabbit Anti-Active Caspase-3 antibody (BD Biosciences, Catalog No. 559341) in 100 µL of 1X BD Perm/Wash buffer at room temperature. Finally, each sample was washed and resuspended in 1X BD Perm/Wash buffer and analyzed by flow cytometry. Flow cytometry data were analyzed via the software FlowJo. The following gating strategy was applied: doublets discrimination (SSC-A vs SSC-H); selection of the population of interest/debris elimination (SSC-H vs FSC-H) and application of one-color gating (BL1-H vs FSC-H).

Spheres of DMSO-1080 and TMZ-1080 GSC cells were dissociated using Trypsin-EDTA 0,05% diluted at a 1:1 ratio in NeuroBasal medium, plated on ornithin-coated glass coverslips and treated accordingly in triplicates 24h later. After 5 days of incubation at 21% and at 3% O_2, cells were fixed with 4% paraformaldehyde, washed with PBS, incubated in blocking solution (0.1% Triton X-100, 1% bovine serum albumin) and stained overnight at + 4°C with a mix of antibodies specific for cleaved caspase-3 (Cell Signaling) and human Nestin (Abcam). Secondary antibodies were goat α-mouse Alexa Fluor 488 (Invitrogen) and goat α-rabbit Alexa Fluor 555 (Invitrogen). Dapi staining was performed according to standard conditions. Stained cells were analyzed by using the BZ-X fluorescence microscope (Keyence Germany GmbH). For each condition (triplicate), 700 to 1100 cells were counted from a total of 7 to 9 regions. Percentage of cells positive for cleaved caspase-3 was determined by using the Image Tool software.

4.11. Measurement of mitochondrial membrane potential

NCH82 cells were seeded in 12-well plates (20,000 cells/well) and treated accordingly in triplicates 24h later. Cells were treated with (TMZ + SKI-II) for 24h and 48h, or with 50 µM FCCP (carbonyl cyanide 4-(trifluoromethoxy) phenylhydrazone) for 60 min. FCCP was used to dissipate the mitochondrial membrane potential. After incubation time under 21% and 3% O_2, the supernatant was removed and replaced with a solution of TMRE (1.2 µM) in Stain Buffer (BD Biosciences). After 30 min incubation at 37°C, the solution was removed, and the wells were washed twice with Stain Buffer. Cells were detached with Accutase and collected into

polypropylene tubes. Finally, cells were washed twice with Stain Buffer at room temperature and analyzed by flow cytometry. The median fluorescence intensity was calculated with the software FlowJo.

4.12. Western blot analysis

4.12.1. Detection of caspase-3, p62, LC3 and BiP proteins

After treatment, adherent and floating cells were harvested and washed twice with cold PBS. The cell pellets were lysed in RIPA buffer (150 mM NaCl, 0.1% Triton X-100, 0.5% sodium deoxycholate, 0.1% SDS, 20 mM Tris-HCl pH 7.5) with a complete EDTA-free protease inhibitor cocktail (Roche, Basel, Switzerland) for 30 min on ice. Lysates were centrifuged at 13000 RPM for 20 min at 4°C. Protein concentration was measured with Pierce™ BCA protein assay kit (Thermo Scientific, Waltham, MA, USA, 23228). Samples of lysates were prepared in Laemmli buffer containing the DTT reducing agent, boiled for 5 min at 95°C and resolved in a 12% polyacrylamide gel (Invitrogen™ SureCast™ Gel Handcast). The following amount of protein was loaded per lane: 20 µg for Caspase-3, 25 µg for LC3 and p62 and 35 µg for BiP analyses. Transfer was performed onto nitrocellulose membrane via a semi-dry blotting system. Membranes were blocked in 5% nonfat milk powder in TBS-T buffer (Tris-base, NaCl and 0.1% Tween 20) for 1 h at room temperature and labeled with the following antibodies against: Cleaved Caspase-3 (Cell Signaling, 9661; 1:1000; rabbit), LC3B (Cell Signaling, 2775; 1:1000; rabbit), SQSTM1/p62 (Cell Signaling, 5114; 1:1000; rabbit), BiP (Cell Signaling, 3177, 1:1000; rabbit), GAPDH (BioLegend, 649202; 1:1000; mouse), and GAPDH (ThermoScientific, PA1-987, 1:1000; rabbit). After washing in TBS-T, membranes were incubated with HRP-conjugated secondary antibodies (anti-mouse IgG, Cell Signaling, 7076S or anti-rabbit IgG, Cell Signaling, 7074S) for 1 h at room temperature, washed again and incubated with chemiluminescence reagent (Western Lightning Plus-ECL, Enhanced Chemiluminescence Substrate, PerkinElmer) for 1 min. Detection was performed with the chemiluminescent imaging system FusionCapt Advance FX7.

4.12.2. Detection of MGMT protein

Whole cell protein was extracted using the Invitrogen cell-extraction buffer (Invitrogen Corporation, Camarillo, CA) according to the manufacturer's protocol. Cell lysates were mixed with RotiLoad 1 (Carl Roth GmbH + Co. KG, Karlsruhe, Germany), boiled for 5 min at 90°C and stored at -20°C until use. Protein concentrations were determined as previously described [80]. For protein detection, 30 µg protein were loaded on to a 10 % SDS-acrylamide gel. Separated proteins

were transferred onto nitrocellulose membrane using a mini-protean blotting chamber. Membranes were blocked in 5% BSA-TBS-T in PBS for 1h at RT. Primary antibodies were HSP90 (Santa Cruz, 1:1000; mouse) and MGMT (produced by B. Kaina, 1:750; rabbit). Secondary antibodies were IRDye 800CW anti-mouse and anti-rabbit IgG (Li-Corn Inc, USA 1:5000). Proteins were detected using the Odyssee 9120 (Li-Cor Inc., USA).

4.13. Sphingolipid analysis

Sphingolipids were extracted from cell pellets using methyl-tert-butyl ether (MTBE)-based liquid-liquid extraction method (LLE). Cells were pelleted in Precellys tubes (Peqlab) to which steel balls were manually added. 1000 µl of MTBE/methanol (10:3, v/v), which served as an extraction solvent, were added to the tubes and then 250 µl of ice-cold 0.1% formic acid containing 5 µM tetrahydrolipstatin/3′-(aminocarbonyl) [1,1′-biphenyl]3-yl)-cyclohexylcarbamate and 10 µg/ml butyl hydroxytoluene as homogenization solvent. A 10 µl methanolic solution of internal standards: Sphingosine d17:1, Sphingosine-1P d17:1, Ceramide d18:1/17:0, Ceramide-1P d18:1/12:0, and Sphingomyelin d18:1/12:0 was then added to the tubes. The concentration of internal standards in the spike solution was set so as to result in a target concentration in the 100 µl final extracts of: 200 ng/ml for Sphingosine d17:1; 200 ng/ml for Sphingosine-1P d17:1; 500 ng/ml for Ceramide d18:1/17:0; 500 ng/ml for Ceramide-1P d18:1/12:0 and 100 ng/ml for Sphingomyelin d18:1/12:0. Samples were then homogenized for 20 sec at 6000 rpm. Homogenates were transferred into 1.5 ml Eppendorf tubes, vortexed for 30 sec at 4°C and centrifuged for 10 min at 13000 rpm. Upper organic phase was recovered in new 1.5 ml tubes, evaporated to dryness under a gentle stream of nitrogen, reconstituted in 90 µl methanol and stored at -20°C till further analysis. Lower aqueous phase was used for protein content determination using the BCA assay. Lipids were analyzed by liquid chromatography/multiple reaction monitoring (LC/MRM) using QTRAP 5500 (AB Sciex) operating in positive/ negative ion mode switching. The ionization and detection parameters as well as LC solvents used for this analysis are as described in [81]. Calibrants and MRM transitions for sphingomyelins, sphingosine and ceramide 1P species are as described in[82]. For the quantification of Ceramide d18:1/24:1 and Ceramide d18:1/16:0 in cell pellets, Ceramide d18:1/17:0 served as internal standard and Ceramide d18:1/16:0 was used as calibration standard. The MRM transitions for detection/quantification of ceramides were manually inferred by direct infusion analysis. For analysis an aliquot of 27 µl methanolic solution of lipid extract was mixed with 3 µl water and transferred in vials for liquid-chromatography/multiple reaction monitoring (LC/MRM) analysis.

Lipid species were quantified using the Multiquant software version 3.0.3. The determined lipid concentrations were normalized to protein content of the cell pellets.

4.14. Real-time quantitative PCR

Isolation of total RNA was performed using RNeasy Mini Kit (Qiagen) according to manufacturers' instructions. After treatment, cells were collected, washed with 1XPBS, and lysed in Buffer RLT (containing 1% ß-mercaptoethanol). All following steps were conducted as described in the manufacturers' protocol. RNA concentration and quality were determined using a Nanodrop 2200 (ThermoFisher). Only samples showing a 260/280 nm ratio between 1.8 and 2.1 were selected for cDNA transcription, which was performed with the Omniscript RT Kit (Qiagen) and random hexamers (Life Technologies). Quantitative PCR (qPCR) analysis was done using TaqMan® primers and a StepOnePlus System (Applied Biosystems). Briefly, for each well of the 96-well qPCR plate (Sarstedt), 10 µl of TaqMan™ Universal PCR Master Mix (ThermoFisher) were mixed with 10 ng cDNA and 1 µl of the appropriate primer (ThermoFisher). All measurements were performed using three technical replicates. Relative quantification (RQ) of gene expression were determined using the $2^{-\Delta\Delta Ct}$ method. Expression of GAPDH, used as a reference gene, was similar in untreated cells under both 21% and 3% oxygen conditions (Ct values of 20,743 and 20,749 respectively).

4.15. Transmission electron microscopy (TEM)

NCH82 cells were cryo-fixed within a few milliseconds at a pressure of 2000 bar under liquid nitrogen using a high-pressure freezer Compact 1 (Wohlwend GmbH, Switzerland). Freeze-substitution was conducted using a Leica EM AFS 2 device (Leica Microsystems, Germany). Here, the substitution/staining medium (acetone p.a., 0.2% osmium tetroxide, 0.1% uranylacetate and 5% water) was pre-cooled to -90 °C before samples were added. Finally, the samples were embedded in EPON 812 and sectioned at room temperature using a diamond knife. Examination of the thin sections was conducted with a FEI Tecnai F20 transmission electron microscope (FEI, USA) operated at an acceleration voltage of 200 kV. Conventional bright field images were acquired using a Gatan US1000 slow scan CCD camera (Gatan Inc., USA).

4.16. Statistical analysis

Data were expressed as the mean (standard deviation, SD) of at least two independent experiments. Statistical analyses were performed using GraphPad Prism software (version 9.2.0). Mean comparison was performed using unpaired *t* test or ANOVA (one-way or two-way). Tukey and Šídák tests were used for multiple comparison analyses. The used statistical method is referred in the legend of the respective figure. Statistical significance was defined by an alpha of 0.05. * $p \leq 0.05$; ** $p \leq 0.01$; *** $p \leq 0.001$; **** $p \leq 0.0001$.

5. RESULTS

5.1. Cytotoxic effect of TMZ and sphingosine kinase inhibitors in human glioblastoma cells under normoxia and hypoxia

The cytotoxicity of temozolomide (TMZ) and the sphingosine kinase inhibitor SKI-II was assessed in the human glioblastoma (GB) cell lines NCH82 and LN18. Additionally, the effect of the sphingosine kinase inhibitors PF543 (SK1-specific inhibitor) and ABC294640 (SK2-specific inhibitor) was assessed in NCH82 cells. The dose-effect curves of each drug were determined via the sulforhodamine B (SRB) assay by treating cells with several 2-fold serial dilutions of the drugs during 5 days under normoxia (21% O_2) and hypoxia (3% O_2) (Figure 6). Based on the dose-effect curves, the software CompuSyn automatically calculates the median effect dose (ED50) of each drug, the shape of the dose-effect curve (the *m* value) and the conformity of the data to the mass-action law (the *r* value) (Table 3 and 4). These parameters are required for further synergism analysis of drug combinations.

In NCH82 cells, the calculated ED50 for TMZ was 96 µM under normoxia and 428 µM under hypoxia, demonstrating that hypoxia induces resistance to TMZ. Cells treated with the specific SK inhibitors ABC294640 and PF543 were only slightly more resistant under hypoxia. On the contrary, SKI-II was equally efficient in inhibiting cell growth in both oxygen conditions (approximately 1.3 µM). NCH82 cells were more sensitive to SKI-II, since the ED50 for SKI-II was 4 to 6 times lower than the specific SK inhibitors. (Table 3). Flow cytometric analysis using Annexin V-FITC and propidium iodide (PI) staining to quantify cell death support that SKI-II is a more potent cell death inducer in these cells (Figure 7). Treatment with PF543 and ABC294640 at a concentration near their calculated ED50 (8 µM) did not induce statistically significant differences in cell death in comparison to the DMSO condition (vehicle control) (Figure 7). Preliminary experiments with higher concentrations (up to 32 µM) of the specific SK inhibitors, revealed that PF543 is a more potent cell death inducer than ABC294640 in NCH82 cells (Figure 8).

In LN18 cells, the calculated ED50 for TMZ was approximately 18 µM under normoxia and 8 µM under hypoxia, demonstrating that hypoxia did not contribute to TMZ resistance. Although these cells have a higher MGMT activity (249 ± 10.6 fmol/mg) than NCH82 cells (11.5 ± 0.3 fmol/mg), they were more sensitive to TMZ treatment in both oxygen conditions. LN18 cells were also more sensitive to SKI-II than NCH82 cells, and the efficacy of SKI-II was also independent of oxygen levels (approximately 0.4 µM) (Table 4).

SKI-II was selected for further experiments over ABC294640 and PF543 due to the following reasons: (i) higher sensitivity to SKI-II, in terms of cell growth inhibition and cell death, (ii) the efficacy of SKI-II was equal in normoxia and hypoxia, and (iii) the *r* value of the dose-effect curves of SKI-II was higher, reflecting a better conformity of the data to the mass-action law, and therefore, providing more confidence in the obtained results (ideally r >0.97 for *in vitro* studies [74]).

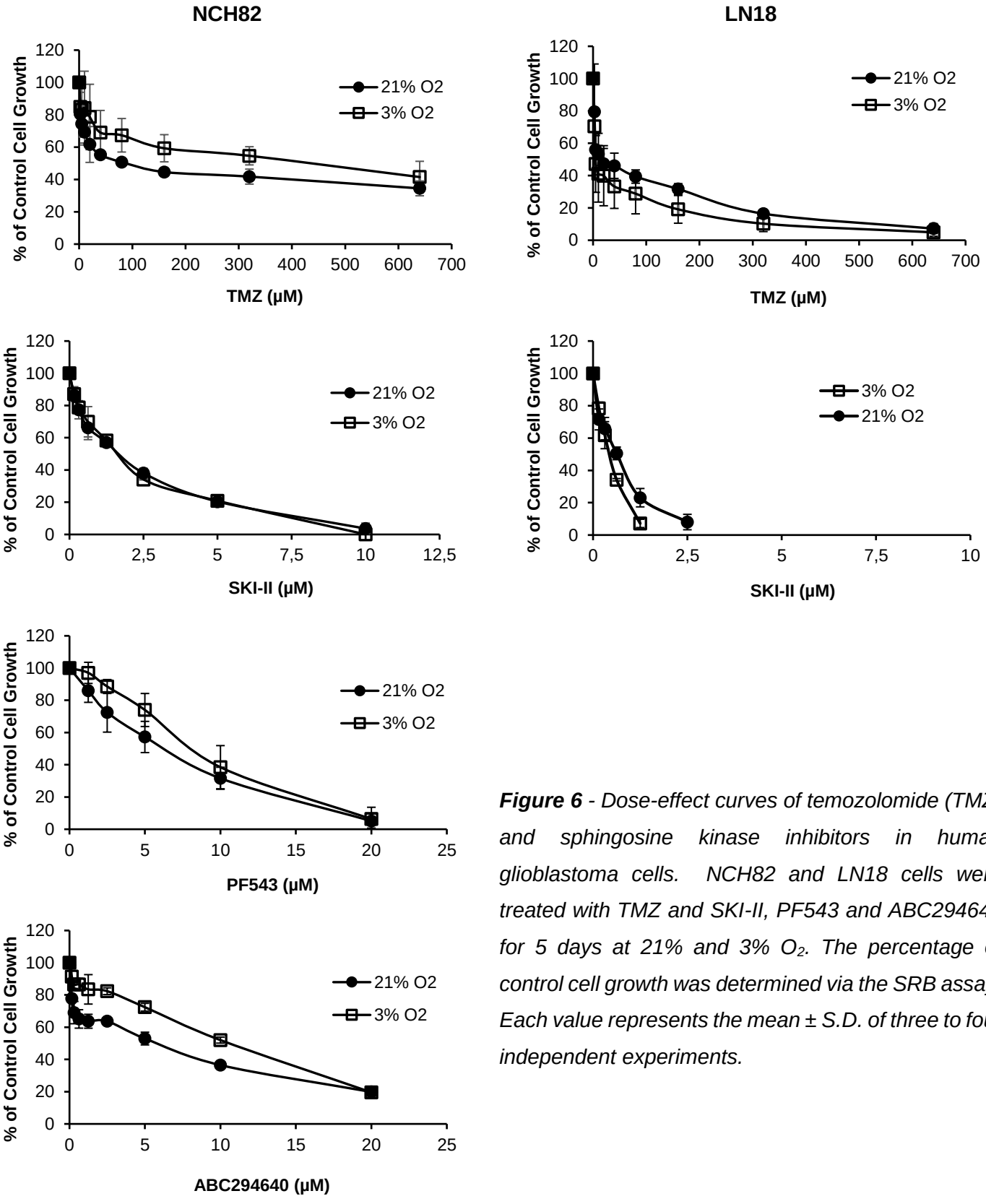

Figure 6 *- Dose-effect curves of temozolomide (TMZ) and sphingosine kinase inhibitors in human glioblastoma cells. NCH82 and LN18 cells were treated with TMZ and SKI-II, PF543 and ABC294640 for 5 days at 21% and 3% O_2. The percentage of control cell growth was determined via the SRB assay. Each value represents the mean ± S.D. of three to four independent experiments.*

Table 3 *- The median-effect dose (ED50) of temozolomide (TMZ) and the sphingosine kinase inhibitors SKI-II, PF543 and ABC294640 was calculated in NCH82 cells at 21% and 3% O_2 using the median-effect analysis program CompuSyn (Nick Martin, MIT, Cambridge, MA, 2005).*

		21% O_2			3% O_2		
Compound	**Concentration range (µM)**	**ED50 (µM)**	***m***	***r***	**ED50 (µM)**	***m***	***r***
TMZ	2.5 - 640	95.67	-0.358	-0.994	427.95	-0.376	-0.976
SKI-II	0.156 - 10	1.33	-0.887	-0.992	1.36	-0.934	-0.992
ABC294640	1.25 - 20	5.57	-0.856	-0.963	7.93	-1.018	-0.950
PF543	1.25 - 20	4.62	-1.617	-0.969	6.86	-2.146	-0.989

*Data obtained from three to four independent experiments.

Table 4 *- The median-effect dose (ED50) of temozolomide (TMZ) and the sphingosine kinase inhibitor SKI-II was calculated in LN18 cells at 21% and 3% O_2 using the median-effect analysis program CompuSyn (Nick Martin, MIT, Cambridge, MA, 2005).*

		21% O_2			3% O_2		
Compound	**Concentration range (µM)**	**ED50 (µM)**	***m***	***r***	**ED50 (µM)**	***m***	***r***
TMZ	2.5 - 640	18.45	-0.561	-0.944	8.37	-0.581	-0.963
SKI-II	0.156 – 2.5	0.45	-1.23	-0.968	0.36	-1.826	0.981

*Data obtained from two to three independent experiments.

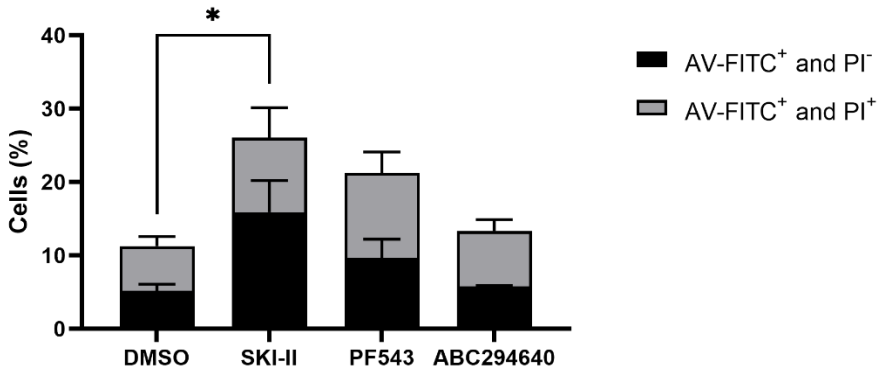

Figure 7 *– Cytotoxic effect of the sphingosine kinase inhibitors SKI-II, PF543 and ABC294640 in human glioblastoma cells (preliminary analysis). NCH82 cells were treated with 2.66 µM SKI-II, 8 µM PF543, 8 µM ABC294640 and DMSO (vehicle control) for 5 days at 21% O_2. Data shows the quantification of flow cytometric analysis of annexin V-FITC (AV-FITC) and propidium iodide (PI)-stained cells. Data represents mean + S.D. of two to three independent experiments (PF543 and ABC294640, n=2; SKI-II, n=3). One-way ANOVA followed by Tukey's multiple comparisons test was performed for statistical analysis.*

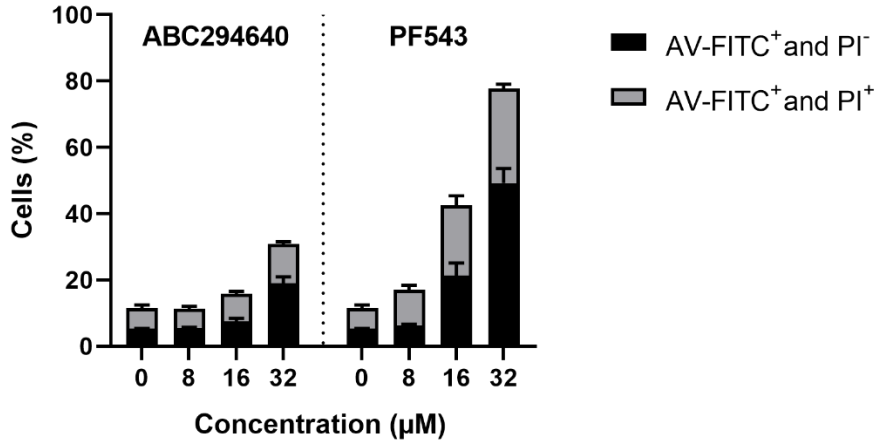

Figure 8 *– Effect of increasing concentrations of the sphingosine kinase inhibitors ABC294640 and PF543 in human glioblastoma cells. Quantification of flow cytometric analysis of annexin V-FITC (AV-FITC) and propidium iodide (PI)-stained cells. NCH82 cells were treated accordingly for 3 days at 21% O_2. Data represents mean + S.D. of two independent experiments.*

5.2. TMZ synergizes with SKI-II to suppress glioblastoma cell growth under normoxia and hypoxia

Drug combinations are extensively considered for cancer therapy. The main aim of combining therapeutics is to achieve a synergistic therapeutic effect which *per se* may allow toxicity reduction, minimize therapeutic resistance, and increase therapeutic efficacy. The term synergism has been mistakenly used as enhancement or potentiation, leading to unsubstantiated synergy claims. In 1984, Paul Talalay (Johns Hopkins University School of Medicine) and Ting-Chao Chou (Memorial Sloan-Kettering Cancer Center) introduced the scientific term “combination index (CI)” to quantitatively define synergism (CI <1), additive effect (CI=1) and antagonism (CI>1). The CI determines the type and degree of interactions between drugs and it can be calculated via the third-generation software “CompuSyn” written by Nick Martin (MIT, Cambridge, MA) in 2005.

The Chou-Talalay CI method was used to find the combination of TMZ and SKI-II with the strongest degree of synergism at the highest effect level towards NCH82 cells. SKI-II and TMZ were combined at a non-constant ratio and the doses of the 15 combinations were based on 2-fold serial dilutions above and below the ED50 of each drug. TMZ concentrations were kept under clinically relevant ranges and, therefore, not tested above 96 µM in combination (Table 5 and 6). All 15 combinations tested under normoxia had a CI value below 1 and are, accordingly, synergistic. Under hypoxia some combinations became nearly additive (combinations A1 and C1-3) or presented a diminished degree of synergism (combinations B1-3), and their effect level was reduced. Interestingly, combinations with higher SKI-II concentration, such as the combinations D1-3 (2 x ED50SKI-II) and E1-3 (4 x ED50SKI-II), presented a constant degree of synergism and similar effect level between oxygen conditions (Figure 9 A, Table 7). The synergistic drug combination consisting of 48 µM TMZ and 2.66 µM SKI-II (D2) was able to inhibit cell growth by almost 80% under normoxia and hypoxia (Table 7). The dose reduction index (DRI), i.e., the measure of how many folds of dose-reduction for each drug at a given effect are allowed in synergistic combination, was obtained from the CompuSyn software (Table 8). The DRI is favorable when above 1. Combinations D and E, which contain higher doses of SKI-II, allowed a higher dose reduction of TMZ. More specifically, the synergistic drug combo (D2) consisting of 48 µM TMZ and 2.66 µM SKI-II was able to inhibit cell growth by almost 80% in normoxia and hypoxia. Additionally, it had a similar degree of synergism in both oxygen conditions (CI = 0.45 in normoxia and CI = 0.51 in hypoxia). The DRI of TMZ for this combination was of 84 under normoxia, and 252 under hypoxia. Meaning that this synergistic (TMZ + SKI-II) combination was able to reduce the concentration of TMZ by 252-fold under hypoxia. The DRI of SKI-II was as well

favorable and similar in both oxygen conditions (1.9 in hypoxia and 2.2 in normoxia). Combinations with a higher degree of synergism at a higher effect level are the most relevant for cancer therapy [83]. For this reason, and to combine a clinically relevant dose of TMZ with the lowest concentration of SKI-II, I decided to use the D2 (48 µM TMZ + 2.66 µM SKI-II) combination for further studies.

The D2 and D3 combos (2.66 µM SKI-II with 48 µM and 96 µM TMZ, respectively) were as well tested in LN18 cells (Figure 9 B). Both combinations inhibited cell growth by about 87% under normoxia and 93% under hypoxia, indicating a higher efficacy under hypoxia. Moreover, there was no advantage in increasing the TMZ dose (D3 combination) since both combinations had the same inhibitory effect in cell growth (Table 9). This suggests that the efficacy of these combinations derives solely from SKI-II. Indeed, the CI revealed that the interaction between TMZ and SKI-II is antagonistic in LN18 cells, in both oxygen conditions (CI > 1). The DRI of SKI-II was below 1, whereas the DRI of TMZ was favorable (above 1), indicating that in these cells SKI-II would have been more effective as a single treatment than in combination with TMZ (Table 10). For this reason, further experiments were performed in NCH82 cells only.

Table 5 *- Median-effect doses (ED50) used for drug combination analysis of temozolomide (TMZ) and the sphingosine kinase inhibitor SKI-II.*

	SKI-II (µM)	**TMZ (µM)**
0.25 × ED50	0.33	24
0.5 × ED50	0.66	48
1 × ED50	1.33	96
2 × ED50	2.66	-
4 × ED50	5.32	-

Table 6 *- Combination design of temozolomide (TMZ) and the sphingosine kinase inhibitor SKI-II. 15 (TMZ + SKI-II) combinations were made based on the ED50 of each drug (SKI-II ED50 = 1.33 µM; TMZ ED50 = 96 µM).*

Drug Combos (SKI-II + TMZ)		**TMZ**		
		0.25 x ED50	0.5 x ED50	1 x ED50
SKI-II	0.25 x ED50	A1	A2	A3
	0.5 x ED50	B1	B2	B3
	1 x ED50	C1	C2	C3
	2 x ED50	D1	D2	D3
	4 x ED50	E1	E2	E3

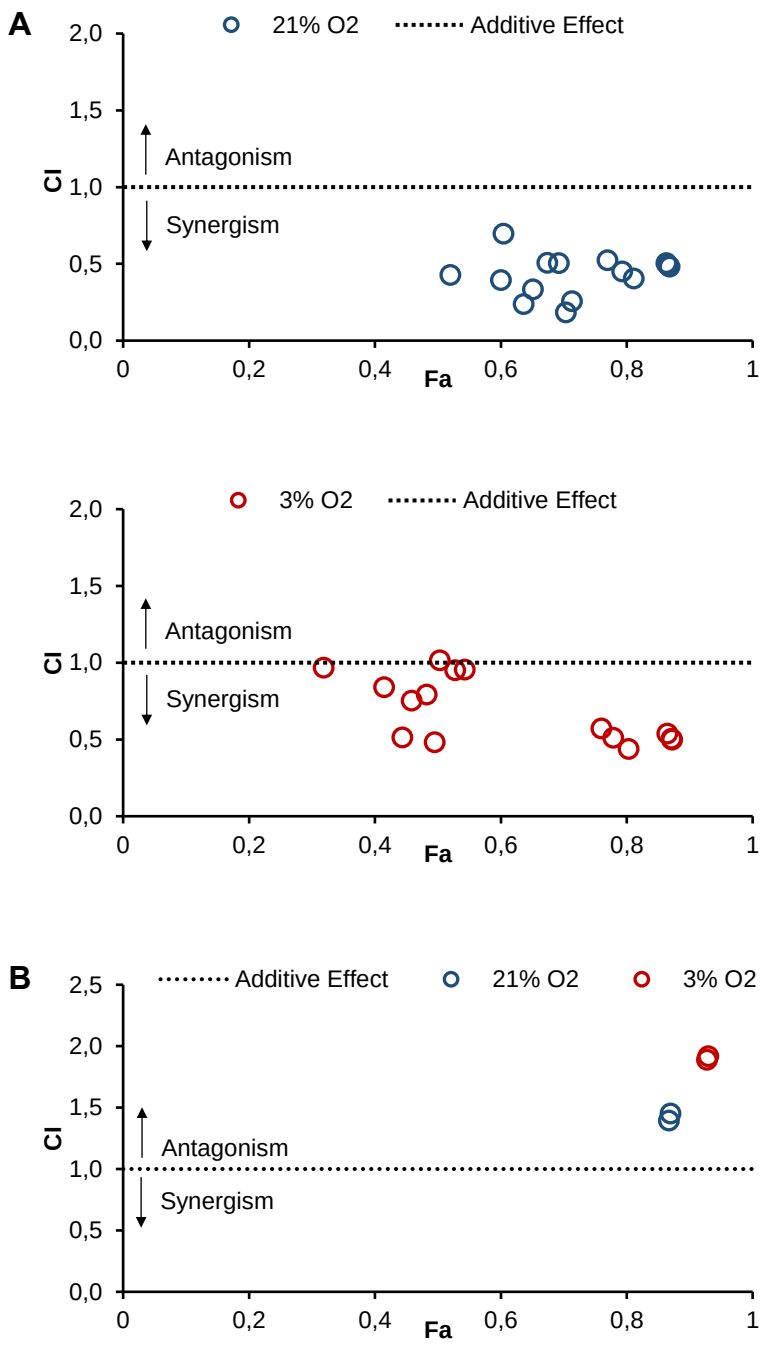

Figure 9 *- Hypoxia affects synergism of (TMZ + SKI-II) combinations. Combination index (CI) vs fraction affected (Fa) plots of (A) 15 drug combinations of TMZ and SKI-II tested in NCH82 cells and (B) 2 drug combinations tested in LN18 cells for 5 days at 21% O_2 and 3% O_2. Data obtained from the median-effect analysis software CompuSyn from the mean of three independent experiments. Fa = 1 - (percentage of control cell growth/100).*

Table 7 *- Combination analysis of temozolomide (TMZ) and the sphingosine kinase inhibitor SKI-II. NCH82 cells were treated with 15 combinations of TMZ and SKI-II for 5 days under normoxia (21% O_2) and hypoxia (3% O_2). Combination Index (CI) was calculated from the CI equation algorithms using CompuSyn software. CI = 1, <1 and >1 indicates additive effect, synergism and antagonism, respectively. Fraction affected (Fa) and CI values of each drug combination were obtained from the average of three independent experiments. Graded symbols were attributed to the CI values to depict the degree of synergism (DS) of each combination, as suggested by Ting-Chau Chou: ++++, strong synergism; +++, synergism; ++, moderate synergism; ±, nearly additive.*

Drug Combo	TMZ	SKI-II	21% O_2			3% O_2		
	Dose (μM)	Dose (μM)	Fa	CI	DS	Fa	CI	DS
A1	24.0	0.33	0.520	0.427	+++	0.318	0.968	±
A2	48.0	0.33	0.636	0.237	++++	0.443	0.513	+++
A3	96.0	0.33	0.703	0.184	++++	0.495	0.483	+++
B1	24.0	0.66	0.600	0.395	+++	0.414	0.841	++
B2	48.0	0.66	0.651	0.333	+++	0.458	0.752	++
B3	96.0	0.66	0.713	0.256	++++	0.482	0.793	++
C1	24.0	1.33	0.604	0.697	++	0.503	1.016	±
C2	48.0	1.33	0.673	0.507	+++	0.527	0.951	±
C3	96.0	1.33	0.692	0.505	+++	0.542	0.955	±
D1	24.0	2.66	0.769	0.523	+++	0.759	0.571	+++
D2	48.0	2.66	0.793	0.451	+++	0.778	0.511	+++
D3	96.0	2.66	0.811	0.404	+++	0.803	0.439	+++
E1	24.0	5.32	0.862	0.504	+++	0.872	0.499	+++
E2	48.0	5.32	0.866	0.490	+++	0.864	0.537	+++
E3	96.0	5.32	0.868	0.482	+++	0.871	0.506	+++

Table 8 *- Dose Reduction Index (DRI) of combinations of temozolomide (TMZ) with the sphingosine kinase inhibitor SKI-II at 21% and 3% O_2 in NCH82 cells. The dose (μM) of TMZ and SKI-II and respective DRI for each combination was calculated using CompuSyn software. DRI=1, >1, and <1 indicates "no dose-reduction", "favorable dose-reduction", and "not favorable dose-reduction", respectively, for each drug in the combination.*

Drug Combo	21% O_2				3% O_2			
	Dose TMZ	Dose SKI-II	DRI TMZ	DRI SKI-II	Dose TMZ	Dose SKI-II	DRI TMZ	DRI SKI-II
A1	119.56	1.45	4.98	4.41	56.87	0.60	2.36	1.83
A2	454.20	2.49	9.46	7.56	234.52	1.06	4.88	3.23
A3	1060.29	3.51	11.04	10.66	406.25	1.33	4.23	4.04
B1	296.49	2.10	12.35	3.18	171.07	0.94	7.12	1.42
B2	544.37	2.68	11.34	4.07	275.44	1.14	5.73	1.72
B3	1213.44	3.71	12.64	5.63	354.22	1.26	3.68	1.91
C1	311.70	2.14	12.98	1.61	443.22	1.38	18.46	1.03
C2	722.46	3.01	15.05	2.26	573.87	1.53	11.95	1.15
C3	915.60	3.31	9.53	2.49	674.22	1.63	7.02	1.23
D1	2745.14	5.16	114.38	1.94	9114.44	4.67	379.76	1.75
D2	4041.18	6.04	84.19	2.27	12113.0	5.24	252.35	1.97
D3	5543.66	6.86	57.74	2.58	17842.0	6.12	185.85	2.30
E1	16124.8	10.57	671.86	1.98	70426.7	10.65	2934.44	2.00
E2	17400.5	10.91	362.51	2.05	58745.6	9.90	1223.87	1.86
E3	18352.1	11.14	191.16	2.09	68447.6	10.53	712.99	1.97

Table 9 *- Combinations of temozolomide (TMZ) and the sphingosine kinase inhibitor SKI-II tested in LN18 cells at 21% and 3% O_2. Combination Index (CI) was calculated from the CI equation algorithms using CompuSyn software. CI=1, <1 and >1 indicates additive effect, synergism and antagonism, respectively. Fractional effect (Fa) and CI values of each drug combination were obtained from the average of two to three independent experiments.*

Drug Combo	TMZ	SKI-II	21% O_2		3% O_2	
	Dose (μM)	Dose (μM)	Fa	CI	Fa	CI
D2	48.0	2.66	0.866	1.393	0.927	1.887
D3	96.0	2.66	0.869	1.451	0.929	1.917

Table 10 *- Dose Reduction Index (DRI) of combinations of temozolomide (TMZ) and the sphingosine kinase inhibitor SKI-II at 21% and 3% O_2 in LN18 cells. DRIs were obtained from CompuSyn software. DRI=1, >1, and <1 indicates "no dose-reduction", "favorable dose-reduction", and "not favorable dose-reduction", respectively, for each drug in the combination.*

Drug Combo	21% O_2				3% O_2			
	Dose TMZ	Dose SKI-II	DRI TMZ	DRI SKI-II	Dose TMZ	Dose SKI-II	DRI TMZ	DRI SKI-II
D2	518.29	2.04	10.79	0.76	672.82	1.46	14.01	0.55
D3	542.23	2.08	5.64	0.78	712.39	1.49	7.42	0.56

5.3. The combination of TMZ and SKI-II potentiates glioblastoma cell death under normoxia and hypoxia

To quantify cell death induced by (TMZ + SKI-II) combination and each drug alone, NCH82 cells were treated for 3 and 5 days under normoxia and hypoxia. After treatment, cells were stained with annexin-V-FITC (AV-FITC) and propidium iodide (PI) and, subsequently, analyzed by flow cytometry (Figure 10 A). At day 3, single treatment with TMZ and SKI-II induced a level of cytotoxicity similar to the combination in both oxygen conditions (Figure 10 B, D). In contrast, at day 5, the combination significantly enhanced cell death in comparison with the single treatments

in both oxygen conditions – an increase between 30-40% in comparison with TMZ alone (Figure 10 C, E). Addition of the pan-caspase inhibitor Z-VAD-FMK (zVAD) did not rescue the cells from death induced by the combination, suggesting induction of a cell death mode independent of caspase activation. Altogether, the present data indicates that treatment with the (TMZ + SKI-II) combination was, both under normoxia and hypoxia, more efficient in killing NCH82 cells than single TMZ or SKI-II treatment, and this effect was time-dependent.

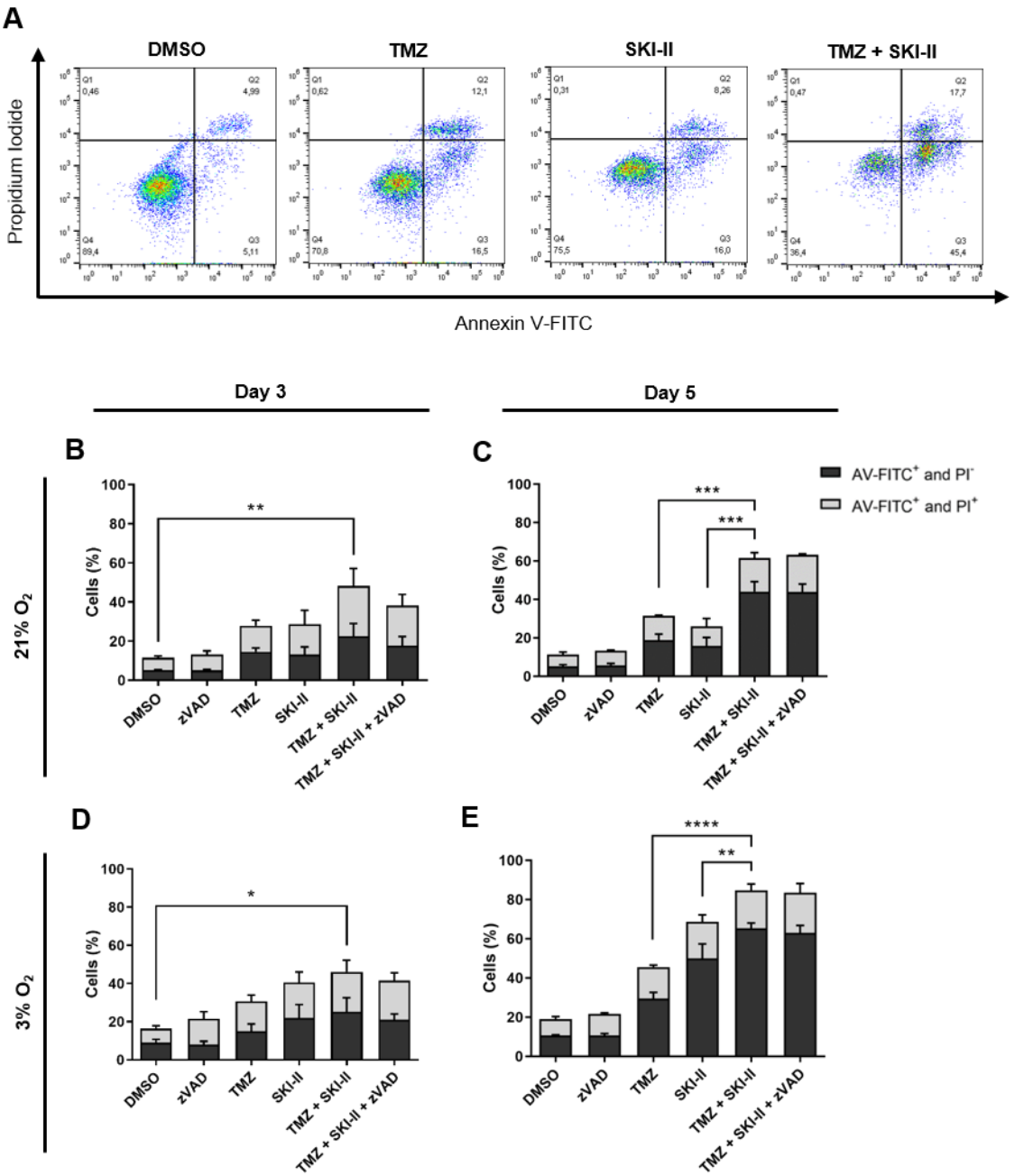

Figure 10 *- The combination of temozolomide (TMZ) and SKI-II potentiates death in human glioblastoma cells. NCH82 cells were analyzed by flow cytometry after treatment with vehicle control (DMSO), 48 µM TMZ, 2.66 µM SKI-II, and the combination (TMZ + SKI-II) in the presence and absence of 20 µM zVAD-fmk (zVAD) for 3 and 5 days, under normoxia (21% O2) and hypoxia (3% O2). (A) Applied quadrant in propidium iodide- (PI) and AnnexinV (AV)-FITC-stained NCH82 cells. (B-E) Quantification of PI- and AV-FITC-labeled NCH82 cells. Data represent mean + SD*

of n = 3. Flow cytometry data analysis was performed using the software FlowJo. One-way ANOVA followed by Tukey's multiple comparisons test was performed for statistical analysis.

5.4. Human astrocytes maintain viability but have impaired proliferation after SKI-II treatment

Previously work published from the laboratory of Dr. Anne Régnier Vigouroux reported that human astrocytes are resistant to 500 µM TMZ and SKI-II up to 30 µM as single treatments or in combination [84]. Since the selected (TMZ + SKI-II) combination is at a much lower dose (48 µM TMZ and 2.66 µM SKI-II), a cytotoxic effect in these cells is not expected. Indeed, flow cytometry analysis of PI-stained human astrocytes treated for 5 days at 21% O_2 showed that the percentage of PI-positive cells in the combination and single treatments was similar to the DMSO (vehicle) control (approximately 5%). Treatment with camptothecin (CPT), a topoisomerase I inhibitor and a known apoptosis inducer, clearly induced cell death in these cells (Figure 11). Thus, at these concentrations, treatment with TMZ and SKI-II seems not to be toxic towards healthy primary cells.

Although light microscopy revealed a normal appearance of the astrocytes after treatment, e.g., with no obvious increase in the amount of floating cells, I noticed a slight decrease in cell density in comparison with conditions without SKI-II. For this reason, I determined the dose-effect curves of each drug in human astrocytes using the SRB assay (which allows to determine cell growth). Based on the dose-effect curves, the median effect dose (ED50) of each drug was calculated using the software CompuSyn (Figure 12, Table 11). The ED50 of SKI-II was approximately 0.7 µM for both oxygen conditions, revealing that SKI-II affects the growth of astrocytes. The ED50 of TMZ was between 177 and 250 µM and therefore, TMZ is not expected to impact the growth of these cells when used at clinically relevant concentrations, e.g., at 48 µM as used in the D2 combination. Preliminary data demonstrated that the growth of human astrocytes is not impacted by treatment for 5 days with the SK1-inhibitor PF543 nor the SK2-inhibitor ABC294640 up to at least a concentration of 20 µM and 10 µM, respectively (data not shown).

Altogether, these data indicate that although SKI-II might not induce cell death in astrocytes, it seems to affect their proliferation, and should therefore be used at the lowest dose possible.

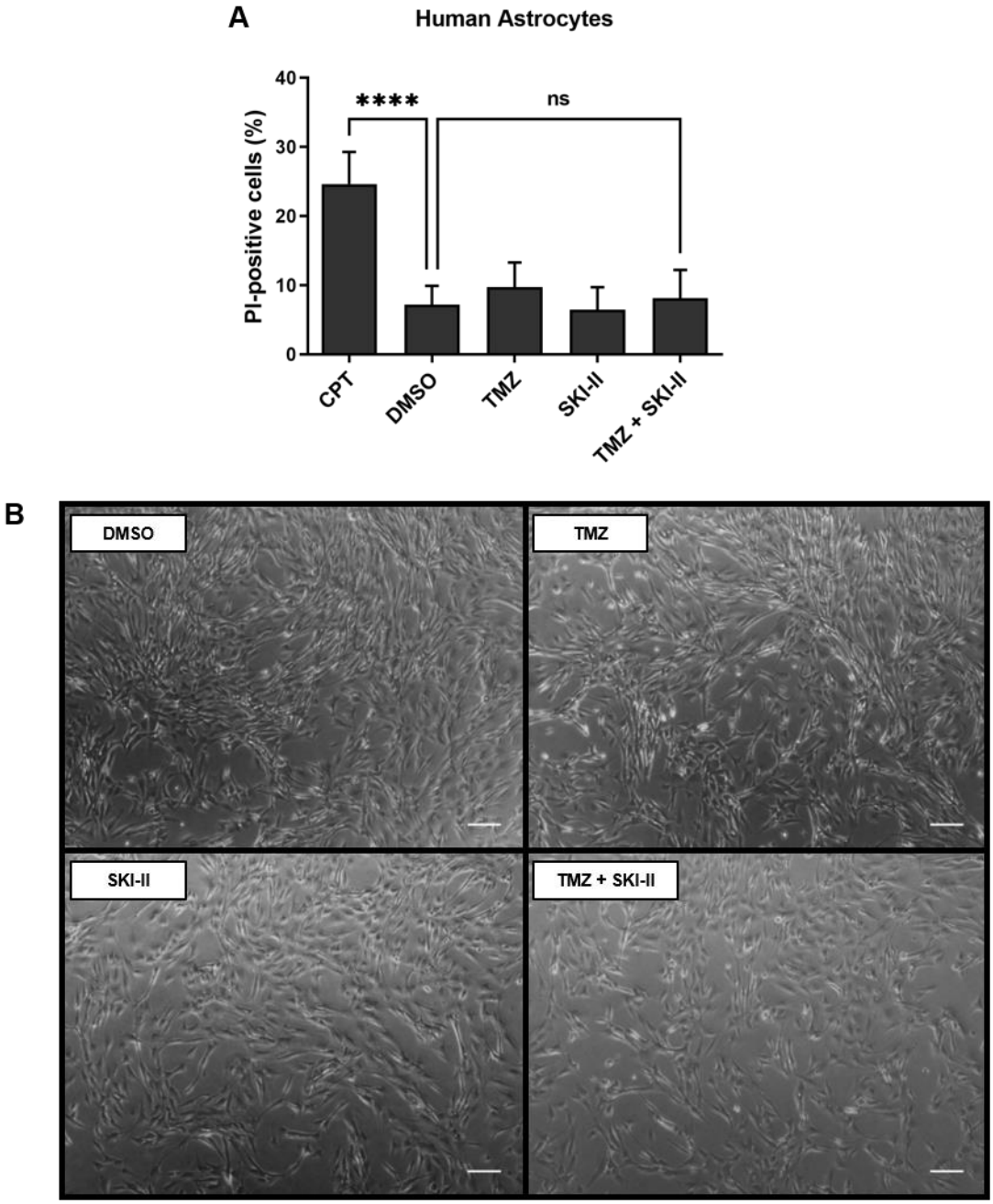

Figure 11 *- The combination of temozolomide (TMZ) and SKI-II does not induce death of human astrocytes (HA). HA were treated for 5 days at 21% O_2 with: 10 µM Camptothecin (CPT), DMSO, 48 µM temozolomide (TMZ), 2.66 µM SKI-II and the combination (TMZ + SKI-II) and stained with propidium iodide (PI). (A) Quantification of flow cytometry data was performed using FlowJo. Data represent mean (+ SD) of n = 4. One-way ANOVA followed by Šídák's multiple comparisons test was performed for statistical analysis. (B) Light microscopy of the treated cells at 5X magnification. Scale bar: 200 µm.*

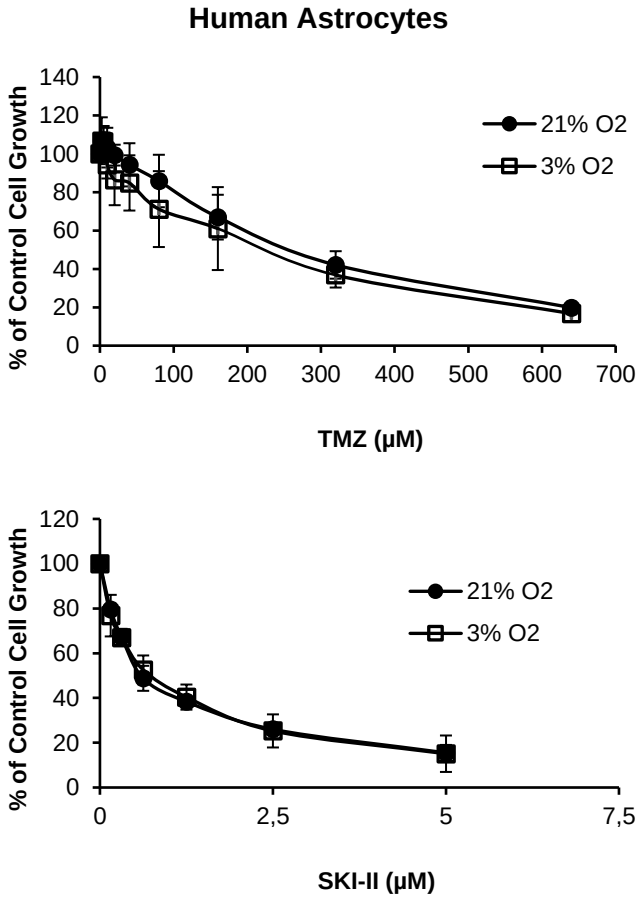

Figure 12 *- Dose-effect curves of temozolomide (TMZ) and the dual sphingosine kinase inhibitor SKI-II in human astrocytes (HA) at 21% and 3% O_2 for 5 days. The percentage of control cell growth was determined via the SRB assay. Each value represents the mean ± SD of n= 3-4.*

Table 11 *- The median-effect dose (ED50) of temozolomide (TMZ) and the sphingosine kinase inhibitor SKI-II was calculated in normal human astrocytes (NHA) at 21% and 3% O_2 using the median-effect analysis program CompuSyn (Nick Martin, MIT, Cambridge, MA, 2005).*

		21% O_2			3% O_2		
Compound	**Concentration range (µM)**	**ED50 (µM)**	***m***	***r***	**ED50 (µM)**	***m***	***r***
TMZ	2.5 - 640	250.2	0.5617	-0.9701	177.13	-1.1024	-0.9852
SKI-II	0.156 – 2.5	0.70	-0.864	-0.997	0.69	-0.8436	-0.9983

*Data obtained from two to three independent experiments.

5.5. The combination induces cell death without caspase-3 activation or mitochondrial membrane potential disruption

Apoptosis can occur via the extrinsic and intrinsic signaling pathways. Both pathways culminate in the activation of effector caspases, such as caspase-3. Addition of the pan-caspase inhibitor Z-VAD-FMK (zVAD) did not rescue NCH82 cells from death induced by the combination (Figure 10 B-E). To confirm this observation, I analyzed the effect of the combination on caspase-3 activation over 72h of treatment under hypoxia and normoxia. As shown in Figure 13, cleaved caspase-3 was not detected in cells treated with the combination after 48h (Figure 13 A, B, Bi) and was expressed in approximately 5% or less of the cells analyzed after 72h of treatment. This indicates that most cells die via a caspase-independent cell death pathway (Figure 13 B, Bi). Note that NCH82 cells are able to activate caspase-3, as shown by the detection of the cleaved caspase-3 after treatment with camptothecin (CPT), a well-known apoptosis inducer (Figure 13 A, B, Bi). Altogether, these data suggest that the combination induces a mode of cell death independent of caspase activation.

During apoptosis, mitochondrial outer membrane permeabilization leads to a loss of mitochondrial membrane potential (MMP) – an event occurring before caspase activation. To analyze whether the (TMZ + SKI-II) combination causes alterations in the MMP, we stained treated NCH82 cells with tetramethylrhodamine ethyl ester (TMRE), a fluorescent dye only able to bind mitochondria with an intact MMP. Fluorescence microscopy showed that treatment with (TMZ + SKI-II) did not cause the loss of TMRE fluorescence which was observed in the FCCP-treated cells (a positive control for the dissipation of the MMP) (Figure 13 C). Quantification via flow cytometry confirmed that FCCP treatment caused a significant decrease of approximately 50% of the median

fluorescence intensity (MFI) of TMRE. The MFI of cells treated with (TMZ + SKI-II) did not significantly differ from the MFI of control cells (DMSO condition) at 24h and 48h, except for an increase observed at 48h under normoxia (Figure 13 D). This increased fluorescence, that could be interpreted as a hyperpolarization, is most likely to result from an increase in cell death at late time points leading to an increase in the dye-to-living cells ratio, as described in [85]. These results indicate that the combination does not cause mitochondrial depolarization under both oxygen conditions, and therefore, mitochondria do not seem to have a decisive role in (TMZ + SKI-II)-induced cell death.

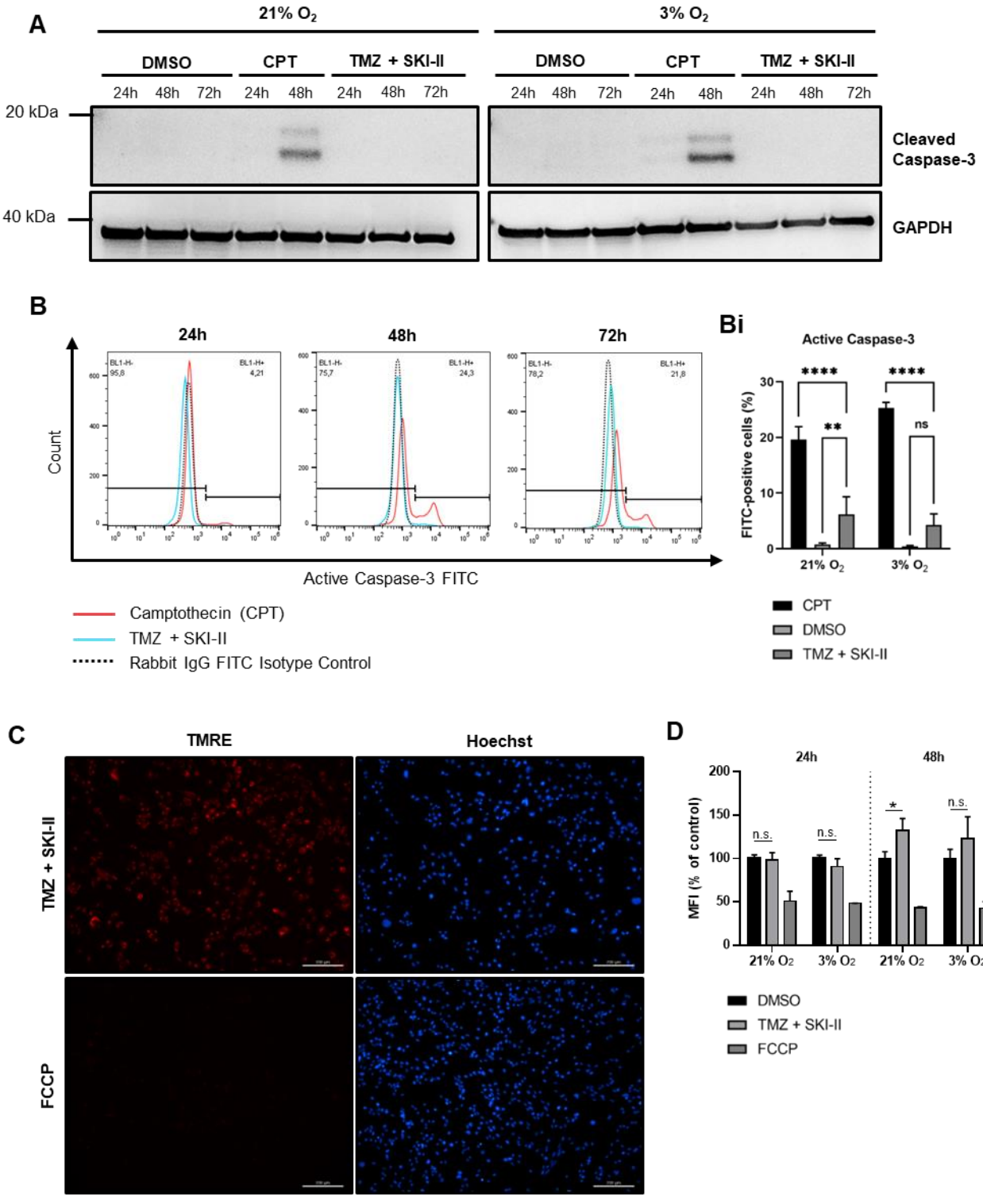

Figure 13 *- Combination-induced cell death occurs without caspase-3 activation and disruption of the mitochondrial membrane potential. (A) Western blot analysis of cleaved caspase-3 in NCH82 cells treated with the vehicle control (DMSO), 15 µM Camptothecin (CPT) and the*

combination of 48 µM TMZ and 2.66 µM SKI-II (TMZ + SKI-II). (B, Bi) Flow cytometric quantification of active caspase-3 FITC-positive NCH82 cells treated with the vehicle control (DMSO), 1 µM Camptothecin (CPT) and (TMZ + SKI-II) for 72 h under normoxia (21% O_2) and hypoxia (3% O_2). (B) Representative plots of NCH82 cells treated under hypoxia. (Bi) Analysis and quantification of the data was performed with the software FlowJo. Data are expressed as the mean (± SD) of the percent of total single cells; n = 3. One-way ANOVA followed by Tukey's multiple comparisons test was performed for statistical analysis. Analysis of the mitochondrial membrane potential by TMRE labelling in NCH82 treated cells via (C) live cell fluorescence microscopy after 48 h at 21% O_2 and (D) flow cytometry after 24- to 48 h under normoxia and hypoxia. Treatment with the depolarization control FCCP (50 µM) for 60 min. The median fluorescence intensity (MFI) of TMRE was calculated with FlowJo. Data represent mean (± SD) of n = 3. Two-way ANOVA followed by Tukey's multiple comparisons test was performed for statistical analysis. Scale bar = 200 µm.

5.6. The combination of TMZ and SKI-II does not affect autophagy in normoxia and hypoxia

The research group of Dr. Anne Régnier-Vigouroux and others have previously reported that TMZ and SKI-II are able to induce autophagy [61,84,86]. Therefore, autophagy could play an important role or, at least, accompany (TMZ + SKI-II)-induced cell death. During autophagy, the cytosolic form of LC3 (LC3-I) is conjugated to phosphatidylethanolamine to form LC3-phosphatidylethanolamine conjugate (LC3-II) which is recruited to autophagosomes. p62 is considered an autophagy substrate and, therefore, is used as a reporter of autophagy activity. To monitor autophagic flux, I analyzed LC3-II and p62 levels in the presence and absence of bafilomycin A1 (BA1). BA1 is a specific inhibitor of the vacuolar type H+-ATPase and inhibits the acidification of organelles containing this enzyme (lysosomes and endosomes). Thus, it blocks the process of autophagy at a late stage. The use of BA1 supports the interpretation of LC3 immunoblotting since an increase in LC3-II levels may represent an increase in autophagy or a block in the autophagy flux [87].

NCH82 cells were treated with the combination and DMSO control for 24h to 72h under hypoxia and normoxia. Under normoxia, p62 and LC3-II protein levels remained similar between both conditions over time (Figure 14 Ai, Aii). The autophagic flux in (TMZ + SKI-II)-treated cells decreased from 24- to 48 h, but there were no differences in comparison with control cells (Figure 14 Aiii). Under hypoxia, p62 protein levels were not significantly affected by the combination whereas LC3-II levels at 72 h were elevated in (TMZ + SKI-II)-treated cells in comparison with the DMSO condition (Figure 14 B, Bi, Bii). Indeed, treatment with the combination tended to decrease

autophagic flux over time, however, this lacks statistical significance (Figure 14 Biii). This trend was not observed in DMSO-treated cells, but as in normoxia, there were no statistically significant differences in the autophagic flux in comparison with the (TMZ + SKI-II)-treated cells. These results suggest that TMZ combined with SKI-II at lower doses does not significantly affect autophagic flux and, therefore, autophagy does not seem to be an essential process in cell death.

The slight increase in the autophagic flux observed in DMSO-treated cells under hypoxia might occur as a mechanism to protect cells against hypoxic stress. BNIP3 (BCL2 and adenovirus E1B 19-kDa-interacting protein 3) is a BH3-only Bcl-2 family member able to induce autophagy and different types of cell death depending on the cellular context. Hypoxia is a well-known inducer of BNIP3. Indeed, BNIP3 is found highly expressed in hypoxic regions of solid tumors, including in GB. Burton *et al*. (2006) reported that in glial cells BNIP3 localizes in the nucleus but can become cytoplasmic and induce cell death under hypoxia. However, in GB, BNIP3 expression is increased, but remains in the nucleus, blocking the ability of BNIP3 to associate with mitochondria and trigger cell death [88]. Considering that BNIP3 is able to induce autophagy under hypoxia [89] and the autophagic flux slightly increased over time under hypoxia in control-treated cells, I analyzed the protein levels of BNIP3 after treatment in normoxia and hypoxia (Figure 15). As expected, under hypoxia, BNIP3 levels were highly upregulated, especially, in DMSO-treated cells. BNIP3 expression remained elevated over time in the DMSO condition, whereas it decreased as cell death occurred by (TMZ + SKI-II) treatment. This indicates that BNIP3 might be induced as a survival mechanism against hypoxic stress. The reduction of BNIP3 over time coincides with a reduction in the autophagic flux after treatment with the combination under hypoxia.

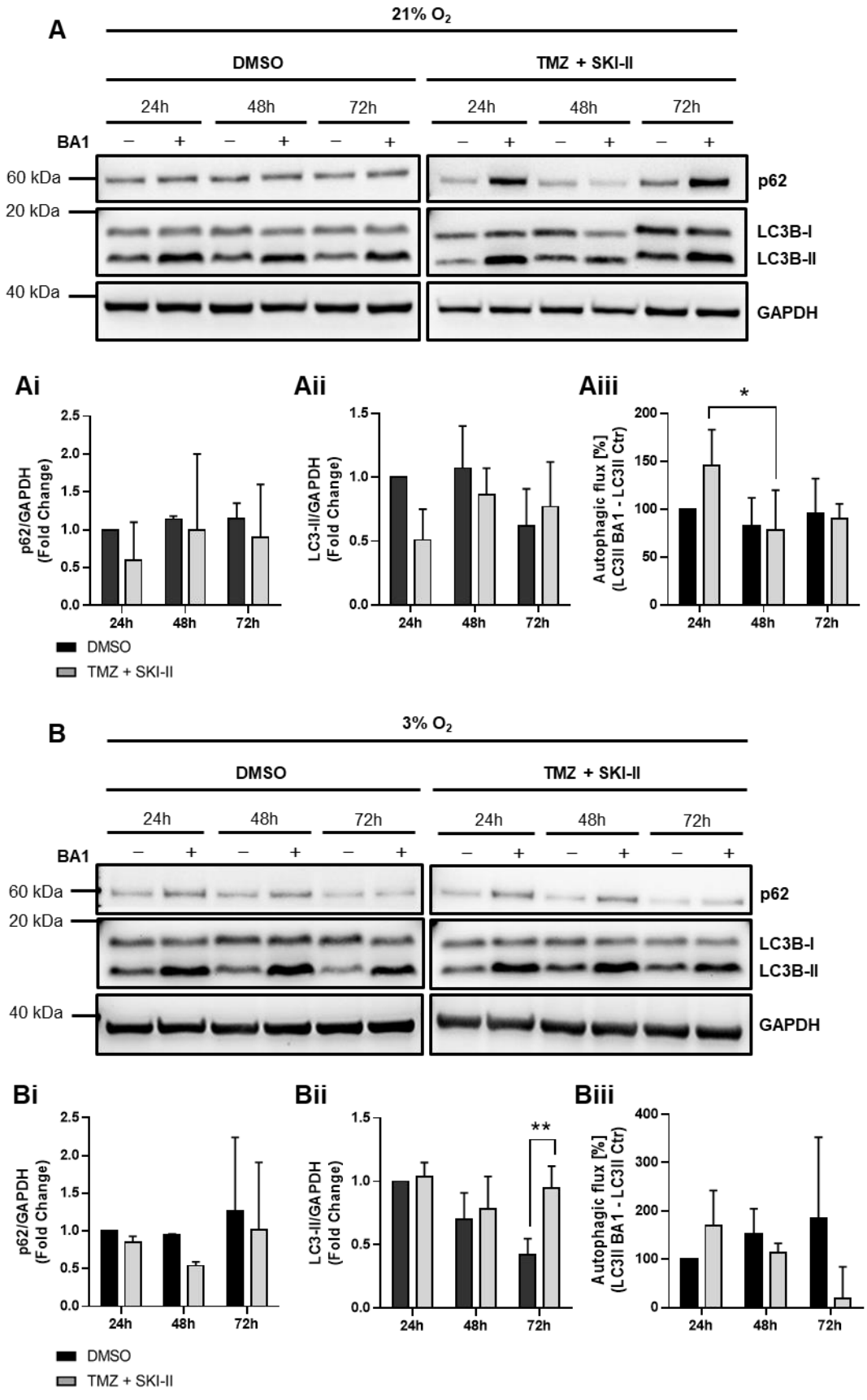
A
21% O2
DMSO
TMZ + SKI-II
24h
48h
72h
BA1
60 kDa
20 kDa
40 kDa
p62
LC3B-I
LC3B-II
GAPDH
Ai
Aii
Aiii
p62/GAPDH (Fold Change)
LC3-II/GAPDH (Fold Change)
Autophagic flux [%] (LC3II BA1 - LC3II Ctr)
*
DMSO
TMZ + SKI-II
B
3% O2
Bi
Bii
Biii
**

Figure 14 *- The combination does not affect autophagic flux in human glioblastoma cells. NCH82 cells were treated with 48 µM temozolomide (TMZ) combined with 2.66 µM SKI-II (TMZ+SKI-II) in the presence and absence of 100 nM Bafilomycin A1 (BA1) under 21% O2 and 3% O2. (A, B) Cell extracts were separated on SDS-PAGE and transferred on nitrocellulose membrane. DMSO and (TMZ+SKI-II) gels were run in parallel. Representative blots are shown. The expression levels of p62 (Ai, Bi) and LC3-II (Aii, Bii) were quantified and normalized to GAPDH. Autophagic flux under basal conditions (DMSO) and under treatment (TMZ + SKI-II) was determined by the subtraction of LC3-II levels without BA1 (Ctrl) from LC3-II levels with BA1 (Aiii, Biii). LC3-II (n = 3); p62 (n = 2). The results are shown as mean (±SD). Two-way ANOVA followed by Tukey's multiple comparisons test was performed for statistical analysis.*

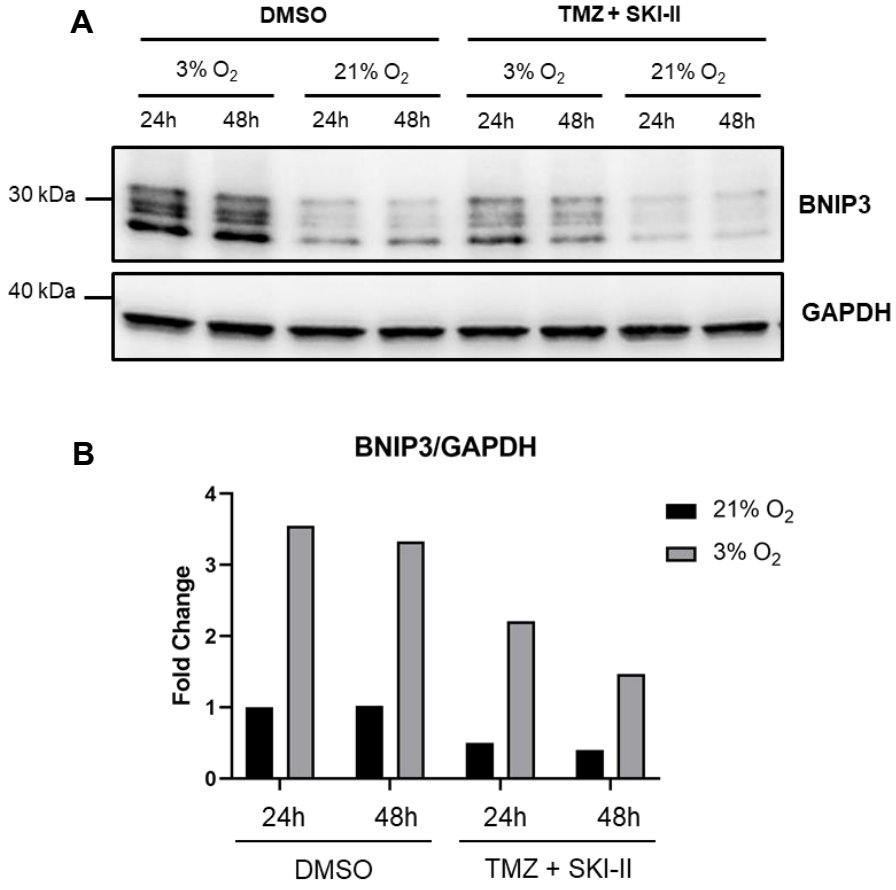

Figure 15 *– BNIP3 is induced under hypoxia. NCH82 cells were treated with 48 µM temozolomide combined with 2.66 µM SKI-II (TMZ+SKI-II) and the respective vehicle control (DMSO) under hypoxia (3% O_2) and normoxia (21% O_2) for up to 48h. Cell extracts were separated on SDS-*

PAGE and transferred on nitrocellulose membrane. The expression levels of BNIP3 were quantified and normalized to GAPDH via ImageJ.

5.7. SKI-II alone and in combination increases cytoplasmic vacuolization

Microscopic observations indicated that SKI-II alone or in combination with TMZ induces cytoplasmic vacuolization in NCH82 cells (Figure 16 A), but not in human astrocytes (Figure 11 B) nor in U3054 cells (mesenchymal subtype GB) (Figure 17). Changes in intracellular complexity, such as cytoplasmic vacuolization, can be detected by the side scatter (SSC) via flow cytometry. NCH82 cells were treated up to 72h with the combination and respective vehicle control (DMSO) and analyzed via flow cytometry. The SSC of (TMZ + SKI-II)-treated cells was significantly increased in comparison to that of control cells (DMSO vehicle) under normoxia and hypoxia. This increase was evident after 24h and aggravated over time. It should be noted that the formation of cytoplasmic vacuoles was observed at the microscope as early as 8h after treatment (data not shown). SSC values observed in combination-treated cells were similar in both oxygen conditions (Figure 16 B, C). The size of the cells, measured via the forward scatter (FSC), was slightly increased after (TMZ + SKII) treatment under normoxia at later time points. These differences were not observed in hypoxia. Altogether these results indicate cytoplasmic vacuolization to be an early effect of sphingosine kinase inhibitor alone and in combination with TMZ.

Based on the previous observations and reported effects of SKI-II on ER dilation and expansion [84], I further examined cytoplasmic vacuolization in treated NCH82 cells by transmission electron microscopy (TEM) in cooperation with Dr. Ingo Lieberwirth (Max Planck Institute for Polymer Research, Mainz). In control cells (DMSO) and in TMZ-treated cells, the ER presented a normal tubular morphology (Figure 18 A, B). In cells treated with SKI-II alone and in combination with TMZ, we observed an enlargement but also fragmentation of the rough ER (vesicles with ribosomes) (Figure 18 C, D). Thus, the cytoplasmic vacuolization observed by light microscopy could represent an expanded and dilated ER. This was deduced by the presence of extensive “white areas” and vesicles with ribosomes (identified by small black puncta inside and at the periphery) in the cytoplasm. Some vesicles did not contain ribosomes and were closely located to (what it seemed to be) a partly fragmented Golgi. These vesicles could be dilated secretory vesicles, because they are positioned at the trans-face of the Golgi. Additionally, cytoplasmic vacuolization can affect non-acidic organelles of the endosomal-lysosomal system and originate from different cellular compartments by different mechanisms [90]. Dilation of the nuclear envelope was also observed in cells treated with SKI-II and the combination. This is not surprising, since

the outer nuclear membrane is directly continuous with the rough ER. These ultrastructural changes were observed under both oxygen conditions (21% O_2 not shown). Untreated NCH82 cells commonly presented disarrangement and distortion of mitochondrial cristae. Such abnormalities have been previously described in GB [91].

Analysis of the SSC in astrocytes showed that, although cytoplasmic vacuolization was not observed by light microscopy, (TMZ + SKI-II) treatment also increases intracellular complexity in astrocytes (Figure 19), but not as severely as in NCH82 cells. This was confirmed by electron microscopy analysis of human astrocytes, showing formation of vacuolization similar to what was observed in NCH82 cells, although not as extensive and, therefore, not visible by light microscopy (Figure 20). Treatment with the combination did not significantly affect the size of the astrocytes, as revealed by the FSC (Figure 19). As previously mentioned, in U3054 cells, cytoplasmic vacuolization was not observed by light microscopy (Figure 17 A). These observations go along with flow cytometric analysis under normoxia, and only a slight (but significant) difference between the control and combination under hypoxia. The size of the cells (FSC) remained unaffected between treatment conditions (Figure 17 B). Cytoplasmic vacuolization was not observed via microscopy in NCH82 cells treated with the SK1-inhibitor PF543 nor the SK2-inhibitor ABC294640. This indicates that this phenotype might be related to off-target inhibition of DES1 via SKI-II (Figure 21).

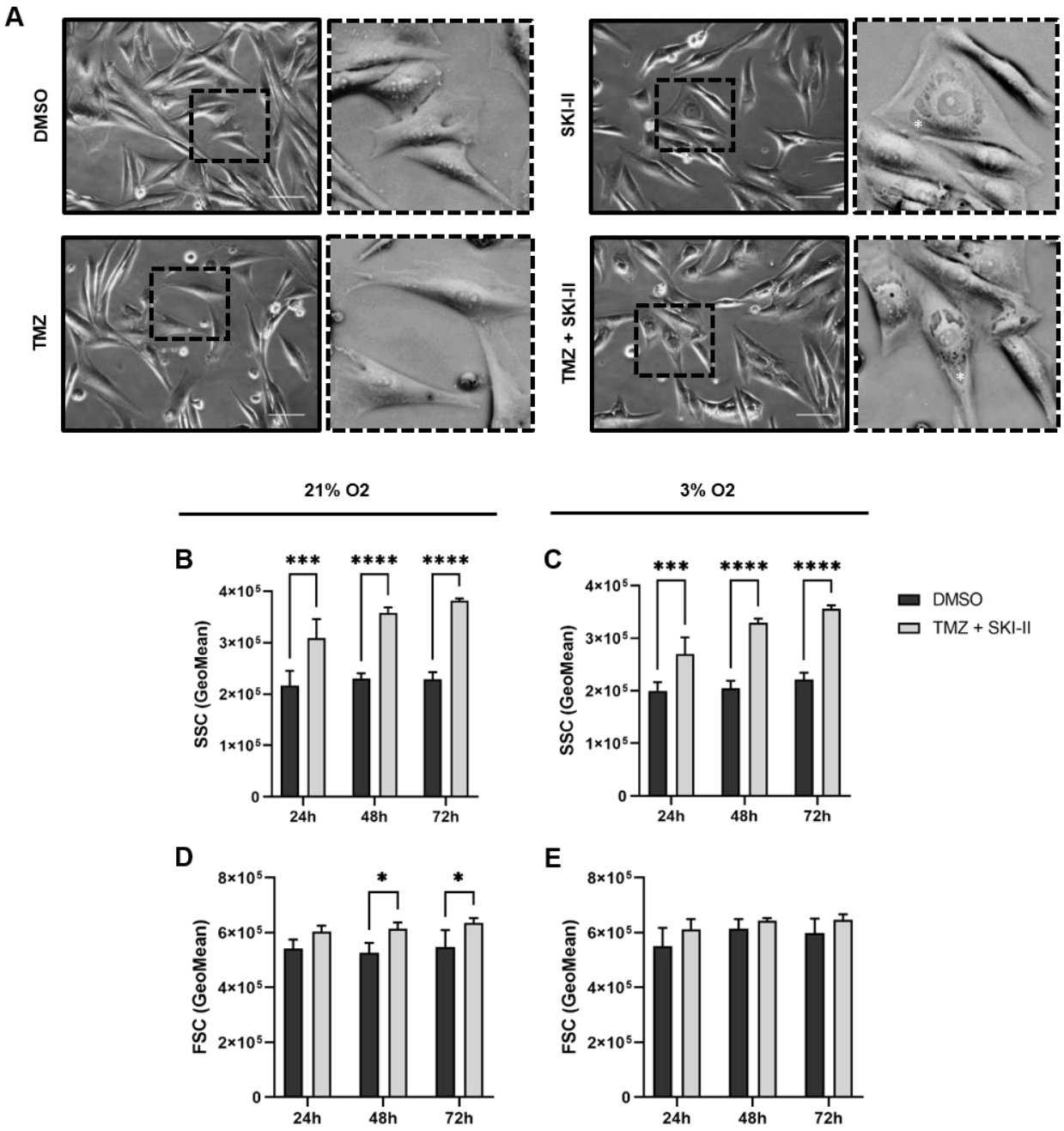

Figure 16 *- SKI-II alone and in combination with temozolomide (TMZ) increases cytoplasmic vacuolization in human glioblastoma cells. (A) Light microscopy of NCH82 cells treated for 72h at 3% O_2 with the vehicle control (DMSO), 48 µM TMZ, 2.66 µM SKI-II, and the combination (TMZ + SKI-II). (B-E) NCH82 cells were treated accordingly for 24- to 72h under normoxia (21% O_2) and hypoxia (3% O_2) and further analyzed by flow cytometry. The light scattering parameters SSC (side scatter) and FSC (forward scatter) were quantified with FlowJo. Data represent mean (+*

SD) of n=3. Scale bar: 100 µm. Two-way ANOVA followed by Šídák's multiple comparisons test was performed for statistical analysis.

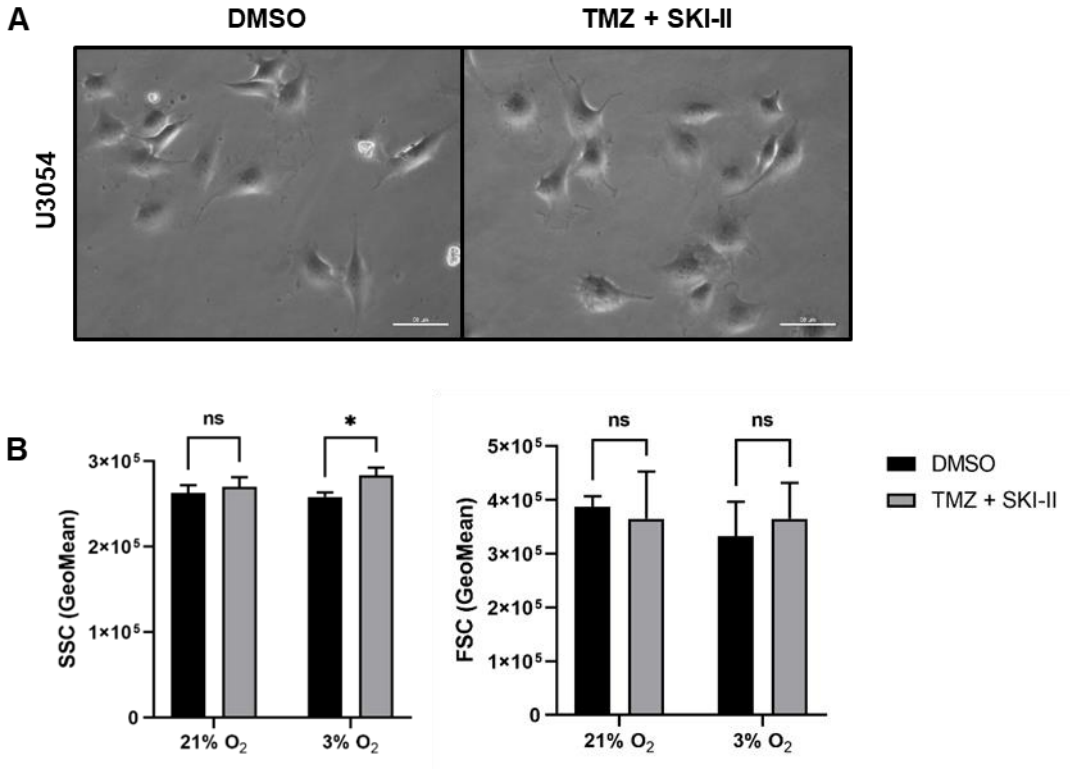

Figure 17 *- Effect of the combination of temozolomide (TMZ) and SKI-II on the internal complexity and size of human glioblastoma U3054 cells. (A) Light microscopy of cells treated with 48 µM temozolomide (TMZ) combined with 2.66 µM SKI-II and the vehicle control (DMSO) for 48h under 21% O_2. (B) Cells were treated accordingly for 72h under normoxia (21% O2) and hypoxia (3% O2) and further analyzed by flow cytometry. The light scattering parameters SSC (side scatter) and FSC (forward scatter) were quantified with FlowJo. Data represent mean (+ SD) of n=3. Scale bar: 50 µm. Two-way ANOVA followed by Šídák's multiple comparisons test was performed for statistical analysis.*

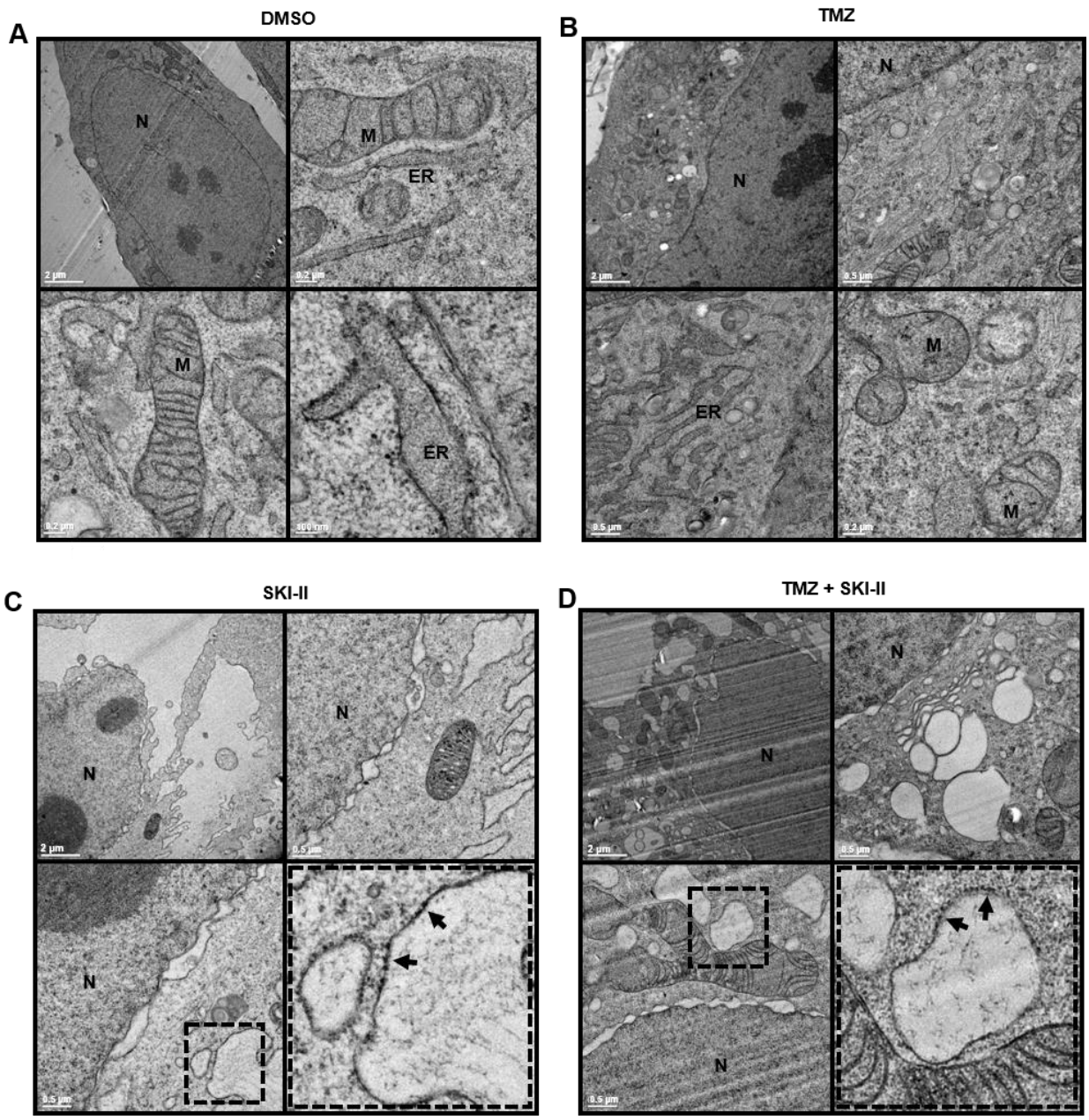

Figure 18 *- SKI-II alone and in combination with temozolomide (TMZ) induces dilation and fragmentation of the ER in human glioblastoma cells. NCH82 cells were treated at 3% O_2 with (A) the vehicle control (DMSO), (B) 48 µM TMZ, (C) 2.66 µM SKI-II, and (D) the combination (TMZ + SKI-II) for 48 h and further analyzed via transmission electron microscopy. Dotted squares are regions of interest. N – nucleus; M – mitochondria; ER – endoplasmic reticulum. Black arrows show ribosomes.*

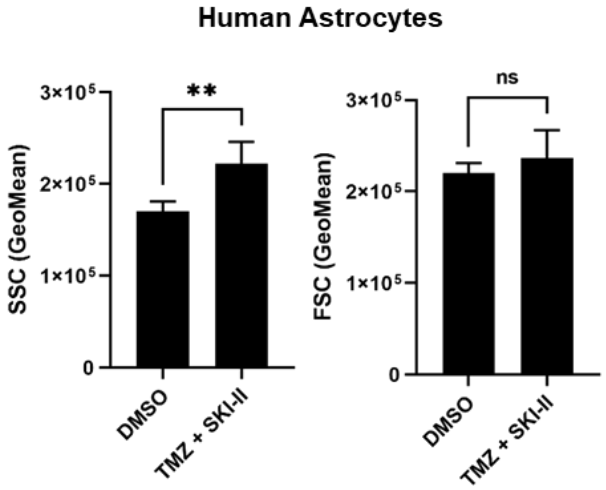

Figure 19 *- Effect of the combination of temozolomide (TMZ) and SKI-II on the internal complexity and size of human astrocytes. Cells were treated with 48 µM TMZ combined with 2.66 µM SKI-II (TMZ + SKI-II) and vehicle control (DMSO) for 72h under normoxia (21% O2) and further analyzed by flow cytometry. The light scattering parameters SSC (side scatter) and FSC (forward scatter) were quantified via the software Flowjo. Data represent mean (+ SD) of n=4. An unpaired t test was performed for statistical analysis. GeoMean, geometric mean.*

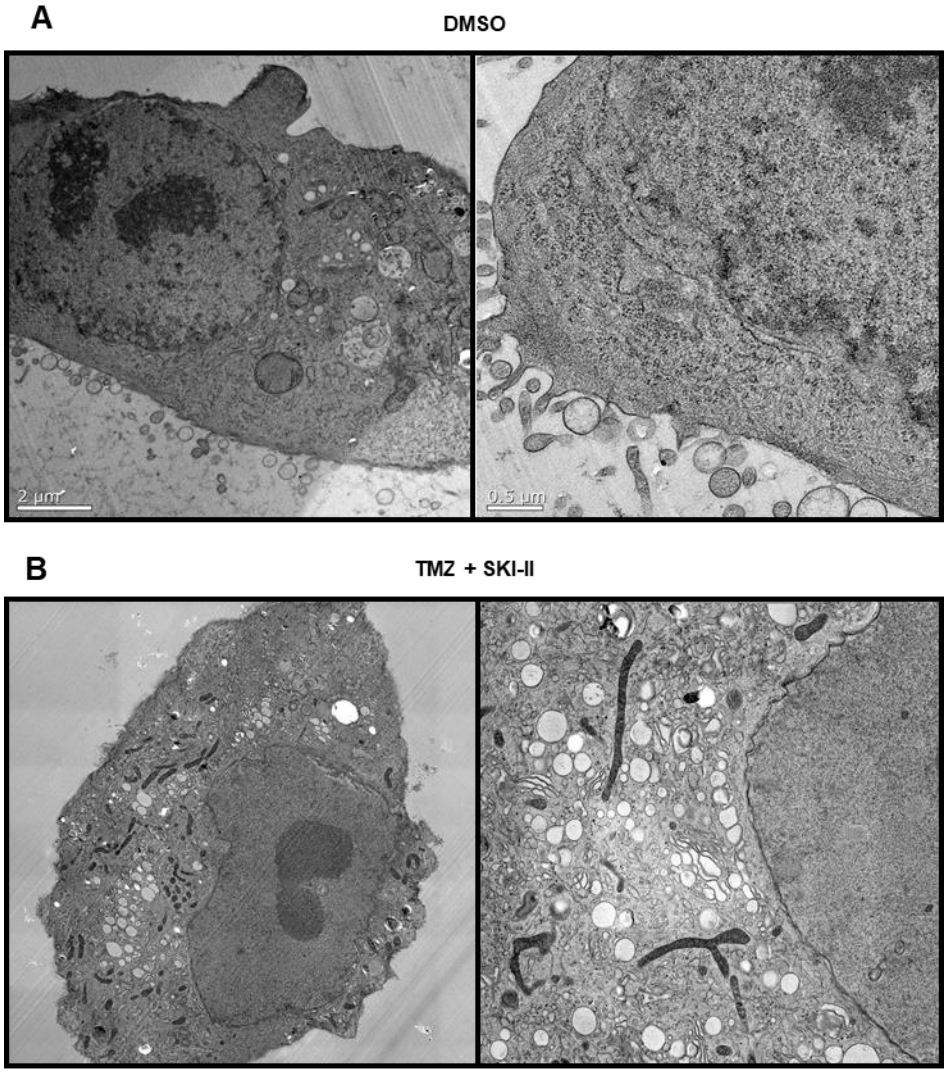

Figure 20 *- The combination of temozolomide (TMZ) and SKI-II induces cytoplasmic vacuolization in human astrocytes. Human astrocytes were treated with 48 µM TMZ combined with 2.66 µM SKI-II (TMZ + SKI-II) and vehicle control (DMSO) for 48h under normoxia (21% O2) and further analyzed via transmission electron microscopy.*

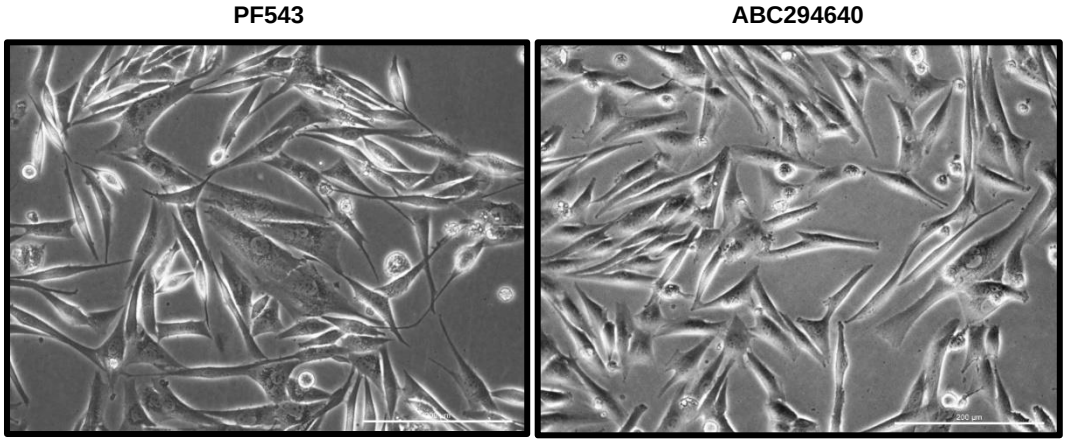

Figure 21 *- The sphingosine kinase inhibitors PF543 (SK1 inhibitor) and ABC294640 (SK2 inhibitor) do not cause cytoplasmic vacuolization at the microscopic level in human glioblastoma cells. Light microscopy of NCH82 cells treated accordingly (at 16 µM) for 72h under 21% O_2. Scale bar: 200 µm.*

5.8. The combination of TMZ and SKI-II induces ER stress and the Unfolded Protein Response

The morphological changes on the ER of NCH82 cells observed via electron microscopy suggest that similar to cells treated with a higher dose combination [84], cells treated with the (TMZ + SKI-II) combination used in the present study underwent ER stress. To confirm this, we analyzed the protein levels of the ER chaperone BiP (Binding immunoglobulin Protein) also known as GRP78 (glucose regulatory protein 78), and the expression of Unfolded Protein Response (UPR) target gene *DDIT3* coding for CHOP (C/EBP Homologous Protein). Under stress conditions, BiP dissociates from ER transmembrane proteins resulting in the activation of the UPR. Subsequently, BiP expression is upregulated to support the re-establishment of ER homeostasis. Prolonged UPR activation leads to the induction of the pro-apoptotic transcription factor CHOP. Treatment of NCH82 cells up to 48 h with the combination resulted in upregulation of BiP expression levels. Co-treatment with Bafilomycin A1 did not affect BiP expression, suggesting that autophagy does not have a role in the mitigation of ER stress (Figure 22 A, Ai). In contrast to TMZ treatment, SKI-II alone or in combination elevated *DDIT3* expression levels by about 6-fold, showing that ER stress levels are increased due to SKI-II treatment solely (Figure 22 B). Hypoxia does not seem to aggravate ER stress, since BiP and *DDIT3* levels were similar in both oxygen conditions. Altogether, these data indicate that SKI-II alone or in combination with TMZ induces ER stress in NCH82 cells.

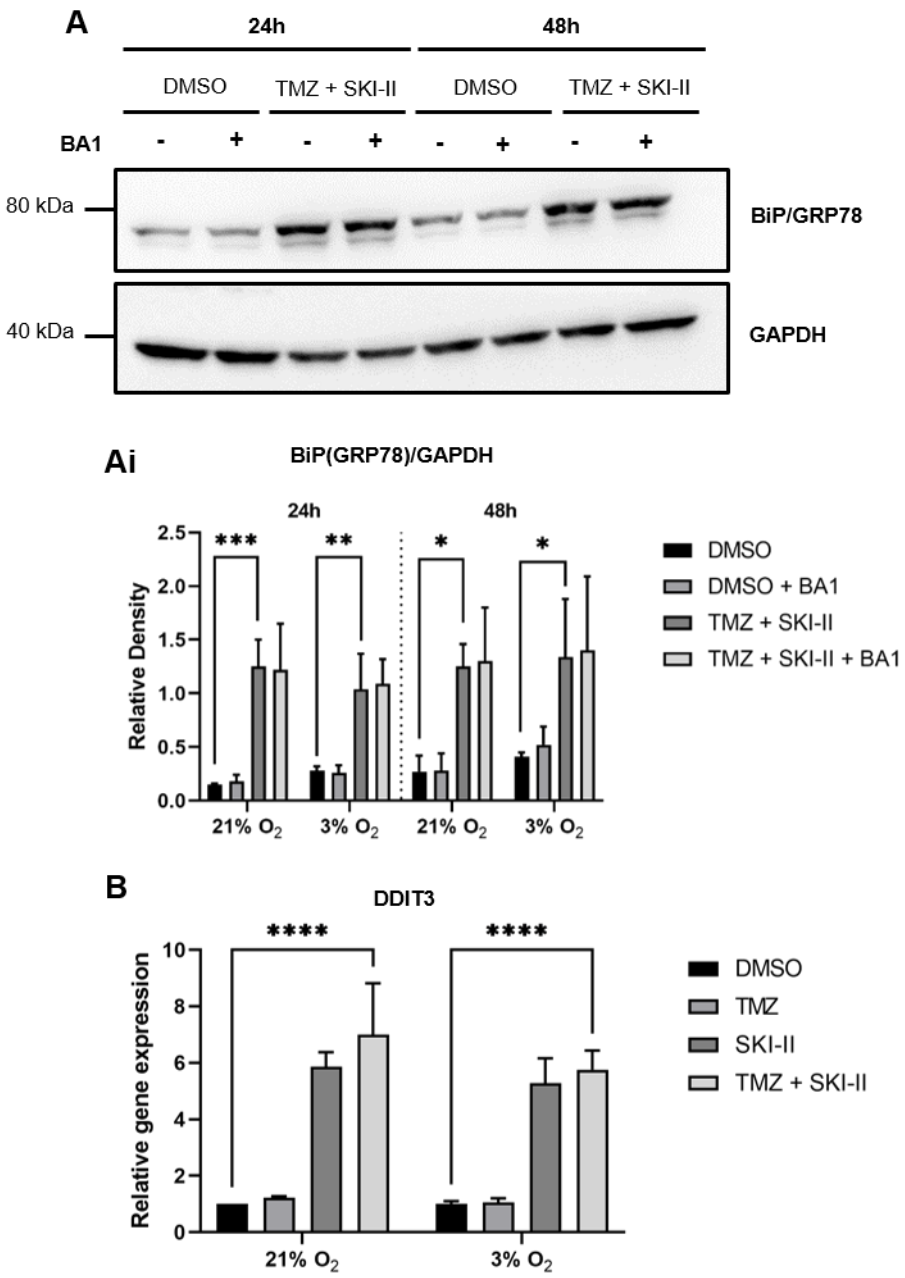

Figure 22 *- SKI-II alone and in combination with TMZ induces ER stress response. (A, Ai) Western Blot analysis of BiP/GRP78 in NCH82 cells treated with the vehicle control (DMSO) and 48 µM TMZ in combination with 2.66 µM SKI-II (TMZ + SKI-II) in absence or presence of Bafilomycin A (BA1), for 24- to 48 h under normoxia (21% O_2) and hypoxia (3% O_2). GAPDH was used as a loading control. (A) Representative blot of cells treated under 3% O_2. (Ai) BiP protein expression relative to GAPDH was quantified with ImageJ. (B) Gene expression analysis of DDIT3 in NCH82 cells treated accordingly for 24 h under normoxia (21% O_2) and hypoxia (3%*

O_2). Data represent mean (+ SD) of n = 3. Two-way ANOVA followed by Tukey's multiple comparisons test was performed for statistical analysis.

5.9. ER stress and cytotoxicity induced by the combination are peroxynitrite-dependent

ER stress and the generation of reactive oxygen and nitrogen species are linked events [92]. Peroxynitrite, a short-lived oxidant species produced by the reaction of nitric oxide with superoxide radicals, can induce ER stress via depletion of ER-Ca^{2+} [93]. Noack *et al.* previously reported that FeTPPS, a decomposition catalyst of peroxynitrite, protects NCH82 cells from ER stress and from death induced by a higher dose (TMZ + SKI-II) combination [84]. To determine the contribution of peroxynitrite to the ER stress and viability loss induced by lower doses of the (TMZ + SKI-II) combination, NCH82 cells were co-treated with 100 µM FeTPPS. Light microscopy revealed that cells treated with FeTPPS did not develop cytoplasmic vacuolization in the (TMZ + SKI-II) condition, as in the DMSO control (Figure 23, A). Mitigation of peroxynitrite significantly decreased BiP protein levels in (TMZ + SKI-II)-treated cells (Figure 23 B, Bi) as well as the number of dead cells induced by the treatment, under both normoxia and hypoxia (Figure 23 C). The mitigation of cytoplasmic vacuolization and ER stress by FeTPPS, further correlated ER stress to the formation of cytoplasmic vacuolization. Altogether, these results suggest that oxidative stress has an important role in ER stress and cell death induced by the combination.

5.10. SKI-II alone and in combination reduces the levels of ceramide and its metabolites

Next, in collaboration with Dr. Laura Bindila (Clinical Lipidomics Unit, Institute of Physiological Chemistry, Medical University Mainz, Mainz), I assessed the effects of the treatments on the sphingolipid metabolism by measuring the concentration of relevant metabolites in NCH82 cells. Treatment for 24h (not shown) and 48h (Figure 24) with SKI-II alone and in combination led to a significant decrease in ceramide (d18:1/16:0) in both oxygen conditions; the same trend was observed for ceramide (d18:1/24:1) with a significant decrease under hypoxia. The level of the ceramide precursor dihydrosphingosine (dihydroceramide was not detectable) was not significantly affected by the treatments. The ceramide/dihydrosphingosine ratio was reduced by SKI-II in both oxygen conditions. It was not affected by the combination under normoxia but was reduced under hypoxia. Sphingomyelin, ceramide-1-phosphate (C1P) and, to a lesser extent, sphingosine, which are all direct metabolites of ceramide, showed a profile similar to that of ceramide under normoxia and hypoxia. Similar to sphingosine, S1P levels were decreased by

SKI-II alone and in combination at 21% O2 (although not significantly) and remained unchanged at 3% O2. TMZ did not induce major alterations in the sphingolipid levels. Furthermore, none of the treatments significantly affected the basal level of expression of the genes coding for SK1, SK2, and DES1 in cells treated under either oxygen concentration (Figure 25, A). Altogether, these data suggest that changes in sphingolipid levels after treatment with SKI-II alone and in combination were primarily the consequences of changes in ceramide levels.

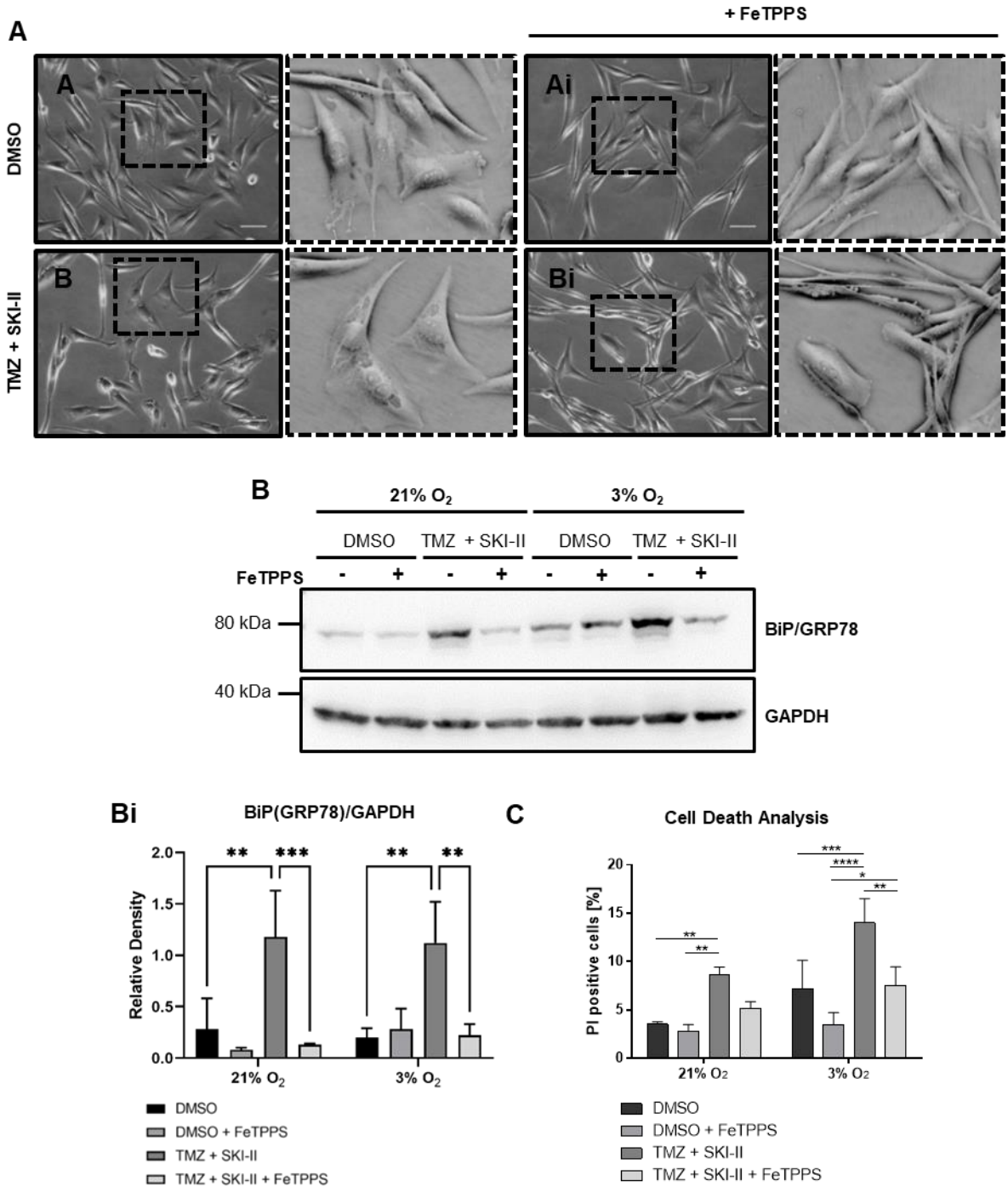

Figure 23 *- Peroxynitrite scavenger rescues the effects of the combination on cytoplasmic vacuolization, ER stress, and viability. (A) Light microscopy of NCH82 cells treated with the vehicle control (DMSO), and 48 µM temozolomide (TMZ) combined with 2.66 µM SKI-II (TMZ + SKI-II) for 24h at 3% O_2 in the presence and absence of FeTPPS. Scale bar: 100 µm. (B) Western blot analysis of BiP/GRP78 in NCH82 cells treated accordingly for 24h under normoxia (21% O_2) and hypoxia (3% O_2). FeTPPS was used at a final concentration of 100 µM. A representative blot*

is shown. (Bi) BiP/GRP78 protein expression level was quantified and normalized to GAPDH with ImageJ. (C) Viability of cells treated accordingly for 72h was determined via flow cytometry. Data represent mean (± SD) of n = 3. Two-way ANOVA followed by Tukey's multiple comparisons test was performed for statistical analysis.

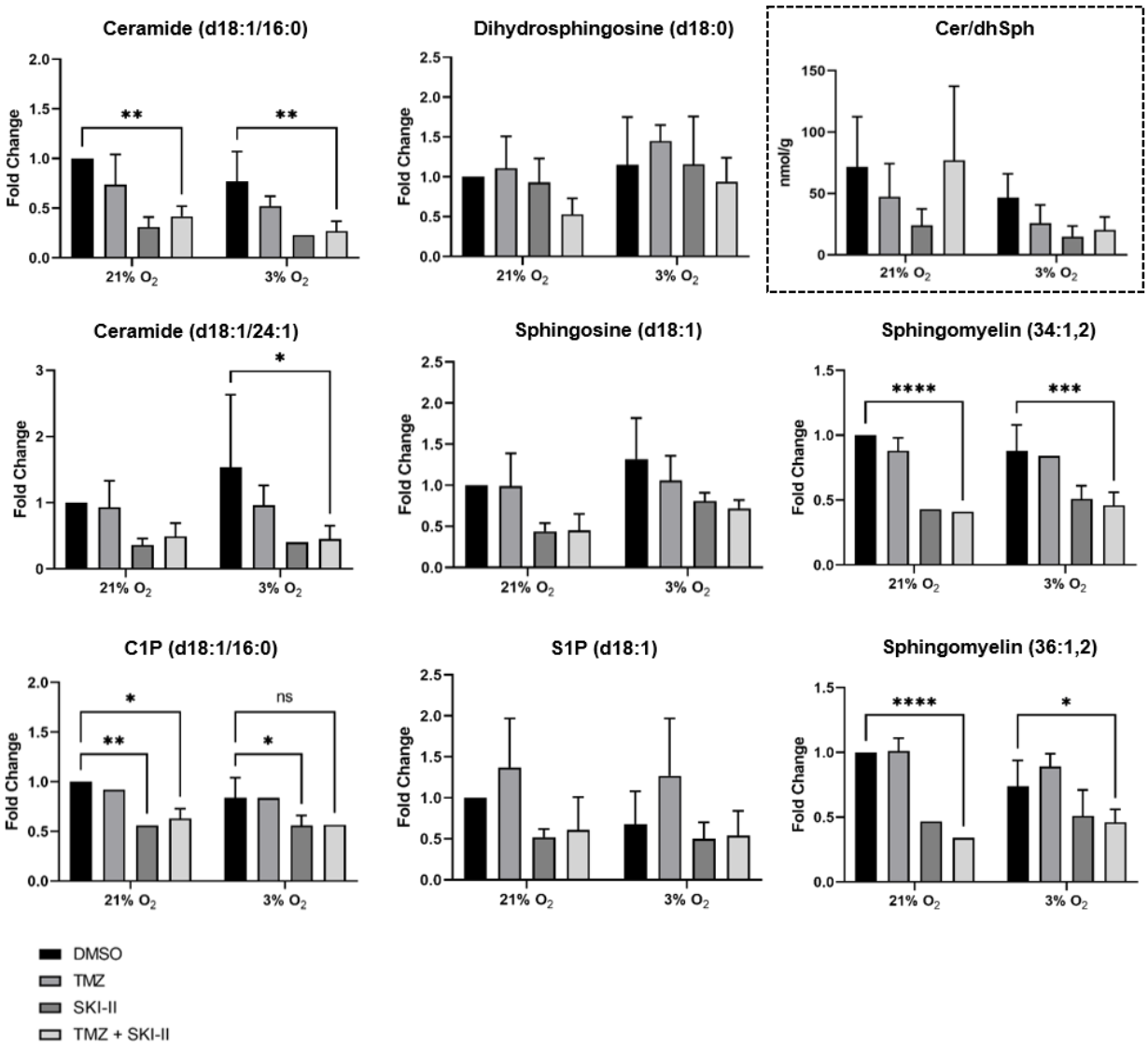

Figure 24 *- SKI-II alone and in combination with temozolomide (TMZ) reduces the levels of ceramide, and ceramide-derived metabolites. NCH82 cells were treated for 48h with the vehicle control (DMSO), 48 µM TMZ, 2.66 µM SKI-II and the combination (TMZ + SKI-II) under normoxia (21% O_2) and hypoxia (3% O_2). Sphingolipids were quantified via liquid chromatography mass spectrometry. Data are normalized as fold change ratio of treatment to DMSO control values and*

represent mean (+SD) of n = 3 (C1P, Ceramide-1-Phosphate, n = 2). The framed panel Cer/dhSph shows the ratio of Ceramide (d18:1/16:0) to dihydrosphingosine and indicates that SKI-II affects the flux of the de novo synthesis of ceramide. The ratio was determined from the mean (+ SD) of n=3. Two-way ANOVA followed by Tukey's multiple comparisons test was performed for statistical analysis. Amount of sphingolipid present in DMSO control cells at 21% O_2 (mean ± SD): C24-ceramide, 4791.2 ± 1790.9 nmol/g; C16-ceramide, 18128.9 ± 8185.5 nmol/g; C16-ceramide-1-phosphate, 16431 ± 221.3 nmol/g; sphingosine-1-phosphate, 81925.5 ± 33204.2 nmol/g; sphingosine, 656.6 ± 96.6 nmol/g; dihydrosphingosine, 283.1 ± 85.3 nmol/g; sphingomyelin 36:1,2, 975.1 ± 489.9 nmol/g; sphingomyelin 34:1,2, 35030.9 ± 8629.9 nmol/g.

5.11. SKI-II alone and in combination affects the expression levels of *S1PR1* and *CXCR4*

S1P receptor signaling is involved in cell proliferation and migration and has been shown to contribute to GB progression [94]. *CXCR4* is overexpressed in GB tissue and GSCs and is associated with reduced overall survival. High levels of *S1PR1*, the gene coding for the S1P receptor 1, and low levels of the chemokine receptor *CXCR4* have been reported to affect the migration of hematopoietic stem cells [95]. We analyzed the gene expression levels of the S1P receptor 1 (*S1PR1*) and *CXCR4* in NCH82 cells after treatment under normoxia and hypoxia (Figure 25, B). As expected from its regulation by HIF-1α, *CXCR4* expression, but not *S1PR1* expression, was increased in untreated and treated cells under hypoxia. TMZ did not affect the basal expression of *S1PR1* and *CXCR4* in both oxygen conditions. On the contrary, SKI-II alone and in combination significantly increased *S1PR1* expression while decreasing *CXCR4* expression, under both normoxia and hypoxia. A correlation between the increased *S1PR1* expression and cell viability of NCH82 cells in response to the treatments was tested by co-treatment with the S1PR1 antagonist W146 [96]. W146 did not recover the viability of (TMZ + SKI-II)-treated cells (Figure 25, C).

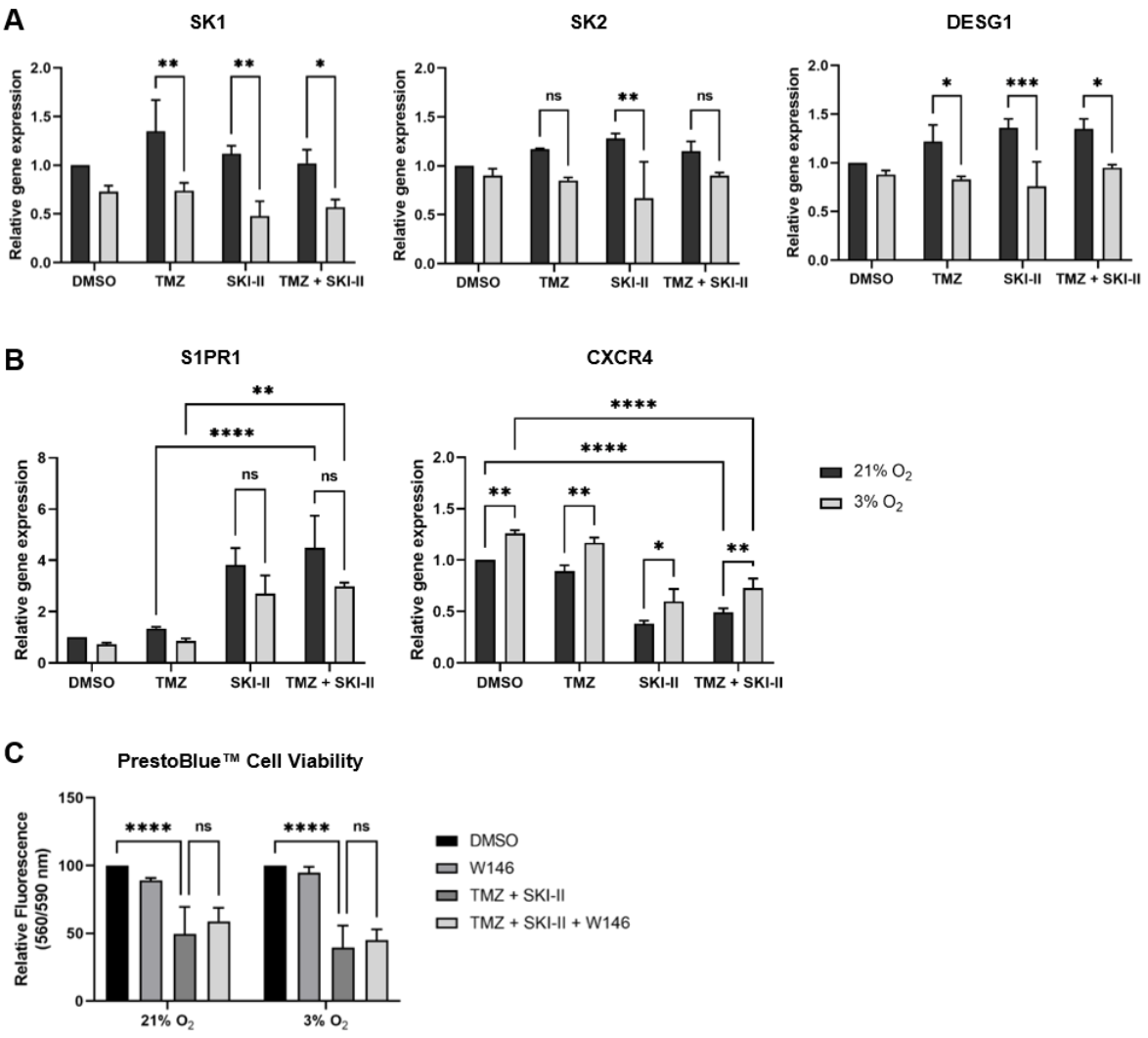

Figure 25 *- SKI-II alone and in combination with temozolomide (TMZ) inversely regulates* S1PR1 *and* CXCR4 *gene expression levels. (A, B) Gene expression analysis in NCH82 cells treated with the vehicle control (DMSO), 48 µM TMZ, 2.66 µM SKI-II and in combination (TMZ + SKI-II) for 24h under normoxia (21% O_2) and hypoxia (3% O_2) of* SK1 *(sphingosine kinase 1);* SK2 *(sphingosine kinase 2),* DESG1 *(dihydroceramide desaturase 1),* S1PR1 *(sphingosine-1-phosphate receptor 1) and* CXCR4 *(C-X-C motif chemokine receptor 4). (C) Metabolic activity of combination-treated cells unaffected by* S1PR1 *blockage via the* S1PR1 *selective antagonist W146 (10 µM). Cell viability was assessed via the resazurin-based assay PrestoBlue™ in NCH82 cells treated accordingly for 72h under normoxia and hypoxia. Data represent mean (+ SD) of n= 3. Two-way ANOVA followed by Tukey's multiple comparisons test was performed for statistical analysis.*

5.12. The combination of TMZ and SKI-II impairs self-renewal of human glioblastoma stem cells

The self-renewal potential of glioblastoma stem cells (GSCs) allows them to divide while maintaining a more malignant stem-like phenotype. Impairment of their self-renewal capacity would allow for a shift into a more differentiated state, turning them more susceptible to chemotherapy. To assess whether the (TMZ + SKI-II) combination affects the self-renewal capacity of GSCs under hypoxia and normoxia, I performed extreme limiting dilution analysis (ELDA). Limiting dilution assays allow the quantification of the frequency of biologically active cells in a population. I first used two GSC lines established by Dr. Ella Kim (Department of Neurosurgery, Medical University of Mainz, Mainz) [97]: the control line DMSO-1080 and the line TMZ-1080, selected for its resistance to 100 µM TMZ. TMZ alone had no effect in the stem cell frequency of both GSC lines in both oxygen conditions. The combination was as effective as SKI-II alone, but more beneficial in the impairment of the self-renewal than TMZ alone (not significantly in the DMSO-1080 line under normoxia) (Figure 26 A-Aii, B-Bii). The self-renewal capacity of TMZ-1080 cells was the most impaired by the combination, particularly under hypoxia: the stem cell frequently decreased almost 4-fold in comparison with SKI-II alone, yet it remained similar under normoxia (Figure 26 B, Bi, Bii).

The cytotoxic potential of single and combined treatments was examined towards DMSO-1080 and TMZ-1080 cells by Dr. Carsten Geiß (Institute of Developmental Biology & Neurobiology, Johannes Gutenberg University Mainz, Mainz) using flow cytometry (Figure 27), and by Dr. Ella Kim using immunofluorescence (Figure 28). As shown in Figure 27, a significant cell death induction could not be detected in both GSC lines after 5 days of TMZ treatment. A slight, though not significant, increase in cell death was detected after treatment with SKI-II alone under normoxia, but not under hypoxia. The combination led to a significant increase in cell death of DMSO-1080 cells at 21% O2, but not in any of the other conditions. There were no significant differences in the distribution of early apoptotic (AV-FITC$^+$/PI$^-$), late apoptotic (AV-FITC$^+$/PI$^+$) or necrotic (AV-FITC$^-$/PI$^+$) cells between the conditions. Immunofluorescence analysis of the GSC lines indicated the presence of cells dying via apoptosis as evidenced by morphological features and activation of caspase 3 (Figure 28). This however represented a low percentage of cells. Interestingly, there was a higher number of cleaved caspase-3 positive cells in TMZ-1080 cells when treated in combination under hypoxia – the same condition where a higher effect on the self-renewal was observed. Altogether these data indicate that SKI-II alone and in combination efficiently reduce the self-renewal capacity of the two GSC lines but did not show major cytotoxic effects after 5 days of treatment.

Gene expression analysis of the stem cell markers SOX2, Nestin and OLIG2, and HIF1α were performed in both GSC lines after 8 days of treatment under hypoxia and normoxia (Figure 29). The expression pattern was quite similar between all markers. TMZ increased the expression of all genes analyzed in DMSO-1080 cells, but not in TMZ-1080 cells. SKI-II reduced or kept the expression of all markers at basal level. Strikingly, in TMZ-1080 cells treated with the combination under hypoxia (the condition where the highest impairment on the stem cell frequency was observed (Figure 29 B, Bi, Bii)), the expression of all markers was much higher in comparison with normoxia, and DMSO-treated cells in both oxygen conditions.

Next, I isolated the stem-like cell population of the NCH82 line by culturing these cells in serum-free media (see *Materials & Methods* section). I hereafter refer to these cells as NCH82 neurospheres. To determine whether these cells acquired a stem-like transcriptional profile, I analyzed the gene expression of several known GSC markers (Figure 30). The expression of *SOX2*, *Nestin*, *CD133*, *CXCR4, AQP4 and NANOG* was highly upregulated in NCH82 neurospheres in comparison with NCH82 cells cultured as monolayers (serum culture). On the contrary, *OCT4*, *NEUROD1* and *OLIG2* levels decreased in NCH82 neurospheres. ELDA analysis under normoxia (21% O_2) revealed that the (TMZ + SKI-II) combination significantly impaired the self-renewal capacity of NCH82 neuropheres in comparison with DMSO and single treatments (Figure 31). The combination was more efficient in decreasing the stem cell frequency than TMZ alone by approximately 26-fold and, than SKI-II alone by almost 8-fold. TMZ alone had no effect in the stem cell frequency of NCH82 neurospheres, as it was similar to the DMSO condition (Figure 31, B, C). NCH82 neurospheres treated with SKI-II alone and in combination with TMZ reduced the expression of genes known to maintain GSCs such as *Nestin*, *SOX2*, *CXCR4* and *CD133*. However, hypoxia counteracted this effect and increased the expression of *CXCR4* and *CD133* (Figure 32).

A

DMSO-1080

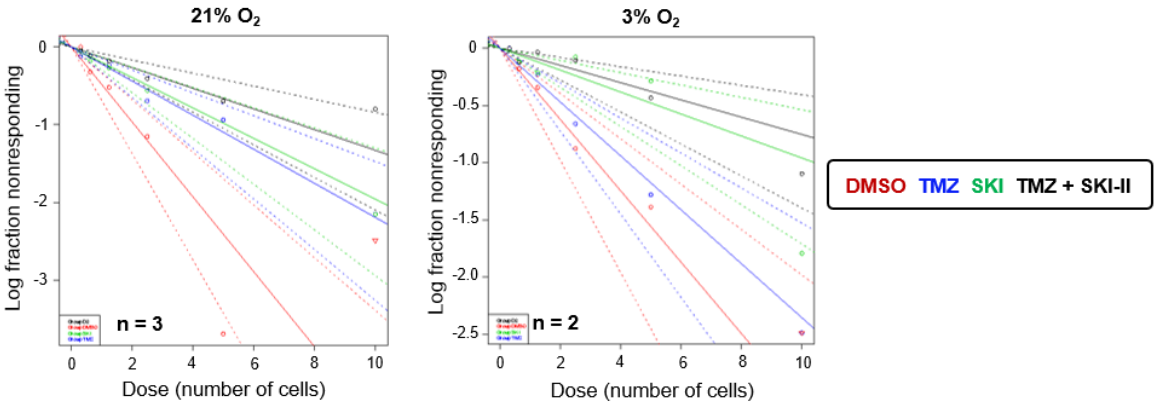

Ai 1/(stem cell frequency)

DMSO-1080	21% O2	3% O_2
DMSO	2.08	3.21
TMZ	4.57	4.25
SKI-II	5.12	10.43
TMZ + SKI-II	7.53	13.28

Aii Pairwise test for differences in stem cell frequencies

DMSO-1080		21% O2	3% O_2
Group 1	Group 2	Pr (>Chisq)	Pr (>Chisq)
	DMSO	5.32e-06	0.000176
TMZ + SKI-II	TMZ	0.0978	0.00221
	SKI-II	0.206	0.582

B

TMZ-1080

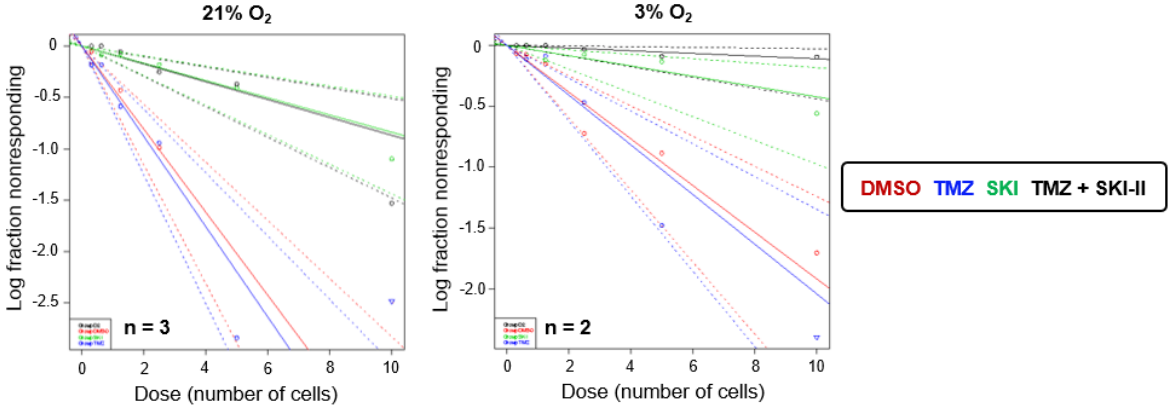

Bi 1/(stem cell frequency)

TMZ-1080	21% O2	3% O_2
DMSO	2.47	5.21
TMZ	2.28	4.90
SKI-II	11.91	23.66
TMZ + SKI-II	11.51	90.67

Bii Pairwise test for differences in stem cell frequencies

TMZ-1080		21% O2	3% O_2
Group 1	Group 2	Pr (>Chisq)	Pr (>Chisq)
	DMSO	8.2 e-07	6.2 e-08
TMZ + SKI-II	TMZ	1.41 e-07	2.31 e-08
	SKI-II	0.931	0.0803

Figure 26 - *SKI-II in combination with TMZ impairs the self-renewal capacity of TMZ-resistant glioblastoma stem cells (GSCs) under hypoxia. Stem cell frequency was determined by extreme limiting dilution assay (ELDA) in (A-Aii) DMSO-selected 1080 GSCs and (B-Bii) TMZ-selected 1080 GSCs. Cells were treated with the DMSO control (red line), 48 µM TMZ (blue line), 2.66 µM SKI-II (green line) and the combination (TMZ+SKI-II) (black line) for 4 weeks under normoxia (21% O_2; n = 3) and hypoxia (3% O_2; n = 2). (A, B) Log-fraction plots, where the y axis "log fraction nonresponding" indicates frequency of cells incapable of forming clonal spheres and the x axis "dose (number of cells)" indicates number of cells per mL. The slope of the line is the log-active cell fraction, and dotted lines give the 95% confidence interval. Note that the panels in A and B have slightly different Y-axis scales. (Ai, Bi) Estimated stem cell frequency, 1/(stem cell frequency). (Aii, Bii) Pairwise test for differences in stem cell frequencies between groups. Data analysis was performed via the ELDA webtool.*

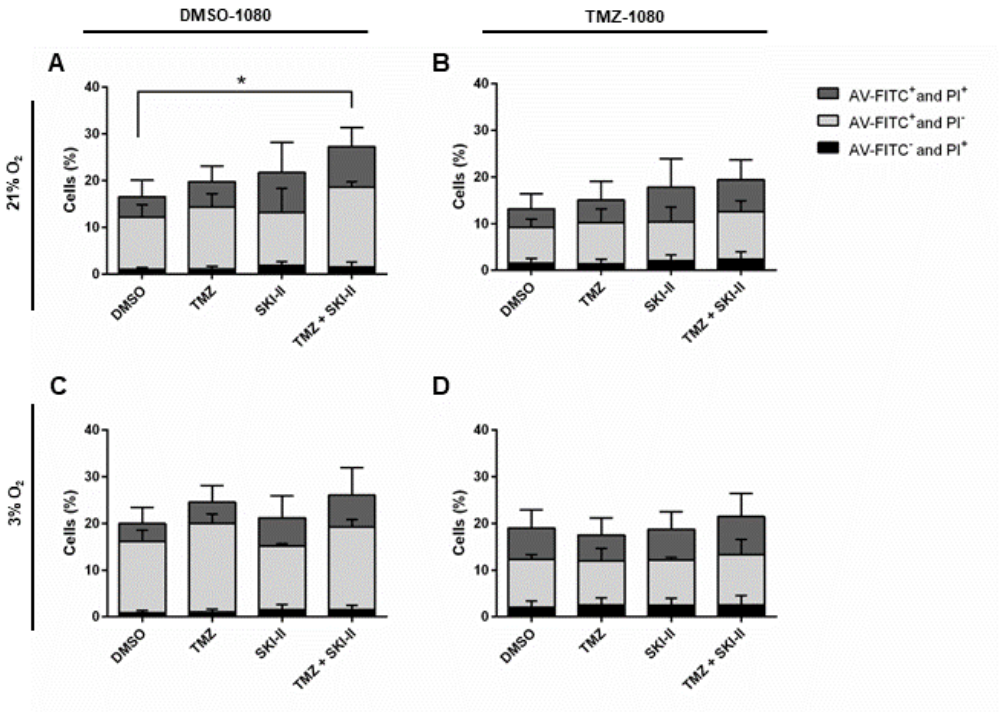

Figure 27 *- Cytotoxic effect of the combinations in glioblastoma stem cells (GSCs). The 1080-DMSO and 1080-TMZ GSC lines were analyzed by flow cytometry after treatment with vehicle control (DMSO), 48 µM TMZ, 2.66 µM SKI-II, and the combination (TMZ + SKI-II) for 5 days under normoxia (21% O_2) and hypoxia (3% O_2). Quantification of PI- and AV-FITC-labeled GSCs was performed using the software FlowJo. Data are presented as percent of total cells; n = 3.*

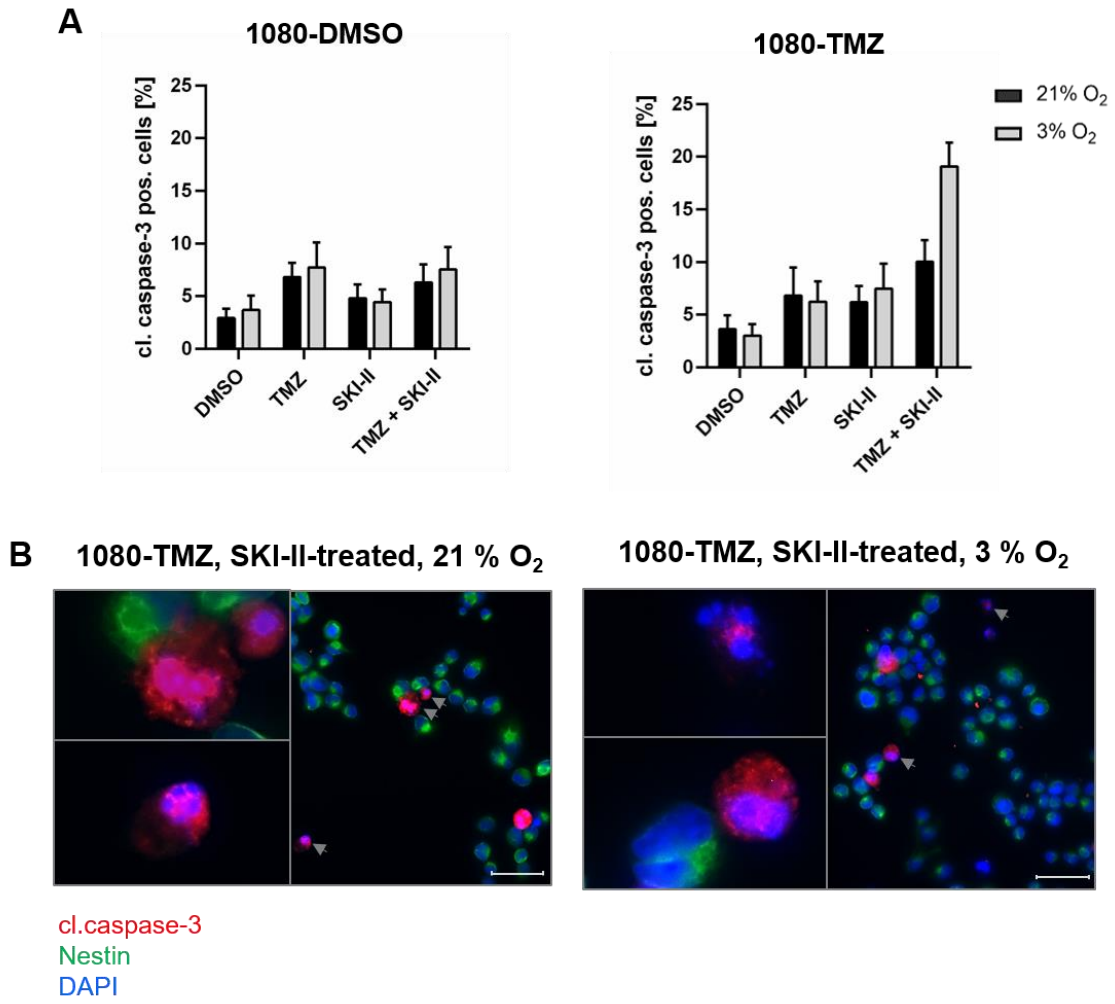

Figure 28 *- Detection of cleaved caspase-3 in treated glioblastoma stem cells (GSCs) by immunofluorescence. DMSO-1080 and TMZ-1080 GSCs plated on ornithin-coated glass coverslips were treated with 2.66 µM SKI-II, 48 µM temozolomide (TMZ) and the combination (TMZ+SKI-II) in triplicates. After 5 days of incubation, cells were fixed with 4% paraformaldehyde and stained for cleaved caspase-3, Nestin and Dapi. (A) Quantification of cleaved caspase-3 positive cells. Data are presented as percent of total cells counted in 7 to 9 regions of triplicates, and for a total number of cells of 700 to 1100. (B) Representative images of apoptotic cells in 1080-TMZ cells treated with SKI-II under normoxia (top) or hypoxia (bottom panel). Magnification 40 x, scale bar 50 µM. Left panels: enlarged images of apoptotic cells (marked by arrows) manifesting morphological hallmarks of apoptosis such as chromatin condensation and cytoplasmic disintegration. n = 1*

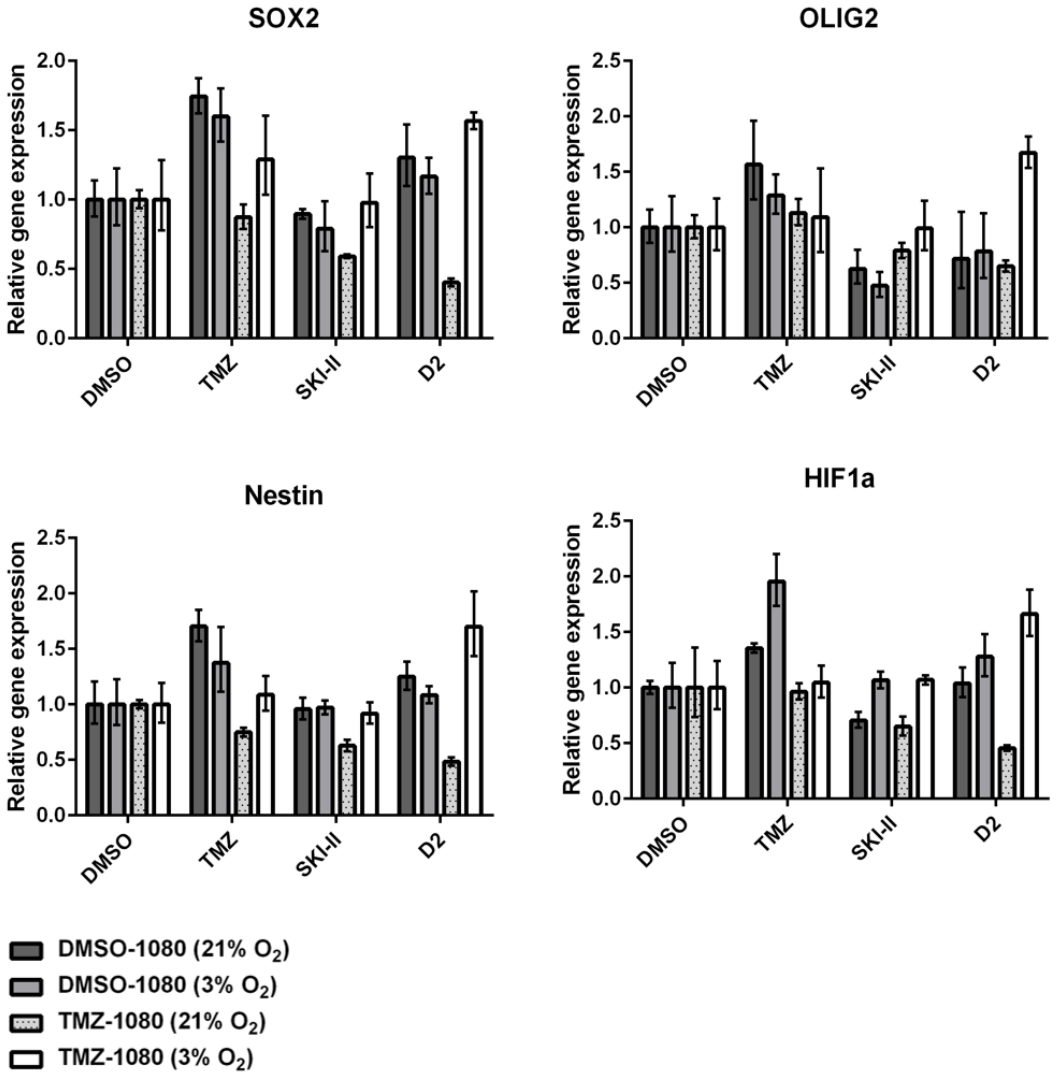

Figure 29 *- Gene expression analysis of the glioblastoma stem cells (GSC). Cells from the GSC lines DMSO-1080 and TMZ-1080 were treated for 8 days under normoxia (21% O_2) and hypoxia (3% O_2) and further analyzed via real-time quantitative PCR to quantify the expression level of stem cell markers (SOX2, OLIG2 and Nestin) and the hypoxia-inducible factor 1 alpha (HIF1α). Data represent mean (± SD) of triplicates, n=1.*

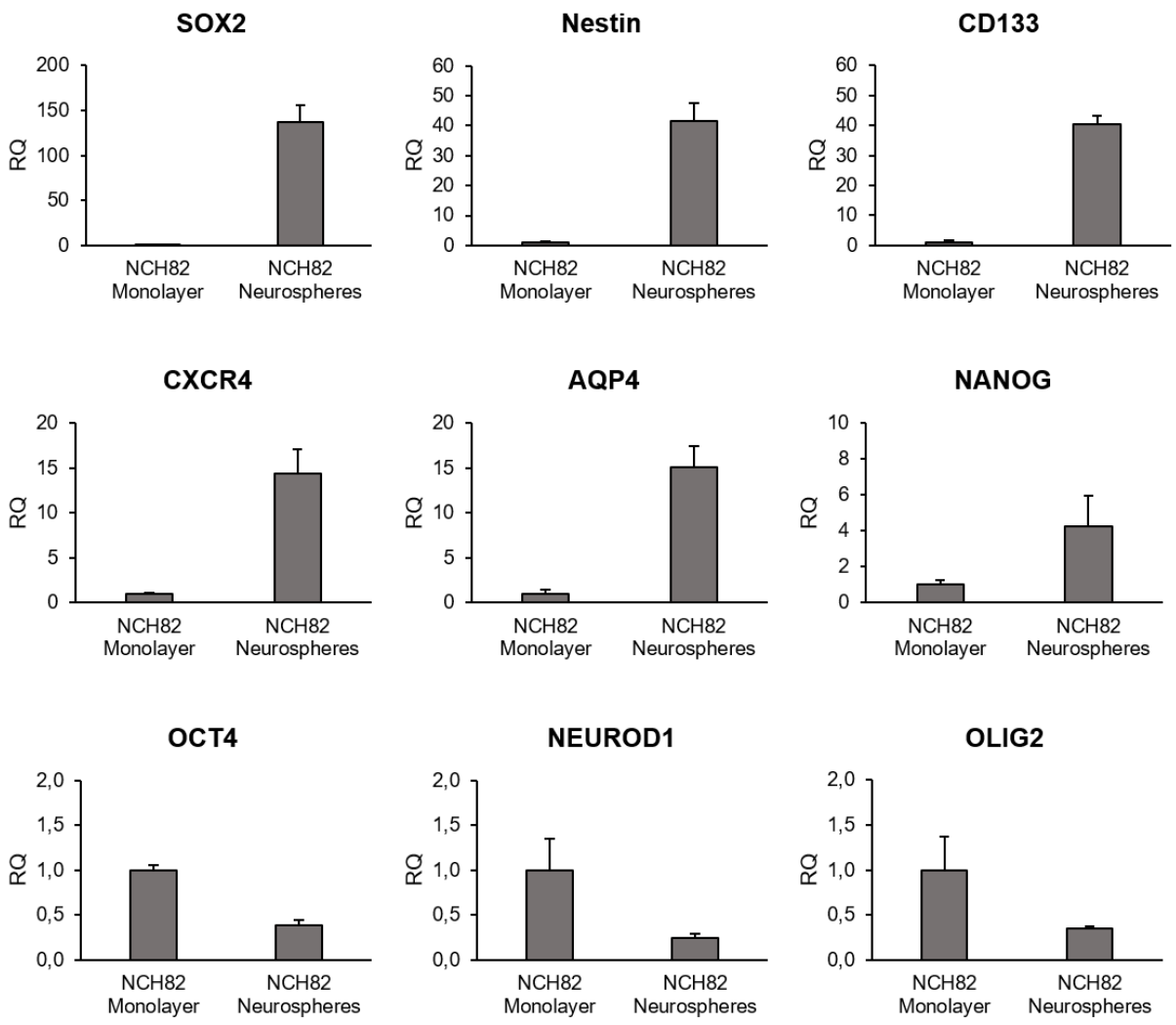

Figure 30 *- NCH82 neurospheres have increased expression of stem cell markers. Gene expression analysis of stem cell markers in NCH82 cells cultured as monolayers (serum culture) and as neurospheres (serum-free culture) under normoxia. RQ, relative quantification of n=1.*

A

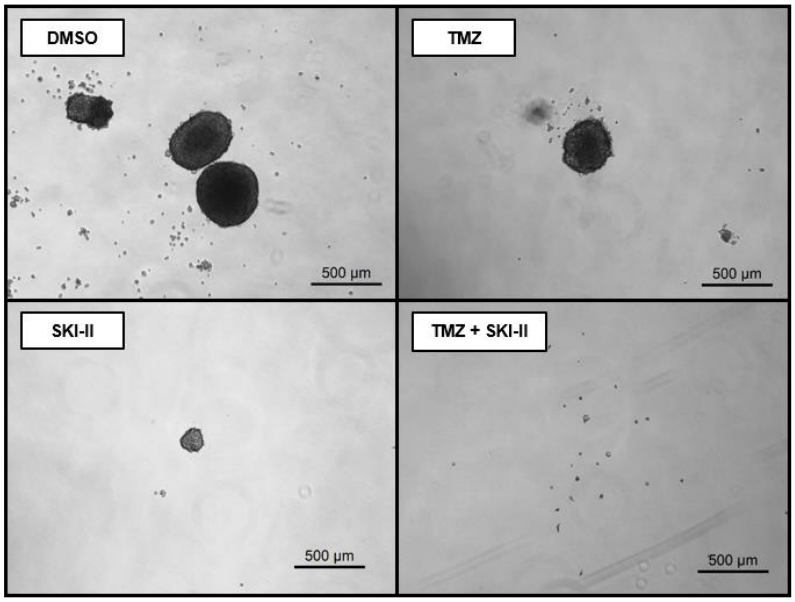

B

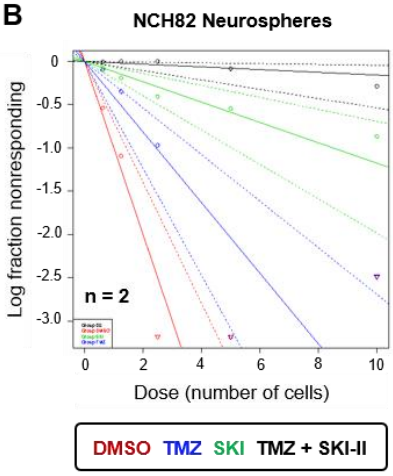

C

1/(stem cell frequency)

Group	Lower	Estimate	Upper
DMSO	1.43	1.00	1.00
TMZ	3.71	2.45	1.62
SKI-II	14.34	8.50	5.03
TMZ + SKI-II	216.89	63.41	18.54

D

Pairwise test for differences in stem cell frequencies

Group 1	Group 2	Pr (>Chisq)
	DMSO	7.57e-22
TMZ + SKI-II	TMZ	4.62e-12
	SKI-II	0.00037

Figure 31 *- SKI-II in combination with TMZ impairs the self-renewal capacity of NCH82 neurospheres. Stem cell frequency was determined by extreme limiting dilution assay (ELDA) in NCH82 neurospheres. Cells were treated with the DMSO control (red line), 48 µM TMZ (blue line), 2.66 µM SKI-II (green line) and the combination (TMZ+SKI-II) (black line) for 4 weeks under normoxia (21% O_2). (A) Light microscopy of formed neurospheres after treatment for 4 weeks at an initial cell density of 10 cells/mL. (B) Log-fraction plot, where "log fraction nonresponding" indicates frequency of cells incapable of forming clonal spheres and "dose (number of cells)" indicates number of cells per mL. The slope of the line is the log-active cell fraction, and dotted lines give the 95% confidence interval. (C) Estimated stem cell frequency, 1/(stem cell frequency). (D) Pairwise test for differences in stem cell frequencies between groups. Data analysis was performed via the ELDA webtool.*

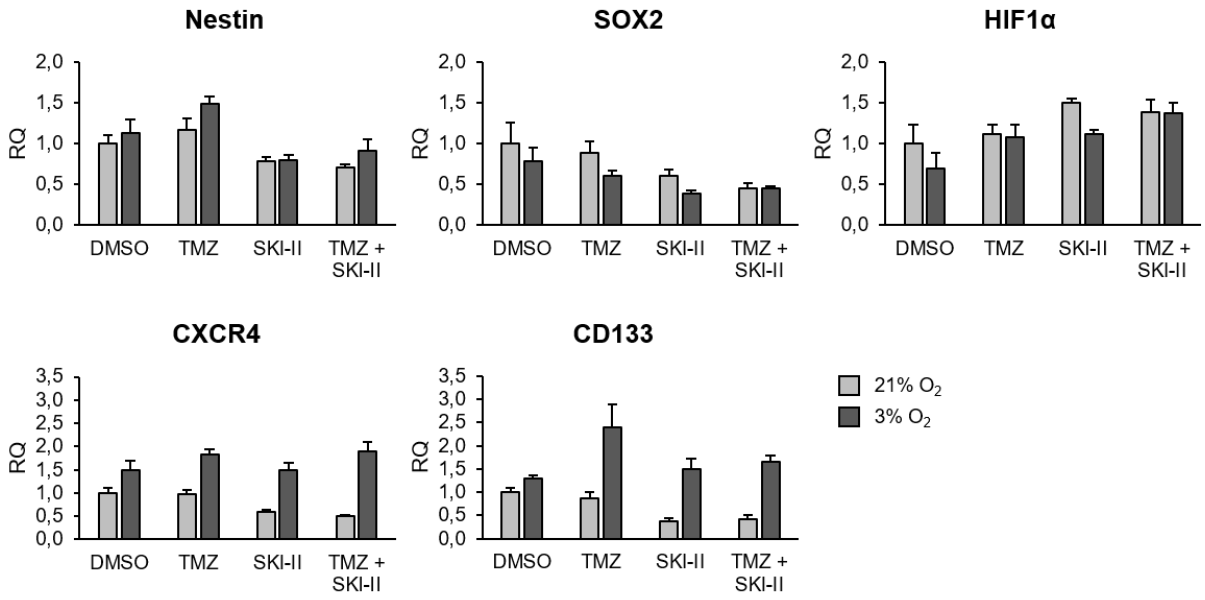

Figure 32 *- Gene expression analysis of NCH82 neurospheres after SKI-II and TMZ treatment. NCH82 neurospheres were treated for 12 days under normoxia (21% O_2) and hypoxia (3% O_2) and further analyzed via real-time quantitative PCR to quantify the expression level of stem cell markers (Nestin, SOX2, CXCR4 and CD133) and the hypoxia-inducible factor 1 alpha (HIF1α).*

5.13. SKI-II alone and in combination impairs invasion of mesenchymal MGMT-positive glioblastoma cells

Tumor cell invasion into the surrounding tissue is a hallmark feature of GB. Invasive GB cells can escape surgery and contribute to tumor relapse by recolonization of the primary tumor site or colonization of distant areas. The mesenchymal GB subtype is considered to be particularly aggressive and invasive, and patients have a poorer prognosis [23,25]. By comparing invasion of spheroids generated from U3054 cells (mesenchymal subtype)[69] (Figure 33 A, Ai) and U3047 cells (proneural subtype)[69] (Figure 33 B, Bi), I confirmed that the mesenchymal GB line was about 2.5-fold more invasive, and thus a suitable cell model to study invasion. Cell arrangement as spheroids allows to better mimic *in vivo* conditions, such as appearance of gradients of nutrients, oxygen and catabolites, that cannot be recapitulated in monolayer cultures. U3054 cells were then used to analyze the effect of the single treatments and combination on the invasion capacity under normoxia and hypoxia using the 3D-spheroid model. The U3054 line is derived from a recurrent GB and is MGMT-positive (Figure 34 A). Altogether these features suggest that these

cells might be resistant to TMZ therapy [98]. Indeed, TMZ treatment did not affect the invasion capacity of U3054 spheroids, as it was similar to the DMSO control. In contrast, treatment with SKI-II alone and in combination reduced invasion by about 30- to 40% after 5 days under hypoxia and normoxia, respectively (Figure 34 B, Bi, C). Hypoxia *per se* reduced the invasion capacity of the U3054 cells in the collagen matrix and the combination was slightly less efficient in impairing invasion.

To understand the molecular mechanism by which SKI-II alone and in combination with TMZ reduces invasion, gene expression analysis was performed in U3054 spheroids treated for 5 days (Figure 35). Markers related to invasion and the epithelial-mesenchymal transition (EMT) were analyzed: carbonic anhydrases (CA) 9 and 12, metalloproteases (MMP) 2 and 9, TGFβ and downstream players TWIST1 and SNAIL1. Treatment did not cause significant changes in the expression of these genes. However, SKI-II alone and in combination tended to slightly decrease the expression of CA9 and increase the expression of CA12.

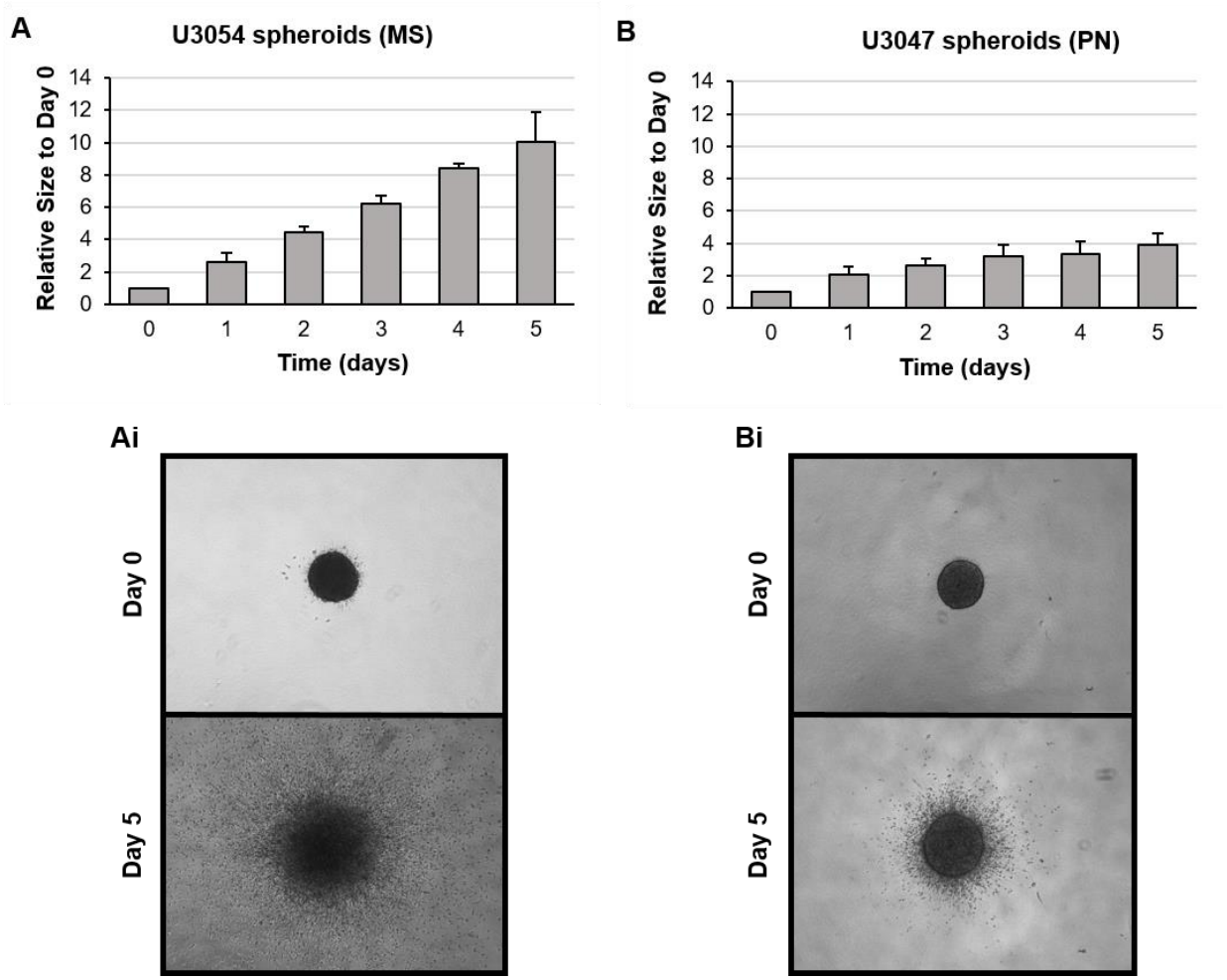

Figure 33 *- The recurrent mesenchymal glioblastoma cell line U3054 is highly invasive. (A, B) The spheroid invasion assay was performed with U3054 cells (mesenchymal (MS) GB) and U3047 (proneural (PN) GB). Quantification of the invaded area was performed using the Spheroid Analyzer (CLADIAC) as described in Material and Methods. (Bi) Light microscopy images of treated U3054 spheroids and respective surface plots (Ai, Bi) Light microscopy images at 5X magnification were collected at the time the spheroids were embedded (day 0) and 5 days later. Data represent mean (+ SD) of n=1.*

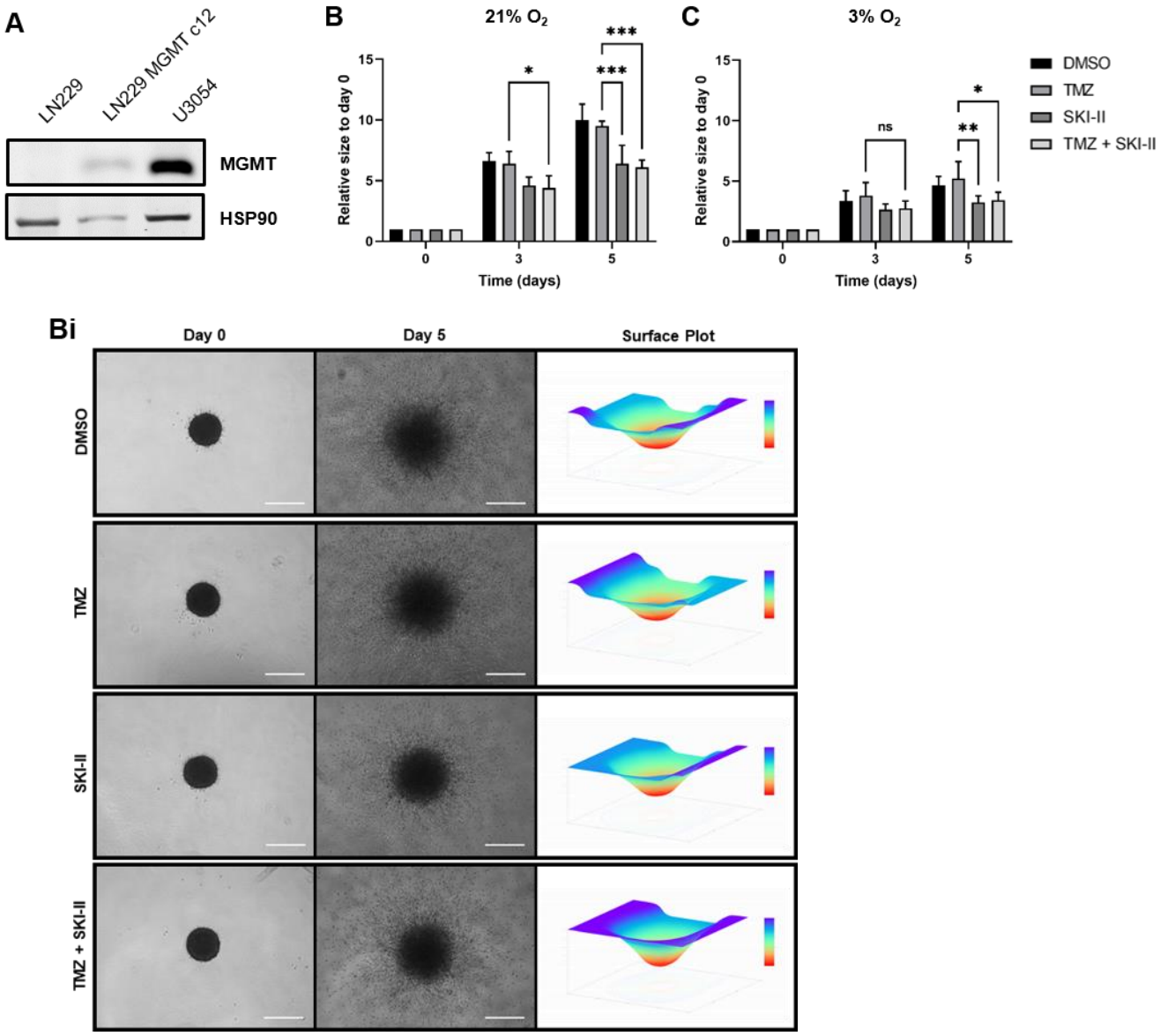

Figure 34 *- SKI-II alone and in combination with temozolomide (TMZ) impairs invasion of MGMT-positive glioblastoma cells. (A) Western blot analysis of MGMT (O6-methylguanine-DNA methyltransferase) and HSP90 in LN229 (negative control), LN229 MGMT c12 (positive control) and in U3054 cells. (B, C) The spheroid invasion assay was performed with U3054 cells (mesenchymal GB) treated with vehicle control (DMSO), 48 µM TMZ, 2.66 µM SKI-II, and the combination (TMZ + SKI-II) for up to 5 days under normoxia (21% O_2) and hypoxia (3% O_2). Quantification of the invaded area was performed using the Spheroid Analyzer (CLADIAC) as described in Material and Methods. (Bi) Light microscopy images of treated U3054 spheroids and*

respective surface plots. Data represent mean (± SD) of n = 3. Two-way ANOVA followed by Tukey's multiple comparisons test was performed for statistical analysis. Scale bar = 500 µm.

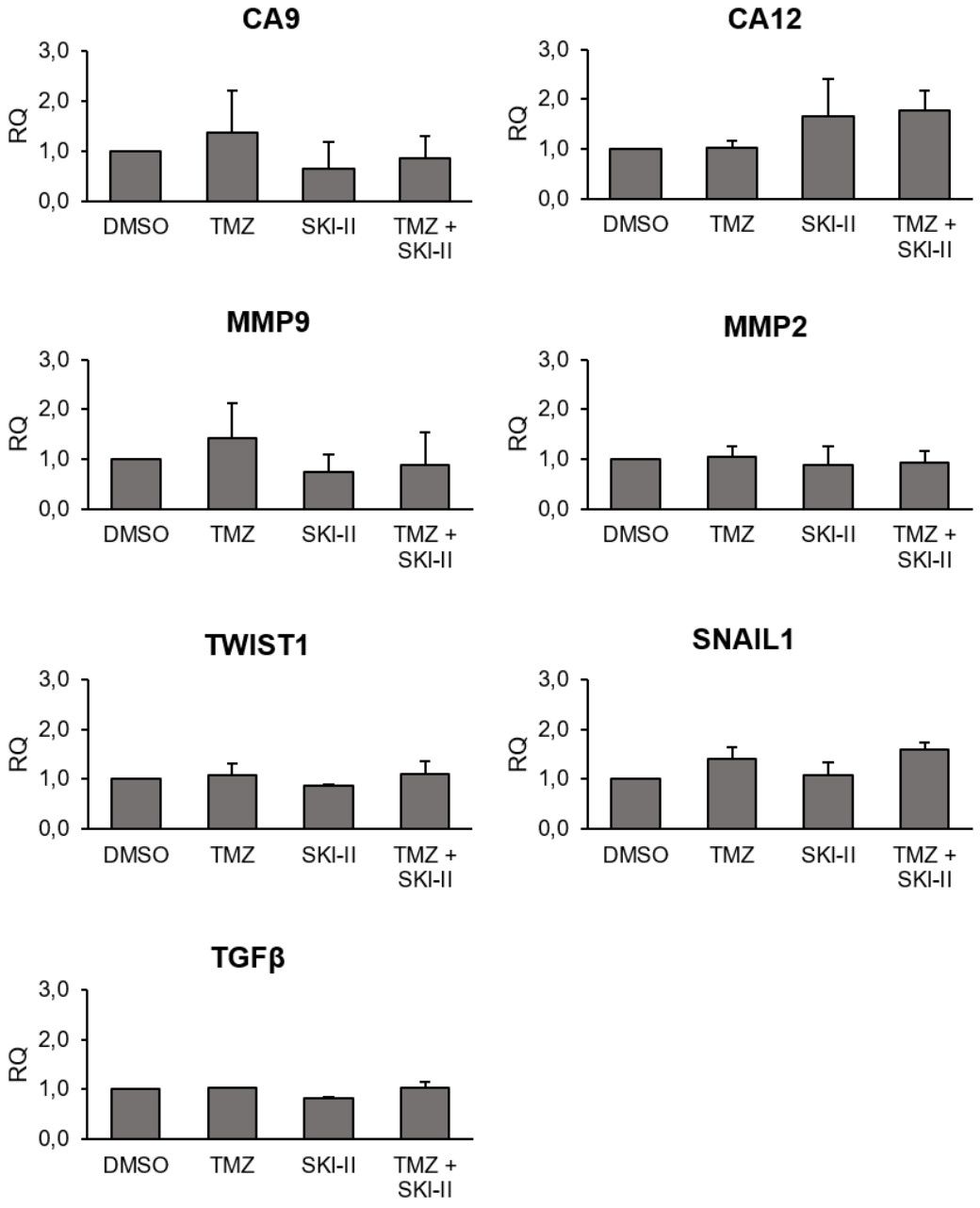

Figure 35 *- Gene expression analysis of U3054 spheroids treated under normoxia. U3054 spheroids were treated in a collagen matrix with 48 µM temozolomide (TMZ), 2.66 µM SKI-II, the combination (TMZ + SKI-II) and vehicle control (DMSO). After 5 days under 21% O_2, the U3054 spheroids were digested from the collagen matrix and analyzed via real-time quantitative PCR to*

*quantify the expression level of invasion associated markers: carbonic anhydrases (*CA9 *and* CA12*), metalloproteases (*MMP9 *and* MMP2*) and EMT process (*TWIST1, SNAIL1 *and* TGFβ*). Data represent mean (+ SD) of n=2. RQ, relative quantification.*

6. DISCUSSION

6.1. Combining TMZ with SKI-II has several potential therapeutic advantages

Two notorious roadblocks to effective glioblastoma (GB) therapy are triggered by hypoxia, a hallmark of tumors: chemotherapy resistance and expansion of glioblastoma stem cells (GSCs). In this *in vitro* study, I demonstrated that combining a clinically relevant dose of TMZ with SKI-II, an inhibitor of three enzymes of the sphingolipid metabolism, can alleviate these blocks. The hypoxia-induced resistance to TMZ in GB cells was effectively overcome by the combination as demonstrated by the combination index analysis. The latter shows that treatment with 48 µM TMZ combined with 2.66 µM SKI-II (referred to as "D2 combination", Table 7) under hypoxia allowed to drastically reduce the dose of TMZ that would have been necessary to achieve the same high efficacy if TMZ would have been used as single treatment. TMZ in combination with SKI-II was more effective than TMZ single treatment in inhibiting cell growth, inducing cell death, reducing invasion of mesenchymal GB cells (U3054 cell line) and impairing the self-renewal of GSCs (DMSO-1080 and TMZ-1080 cells) under hypoxia. SKI-II alone was as effective as in combination in impairing cell invasion and GSC self-renewal, but not in inhibiting cell growth (as shown by synergism in combination) and inducing cell death (as shown by enhancement in combination). This demonstrates that in combination we leverage the cytotoxic and cytostatic capabilities of TMZ.

Studies have shown that the serum concentration of TMZ is in the range of 20-70 µM [99], whereas the intratumoral TMZ concentration is in the range of 3-35 µM [100]. In the present study, I could directly compare the cytotoxic effects of various combinations of doses of TMZ and SKI-II on the NCH82 and LN18 cell lines and made the following observations: the combination used throughout the study (D2 combination, Table 7) was slightly more effective than the D3 combination (96 µM TMZ and 2.66 µM SKI-II), indicating no advantage of using a higher TMZ dose in NCH82 cells. Combinations with even a very low TMZ dose were able to cause major cytotoxic effects in GB cells: the D1 combination (24 µM TMZ and 2.66 µM SKI-II) induced similar effects as the D2 combination (48 µM TMZ and 2.66 µM SKI-II) and with a comparable degree of synergy. NCH82 cells have low MGMT activity (11.5 ± 0.3 (SD) fmol/mg) compared to other GB cell lines such as the LN18 (249 ± 10.6 (SD) fmol/mg; our own unpublished data) and are wild-type for p53 [101]. Thus, lower doses of TMZ are expected to be more effective in these cells [102]. Interestingly, LN18 cells, which have a high MGMT activity and mutated p53, were more sensitive to TMZ treatment than NCH82 cells in both oxygen conditions. Additionally, TMZ and SKI-II combination analysis revealed that in these cells, SKI-II as a monotherapy at a lower dose than

the one used with the D2 combination would have been sufficient to achieve the same efficacy as in combination. This confirms that DNA repair via the MGMT enzyme is a resistance mechanism not to be considered alone. Alterations in other tumor suppressor genes, such as PTEN (phosphatase and tensin homologue), are also known to decrease responsiveness to chemotherapy. In contrast to LN18 cells, NCH82 cells have a PTEN deletion. The loss of PTEN function has been associated with resistance to radio- and chemotherapy in glioma cells [103]. Additionally, there are other factors that could contribute to TMZ resistance [104].

I also showed that resistance to TMZ potentially conferred by MGMT expression was alleviated by the combination, as demonstrated by the reduced invasion capacity of serum-free and MGMT-positive U3054 GB cells. This reduced capacity could indicate a decrease in motility or reflect reduced proliferation and/or increased cell death. Gene expression analysis in treated spheroids of invasion- and EMT-related markers did not provide robust insights on the molecular pathways behind this effect. An interesting observation was the tendency of SKI-II alone or in combination to reduce the expression of carbonic anhydrase (CA) 9 and increase the expression of CA12. Acidosis of the tumor microenvironment is typical of a malignant phenotype, particularly in hypoxic tumors, such as GB. CAs, which catalyze the reversible hydration of cell-generated carbon dioxide into protons and bicarbonate ions, can counteract acidosis through the regulation of the intracellular pH, promoting tumor cell survival[105]. CA9 is highly expressed in GB tissue samples and is associated with a poorer prognosis [106]. CAs are upregulated by hypoxia, but in contrast to CA9, CA12 is not directly controlled by HIF1α. So, how could SKI-II potentially regulate the expression of CAs? One hypothesis is via HIF1α regulation. Ader *et al.* (2008) showed that SK1 stabilizes HIF1α through the Akt/GSK3h pathway and prevents its pVHL-dependent proteasomal degradation[107]. The authors demonstrated that pharmacologic or genetic inhibition of SK1 activity prevents HIF1α accumulation in various human cancer cell lines. Thus, SKI-II could potentially mimic this effect, thereby reducing the expression of CA9. The increase in CA12 expression could reflect a compensation for the downregulation of CA9, as previously reported[105]. Further experiments are needed to unravel the molecular mechanisms behind the effect of SKI-II in invasion. A bottleneck in experimentation with spheroids is the low number of cells available, which did not allow for western blot analysis, limiting the understanding of such mechanisms at the protein expression level. Altogether, the data suggest that using SKI-II and TMZ in combination at clinically relevant doses could potentially result in an increased therapeutic efficacy in GB cells with (high) MGMT activity.

GSCs are a proportion of cells within the bulk tumor that are similar to normal stem cells in their ability to self-renew and differentiate into downstream lineages. Additionally, in contrast to the non-GSCs counterpart, GSCs exhibit tumor-initiating potential. TMZ has shown to contribute to replenish the GSC subpopulation by promoting the conversion of differentiated tumor cells into GSCs, a process referred to as dedifferentiation [108]. Tumor hypoxia is also known to contribute to the maintenance of cancer stem cells and dedifferentiation [109]. GSC's plasticity is regarded as a mechanism of therapeutic resistance and relapse. Impairment of self-renewal could lead to a reduced resistance to therapy. Indeed, as already mentioned, the combination reduced the self-renewal capacity of the two GSC lines I tested and, particularly that of TMZ-resistant GSCs under hypoxia. The combination however did not exhibit significant cytotoxic effects towards DMSO-1080 and TMZ-1080 GSC cell lines after 5 days of treatment. Considering that processing of O6-methylguanine into DNA double-strand breaks requires two rounds of replication [110], a longer treatment time with the combination might be required to observe cytotoxic effects, as the doubling time of these cells might be longer than differentiated cells such as NCH82 (which have a doubling time of 48h, own unpublished data). A hypothesis for the higher effect of the combination in reducing the self-renewal capacity of TMZ-resistant GSCs (TMZ-1080) under hypoxia is the following: cancer (stem) cells adapt/thrive on levels of ROS that are moderately higher than those in their normal counterparts, as they have developed increased antioxidant systems. This feature renders cancer cells more sensitive to external stimuli that further increase the production of ROS, such as SKI-II[111]. Hypoxia and TMZ treatment further contribute to oxidative stress. Cancer cells that are resistant to TMZ rely even more on efficient antioxidant defense mechanisms for survival, making them more susceptible to further oxidative damage induced by exogenous agents that promote ROS production or inhibit antioxidant systems[112,113]. Preliminary gene expression analysis revealed an upregulation of stem-cell markers specifically in this condition. This could represent an attempt of the cells to replenish their protein levels.

The chemokine receptor CXCR4 is known to promote stemness, invasion and enhance resistance to chemotherapy [114,115]. Interestingly, treatment with SKI-II alone and in combination in NCH82 cells downregulated the gene expression of CXCR4, while upregulating that of the S1P receptor 1 (S1PR1). Increased expression of *S1PR1* correlated with prolonged survival of GB patients in two studies [116,117]. A correlation between high levels of *S1PR1* and low *CXCR4* levels has been previously shown to affect the migration of hematopoietic stem cells [95]. CXCR4 and its crosstalk with S1P signaling deserves further attention to better understand the effects of the combination in GB cells and GSCs.

6.2. Interplay between the sphingolipid metabolism and cell death

In this study we used the sphingosine kinase inhibitor SKI-II to alter sphingolipid metabolism. As already mentioned, SKI-II was first discovered as a specific dual inhibitor of SK1 and SK2 with a Ki of 16 µM for SK1. A few years later, Cingolani *et al* provided evidence that SKI-II inhibits the desaturase 1, a very important enzyme of the *de novo* sphingolipid pathway, with a Ki (0.3 µM)[118]. Noack *et al.* showed that the use of 10 µM SKI-II led to a significant increase in dihydrosphingolipids levels and a strong decrease in S1P production, in line with the capacity of the inhibitor to affect, at that concentration, the enzymatic activities of both SK1 and DES1[119]. In the present study, treatment with 2.66 µM SKI-II did not cause these alterations. The data rather suggest that SKI-II at this low concentration mostly affects the desaturase as indicated by the reduced ratio of ceramide/dihydrosphingosine in both oxygen conditions, and leads to ceramide decrease. It might only mildly affect the sphingosine kinase, leading to modest decrease in S1P. The comparable profile of the levels in ceramide and its metabolites after treatments suggests that the metabolic flux between these sphingolipids is not affected and that the S1P decrease can be interpreted as the result of the lower amount of ceramide available for sphingosine generation. Based on these observations, I conclude that SKI-II at 2.66 µM, alone and in combination, mainly affects the desaturase and not the sphingosine kinase. The only partial depletion of S1P (a pro-survival sphingolipid) did not hinder the anti-tumor effects of the low-dose combination and might even be beneficial for cells within the parenchyma, including astrocytes, neurons and tumor-associated cells. Extracellular S1P release by dying cells was reported to serve as a signal for macrophages to phagocytose these dying cells [120]. Suppression of sphingosine kinase in activated microglia was reported to decrease their pro-inflammatory activities [121], which are desirable to eliminate tumor cells. Thus, strategies that would preserve a low level of SK activity, such as the use of low SKI-II doses, might contribute to an environment that is not only protective to healthy cells, but also supportive to immune cells through the facilitation of their phagocytic and pro-inflammatory response. This suggests that the combination might be applied together with immunotherapies designed to promote the anti-tumor activities of tumor-associated microglia/macrophages.

Oxidative stress seems to have an essential role in cell death induced by the combination of TMZ and SKI-II, as shown by their peroxynitrite-dependent effects on ER stress and viability. However, whereas the NCH82 cells treated with the higher dose (TMZ+SKI-II) combination increased their autophagic flux and died by caspase-dependent apoptosis [122], cells treated with the lower dose combination showed no alteration in the autophagic flux and polarization of mitochondria and died

through a caspase-independent, potentially non-apoptotic, form of cell death. The lack of accumulation of dihydrosphingolipids in the low-dose combination could correlate with the absence of changes in the autophagic flux. Several studies report autophagy induction by dihydrosphingosine and dihydroceramide [123]. Apoptosis and autophagy were shown to be induced as a linear function of TMZ dose when MGMT is lacking [124]. Therefore, the difference in the dose of TMZ used in our studies (48 µM vs 500 µM) have likely contributed to the dissimilarities observed in autophagy and cell death mechanisms. The lack of PI-positive/Annexin V-negative NCH82 cells suggests that membrane integrity is kept, and primary necrosis can be ruled out. The increase in the percentage of Annexin V-positive cells over time in all conditions (except in the vehicle control) demonstrates that phosphatidylserine (PS) exposure is a morphological feature induced by SKI-II and TMZ. Exposure of PS is mediated via scramblases, which are activated by caspase 3/7 cleavage. However, caspase-independent mechanisms of PS exposure were also described in non-apoptotic forms of cell death [125]. Namely, PS exposure was shown to occur due to sustained increase in the concentration of cytoplasmic calcium in a form of paraptosis [126]. The appearance of extensive cytoplasmic vacuolization, ER dilation, and lack of caspase activation and mitochondrial depolarization suggests that the low-dose (TMZ + SKI-II) combination could induce a paraptosis-like cell death in NCH82 cells [127]. Although plausible, this conclusion is a hypothesis that will have to be proven.

The mechanism underlying oxidative stress induction by SKI-II in our experimental system is unclear. Sphingolipids are able to regulate cellular redox homeostasis: ceramide can activate NADPH oxidase, supporting peroxynitrite formation [128]; whereas glucosylceramide can inhibit it [129]. I observed a decrease of C16- and C24-ceramide, ceramide-1-phosphate and sphingomyelin in both oxygen conditions. A decreased level of C16-ceramide has been related to ER stress induction as it can promote Ca2+ release from the ER and activate the ATF6/CHOP axis [130]. S1P, which is still produced under treatment with the combination, might contribute to oxidative stress through interaction with its ligand, S1PR1. Indeed, activation of S1PR1 was reported to support peroxynitrite formation by increasing the generation of NADPH oxidase-derived superoxide and nitric oxide synthase-derived nitric oxide [131]. The role of S1P and its receptor in the response of the tumor cells to the combination remains to be elucidated.

7. CONCLUSION

Cancer, as one of the main leading causes of death globally, represents an important public health concern. Experience of the past decades shows that monotherapies offer limited efficacy due to rapidly emerging resistance. Combinatorial treatment strategies have been increasingly explored to target key cancer hallmarks, such as hypoxia, angiogenesis and stemness, and improve patient outcomes.

In the present study, I explored the benefits of combining two drugs affecting two different biological processes to demonstrate, at a preclinical level, the value of the sphingolipid metabolism as a target for cancer therapy, alone and in combination with temozolomide (TMZ), the first-line agent in glioblastoma therapy. Given their key role in controlling cell fate, sphingosine kinases are prime targets to modulate sphingolipid metabolism and have been the focus of many *in vitro* and *in vivo* studies in the past twenty years [63]. However, SK inhibitors have scarcely been implemented in clinical trials and, to paraphrase Gault et al., they are “still benched on (their) way to the bedside”[132]. One explanation may lie in the contradictory data that have been reported on the cytotoxic activities of SK inhibitors on various tumor cell models, thus diminishing their potential value. Or due to the lack of existing selective and potent inhibitors with favorable pharmacodynamics/pharmacokinetics.

With the present data, I hope to raise interest for the sphingolipid metabolism as a relevant and attractive therapeutic strategy. Indeed, I provide evidence that modulation of sphingolipid metabolism, combined with the use of TMZ, has the potential to affect various biological functions of differentiated and stem-like glioblastoma cells under lower oxygen concentrations. These observations warrant further research to assess the clinical potential of such a combination to reduce the glioblastoma stem cell population in tumors and prevent relapse.

8. REFERENCES

1. Wesseling, P., Kros, J. M. & Jeuken, J. W. M. The pathological diagnosis of diffuse gliomas: Towards a smart synthesis of microscopic and molecular information in a multidisciplinary context. *Diagn Histopathol* **17**, 486–494 (2011).
2. Louis, D. N. *et al.* The 2016 World Health Organization Classification of Tumors of the Central Nervous System: a summary. *Acta Neuropathol* **131**, 803–820 (2016).
3. Louis, D. N. *et al.* The 2007 WHO classification of tumours of the central nervous system. *Acta Neuropathol* **114**, 97–109 (2007).
4. Louis, D. N. *et al.* The 2016 World Health Organization Classification of Tumors of the Central Nervous System: a summary. *Acta Neuropathol* **131**, 803–820 (2016).
5. Ohgaki, H. & Kleihues, P. The definition of primary and secondary glioblastoma. *Clinical Cancer Research* **19**, 764–772 (2013).
6. Yan, H. *et al.* IDH1 and IDH2 mutations in gliomas. *New England Journal of Medicine* **360**, 765–773 (2009).
7. Ostrom, Q. T. *et al.* CBTRUS Statistical Report: Primary Brain and Other Central Nervous System Tumors Diagnosed in the United States in 2012-2016. *Neuro Oncol* **21**, v1–v100 (2019).
8. Shukla, G. *et al.* Advanced magnetic resonance imaging in glioblastoma: A review. *Chin Clin Oncol* **6**, 1–12 (2017).
9. Waitkus, M. S., Diplas, B. H. & Yan, H. Isocitrate dehydrogenase mutations in gliomas. *Neuro Oncol* **18**, 16–26 (2016).
10. Krell, D. *et al.* Screen for IDH1, IDH2, IDH3, D2HGDH and l2HGDH mutations in glioblastoma. *PLoS One* **6**, 3–6 (2011).
11. Waitkus, M. S., Diplas, B. H. & Yan, H. Isocitrate dehydrogenase mutations in gliomas. *Neuro Oncol* **18**, 16–26 (2016).
12. Dang, L. *et al.* Cancer-associated IDH1 mutations produce 2-hydroxyglutarate. *Nature* **462**, 739–744 (2009).
13. Chowdhury, R. *et al.* The oncometabolite 2-hydroxyglutarate inhibits histone lysine demethylases. *EMBO Rep* **12**, 463–469 (2011).
14. Noushmehr, H. *et al.* Identification of a CpG Island Methylator Phenotype that Defines a Distinct Subgroup of Glioma. *Cancer Cell* **17**, 510–522 (2010).
15. Turcan, S. *et al.* IDH1 mutation is sufficient to establish the glioma hypermethylator phenotype. *Nature* **483**, 479–483 (2012).

16. Lu, C. *et al.* IDH mutation impairs histone demethylation and results in a block to cell differentiation. *Nature* **483**, 474–478 (2012).
17. Nomura, M. *et al.* DNA demethylation is associated with malignant progression of lower-grade gliomas. *Sci Rep* **9**, 1–12 (2019).
18. Freije, W. A. *et al.* Gene expression profiling of gliomas strongly predicts survival. *Cancer Res* **64**, 6503–6510 (2004).
19. Nutt, C. L. *et al.* Gene expression-based classification of malignant gliomas correlates better with survival than histological classification. *Cancer Res* **63**, 1602–1607 (2003).
20. Brennan, C. W. *et al.* The somatic genomic landscape of glioblastoma. *Cell* **155**, 462 (2013).
21. Phillips, H. S. *et al.* Molecular subclasses of high-grade glioma predict prognosis, delineate a pattern of disease progression, and resemble stages in neurogenesis. *Cancer Cell* **9**, 157–173 (2006).
22. Kim, E. L. *et al.* Intratumoral heterogeneity and longitudinal changes in gene expression predict differential drug sensitivity in newly diagnosed and recurrent glioblastoma. *Cancers (Basel)* **12**, (2020).
23. Verhaak, R. G. W. *et al.* Integrated Genomic Analysis Identifies Clinically Relevant Subtypes of Glioblastoma Characterized by Abnormalities in PDGFRA, IDH1, EGFR, and NF1. *Cancer Cell* **17**, 98–110 (2010).
24. Gill, B. J. *et al.* MRI-localized biopsies reveal subtype-specific differences in molecular and cellular composition at the margins of glioblastoma. *Proc Natl Acad Sci U S A* **111**, 12550–12555 (2014).
25. Wang, Q. *et al.* Tumor Evolution of Glioma-Intrinsic Gene Expression Subtypes Associates with Immunological Changes in the Microenvironment. *Cancer Cell* **32**, 42–56 (2017).
26. Noushmehr, H. *et al.* Identification of a CpG Island Methylator Phenotype that Defines a Distinct Subgroup of Glioma. *Cancer Cell* **17**, 510–522 (2010).
27. Verhaak, R. G. W. *et al.* Integrated Genomic Analysis Identifies Clinically Relevant Subtypes of Glioblastoma Characterized by Abnormalities in PDGFRA, IDH1, EGFR, and NF1. *Cancer Cell* **17**, 98–110 (2010).
28. Wang, Q. *et al.* Tumor Evolution of Glioma-Intrinsic Gene Expression Subtypes Associates with Immunological Changes in the Microenvironment. *Cancer Cell* **32**, 42–56 (2017).
29. Stupp, R., Mason, W. P. & van den Bent, M. J. “Radiotherapy plus Concomitant and Adjuvant Temozolomide for Glioblastoma”. *Oncology Times* **27**, 15–16 (2005).

30. Chen, L. *et al.* Glioblastoma recurrence patterns near neural stem cell regions. *Radiotherapy and Oncology* **116**, 294–300 (2015).
31. Weller, M. *et al.* European Association for Neuro-Oncology (EANO) guideline on the diagnosis and treatment of adult astrocytic and oligodendroglial gliomas. *Lancet Oncol* **18**, e315–e329 (2017).
32. Park, J. K. *et al.* Scale to predict survival after surgery for recurrent glioblastoma multiforme. *Journal of Clinical Oncology* **28**, 3838–3843 (2010).
33. Mann, J., Ramakrishna, R., Magge, R. & Wernicke, A. G. Advances in radiotherapy for glioblastoma. *Front Neurol* **8**, 1–11 (2018).
34. Shah, J. L. *et al.* Stereotactic radiosurgery and hypofractionated radiotherapy for glioblastoma. *Neurosurgery* **82**, 24–34 (2018).
35. Westphal, M. *et al.* A phase 3 trial of local chemotherapy with biodegradable carmustine (BCNU) wafers (Gliadel wafers) in patients with primary malignant glioma. *Neuro Oncol* **5**, 79–88 (2003).
36. Kreisl, T. N. *et al.* Phase II trial of single-agent bevacizumab followed by bevacizumab plus irinotecan at tumor progression in recurrent glioblastoma. *Journal of Clinical Oncology* **27**, 740–745 (2009).
37. Friedman, H. S. *et al.* Bevacizumab alone and in combination with irinotecan in recurrent glioblastoma. *Journal of Clinical Oncology* **27**, 4733–4740 (2009).
38. Desjardins, A. *et al.* Bevacizumab and daily temozolomide for recurrent glioblastoma. *Cancer* **118**, 1302–1312 (2012).
39. Gilbert, M. R. *et al.* A randomized trial of bevacizumab for newly diagnosed glioblastoma. *New England Journal of Medicine* **370**, 699–708 (2014).
40. Rominiyi, O. *et al.* Tumour treating fields therapy for glioblastoma: current advances and future directions. *British Journal of Cancer* vol. 124 697–709 Preprint at https://doi.org/10.1038/s41416-020-01136-5 (2021).
41. Lopes, I. C., De Oliveira, S. C. B. & Oliveira-Brett, A. M. Temozolomide chemical degradation to 5-aminoimidazole-4-carboxamide - Electrochemical study. *Journal of Electroanalytical Chemistry* **704**, 183–189 (2013).
42. Beranek, D. T. Distribution of methyl and ethyl adducts following alkylation with monofunctional alkylating agents. *Mutation Research - Fundamental and Molecular Mechanisms of Mutagenesis* **231**, 11–30 (1990).

43. Quiros, S., Roos, W. P. & Kaina, B. Processing of O6-methylguanine into DNA double-strand breaks requires two rounds of replication whereas apoptosis is also induced in subsequent cell cycles. *Cell Cycle* **9**, 168–178 (2010).
44. Friedman, H. S., Kerby, T. & Calvert, H. Temozolomide and treatment of malignant glioma. *Clinical Cancer Research* **6**, 2585–2597 (2000).
45. Erecińska, M. & Silver, I. A. Tissue oxygen tension and brain sensitivity to hypoxia. *Respir Physiol* **128**, 263–276 (2001).
46. Beppu, T. *et al.* Change of Oxygen Pressure in Glioblastoma Tissue Under Various Conditions. *J Neurooncol* **58**, 47–52 (2002).
47. Brat, D. J. *et al.* Pseudopalisades in Glioblastoma Are Hypoxic, Express Extracellular Matrix Proteases, and Are Formed by an Actively Migrating Cell Population. *Cancer Res* **64**, 920–927 (2004).
48. Auffinger, B. *et al.* Conversion of differentiated cancer cells into cancer stem-like cells in a glioblastoma model after primary chemotherapy. *Cell Death Differ* **21**, 1119–1131 (2014).
49. Wang, P., Wan, W., Xiong, S.-L., Feng, H. & Wu, N. Cancer stem-like cells can be induced through dedifferentiation under hypoxic conditions in glioma, hepatoma and lung cancer. *Cell Death Discov* **3**, 16105 (2017).
50. Marzagalli, M., Fontana, F., Raimondi, M. & Limonta, P. Cancer stem cells—key players in tumor relapse. *Cancers (Basel)* **13**, 1–23 (2021).
51. Heffernan-Stroud, L. A. & Obeid, L. M. *Sphingosine Kinase 1 in Cancer*. *Advances in Cancer Research* vol. 117 (Elsevier Inc., 2013).
52. Zhang, H. *et al.* Sphingosine-1-phosphate, a novel lipid, involved in cellular proliferation. *Journal of Cell Biology* **114**, 155–167 (1991).
53. Obeid, L. M., Linardic, C. M., Karolak, L. A. & Hannun, Y. A. Programmed cell death induced by ceramide. *Science (1979)* **259**, 1769–1771 (1993).
54. Giussani, P., Tringali, C., Riboni, L., Viani, P. & Venerando, B. Sphingolipids: Key regulators of apoptosis and pivotal players in cancer drug resistance. *Int J Mol Sci* **15**, 4356–4392 (2014).
55. Abuhusain, H. J. *et al.* A metabolic shift favoring sphingosine 1-phosphate at the expense of ceramide controls glioblastoma angiogenesis. *Journal of Biological Chemistry* **288**, 37355–37364 (2013).
56. Bose, R. *et al.* Ceramide synthase mediates daunorubicin-induced apoptosis: An alternative mechanism for generating death signals. *Cell* **82**, 405–414 (1995).

57. Kitatani, K., Idkowiak-Baldys, J. & Hannun, Y. A. The sphingolipid salvage pathway in ceramide metabolism and signaling. *Cell Signal* **20**, 1010–1018 (2008).
58. Dickson, M. A. *et al.* A phase I clinical trial of safingol in combination with cisplatin in advanced solid tumors. *Clin Cancer Res* **17**, 2484–92 (2011).
59. Schwartz, G. K. *et al.* A pilot clinical/pharmacological study of the protein kinase C-specific inhibitor safingol alone and in combination with doxorubicin. *Clin Cancer Res* **3**, 537–43 (1997).
60. French, K. J. *et al.* Antitumor Activity of Sphingosine Kinase Inhibitors. *Journal of Pharmacology and Experimental Therapeutics* **318**, 596–603 (2006).
61. Cingolani, F. *et al.* Inhibition of dihydroceramide desaturase activity by the sphingosine kinase inhibitor SKI II. *The Journal of Lipid Research* **55**, 1711–1720 (2014).
62. Gao, P., Peterson, Y. K., Smith, R. A. & Smith, C. D. Characterization of isoenzyme-selective inhibitors of human sphingosine kinases. *PLoS One* **7**, (2012).
63. Cao, M. *et al.* Sphingosine kinase inhibitors: A patent review. *Int J Mol Med* **41**, 2450–2460 (2018).
64. Yan, G., Elbadawi, M. & Efferth, T. Multiple cell death modalities and their key features (Review). *World Academy of Sciences Journal* vol. 2 39–48 Preprint at https://doi.org/10.3892/wasj.2020.40 (2020).
65. Kerr, J. F. R., Wyllie, A. H. & Currie, A. R. *Apoptosis: A Basic Biological Phenomenon with Wide-Ranging Implications in Tissue Kinetics. Br. J. Cancer* vol. 26 (1972).
66. Galluzzi, L. *et al.* Molecular mechanisms of cell death: Recommendations of the Nomenclature Committee on Cell Death 2018. *Cell Death Differ* **25**, 486–541 (2018).
67. Karcher, S. *et al.* Different angiogenic phenotypes in primary and secondary glioblastomas. *Int J Cancer* **118**, 2182–2189 (2006).
68. Barrantes-Freer, A. *et al.* Human glioma-initiating cells show a distinct immature phenotype resembling but not identical to NG2 glia. *J Neuropathol Exp Neurol* **72**, 307–324 (2013).
69. Xie, Y. *et al.* The Human Glioblastoma Cell Culture Resource: Validated Cell Models Representing All Molecular Subtypes. *EBioMedicine* **2**, 1351–1363 (2015).
70. Knizhnik, A. V. *et al.* Survival and Death Strategies in Glioma Cells: Autophagy, Senescence and Apoptosis Triggered by a Single Type of Temozolomide-Induced DNA Damage. *PLoS One* **8**, 1–12 (2013).
71. Roos, W. P. *et al.* Apoptosis in malignant glioma cells triggered by the temozolomide-induced DNA lesion O6-methylguanine. *Oncogene* **26**, 186–197 (2007).

72. Vichai, V. & Kirtikara, K. Sulforhodamine B colorimetric assay for cytotoxicity screening. *Nat Protoc* **1**, 1112–1116 (2006).
73. Chou, T. C. & Talalay, P. Quantitative analysis of dose-effect relationships: the combined effects of multiple drugs or enzyme inhibitors. *Adv Enzyme Regul* **22**, 27–55 (1984).
74. Chou, T. C. Drug combination studies and their synergy quantification using the chou-talalay method. *Cancer Res* **70**, 440–446 (2010).
75. Chou, T. C. Preclinical versus clinical drug combination studies. *Leuk Lymphoma* **49**, 2059–2080 (2008).
76. Chou, T. & Martin, N. CompuSyn for Drug Combinations: PC Software and User's Guide: A Computer Program for Quantitation of Synergism and Antagonism in Drug Combinations, and the Determination of IC50 and ED50 and LD50 Values. Preprint at (2005).
77. Hu, Y. & Smyth, G. K. ELDA: Extreme limiting dilution analysis for comparing depleted and enriched populations in stem cell and other assays. *J Immunol Methods* **347**, 70–78 (2009).
78. Cisneros Castillo, L. R. *et al.* Evaluation of Consistency in Spheroid Invasion Assays. *Sci Rep* **6**, 28375 (2016).
79. Cisneros Castillo, L. R., Oancea, A.-D., Stüllein, C. & Régnier-Vigouroux, A. A Novel Computer-Assisted Approach to evaluate Multicellular Tumor Spheroid Invasion Assay. *Sci Rep* **6**, 35099 (2016).
80. Marion M.Bradford. A rapid and sensitive method for the quantitation of microgram quantities of protein utilizing the principle of protein-dye binding. *Anal Biochem* **72**, 248–254 (1976).
81. Post, J. M. *et al.* Lipidomics and Transcriptomics in Neurological Diseases. *J Vis Exp* (2022) doi:10.3791/59423.
82. Lerner, R., Cuadrado, D. P., Post, J. M., Lutz, B. & Bindila, L. Broad lipidomic and transcriptional changes of prophylactic pea administration in adult mice. *Front Neurosci* **13**, 1–16 (2019).
83. Chou, T. C. Drug combination studies and their synergy quantification using the chou-talalay method. *Cancer Res* **70**, 440–446 (2010).
84. Noack, J., Choi, J., Richter, K., Kopp-Schneider, A. & Régnier-Vigouroux, A. A sphingosine kinase inhibitor combined with temozolomide induces glioblastoma cell death through accumulation of dihydrosphingosine and dihydroceramide, endoplasmic reticulum stress and autophagy. *Cell Death Dis* **5**, e1425 (2014).

85. Christensen, M. E., Jansen, E. S., Sanchez, W. & Waterhouse, N. J. Flow cytometry based assays for the measurement of apoptosis-associated mitochondrial membrane depolarisation and cytochrome c release. *Methods* **61**, 138–145 (2013).
86. Würstle, S. *et al.* Temozolomide induces autophagy in primary and established glioblastoma cells in an EGFR independent manner. *Oncol Lett* **14**, 322–328 (2017).
87. Klionsky DJ, Abdelmohsen K, Abe A, Abedin MJ, Abeliovich H, Acevedo Arozena A, Adachi H, Adams CM, Adams PD, Adeli K, Adhihetty PJ, Adler SG, Agam G, Agarwal R, Aghi MK, Agnello M, Agostinis P, Aguilar PV, Aguirre-Ghiso J, Airoldi EM, Ait-Si-Ali S, Akemat, Z. SM. Guidelines for use and interpretation of assays for monitoring autophagy (3rd edition). *Autophagy* **12**, 1–222 (2016).
88. Burton, T. R., Henson, E. S., Baijal, P., Eisenstat, D. & Gibson, S. B. The pro-cell death Bcl-2 family member, BNIP3, is localized to the nucleus of human glial cells: Implications for glioblastoma multiforme tumor cell survival under hypoxia. *Int J Cancer* **118**, 1660–1669 (2006).
89. Bellot, G. *et al.* Hypoxia-Induced Autophagy Is Mediated through Hypoxia-Inducible Factor Induction of BNIP3 and BNIP3L via Their BH3 Domains. *Mol Cell Biol* **29**, 2570–2581 (2009).
90. Shubin, A. V., Demidyuk, I. V., Komissarov, A. A., Rafieva, L. M. & Kostrov, S. V. Cytoplasmic vacuolization in cell death and survival. *Oncotarget* **7**, 55863–55889 (2016).
91. Arismendi-Morillo, G. Electron microscopy morphology of the mitochondrial network in gliomas and their vascular microenvironment. *Biochim Biophys Acta Bioenerg* **1807**, 602–608 (2011).
92. Santos, C. X. C., Tanaka, L. Y., Wosniak, J. & Laurindo, F. R. M. Mechanisms and Implications of Reactive Oxygen Species Generation During the Unfolded Protein Response: Roles of Endoplasmic Reticulum Oxidoreductases, Mitochondrial Electron Transport, and NADPH Oxidase. *Antioxid Redox Signal* **11**, 2409–2427 (2009).
93. Dickhout, J. G. *et al.* Peroxynitrite causes endoplasmic reticulum stress and apoptosis in human vascular endothelium: Implications in atherogenesis. *Arterioscler Thromb Vasc Biol* **25**, 2623–2629 (2005).
94. Mahajan-Thakur, S., Bien-Möller, S., Marx, S., Schroeder, H. & Rauch, B. H. Sphingosine 1-phosphate (S1P) signaling in glioblastoma multiforme—A systematic review. *Int J Mol Sci* **18**, 1–17 (2017).
95. Ryser, M. F. *et al.* S1P1 Overexpression Inhibits SDF1/CXCR4 Dependent Migration and In Vivo Homing of Hematopoietic Stem Cells. *Blood* **106**, 2188–2188 (2005).

96. Sanna, M. G. *et al.* Enhancement of capillary leakage and restoration of lymphocyte egress by a chiral S1P1 antagonist in vivo. *Nat Chem Biol* **2**, 434–441 (2006).
97. Barrantes-Freer, A. *et al.* Human glioma-initiating cells show a distinct immature phenotype resembling but not identical to NG2 glia. *J Neuropathol Exp Neurol* **72**, 307–324 (2013).
98. van Nifterik, K. a *et al.* Absence of the MGMT protein as well as methylation of the MGMT promoter predict the sensitivity for temozolomide. *Br J Cancer* **103**, 29–35 (2010).
99. Ostermann, S. *et al.* Plasma and cerebrospinal fluid population pharmacokinetics of temozolomide in malignant glioma patients. *Clinical Cancer Research* **10**, 3728–3736 (2004).
100. Rosso, L. *et al.* A new model for prediction of drug distribution in tumor and normal tissues: Pharmacokinetics of temozolomide in glioma patients. *Cancer Res* **69**, 120–127 (2009).
101. Di Piazza, M. *et al.* Cytosolic Activation of Cathepsins Mediates Parvovirus H-1-Induced Killing of Cisplatin and TRAIL-Resistant Glioma Cells. *J Virol* **81**, 4186–4198 (2007).
102. Hermisson, M. *et al.* O6-methylguanine DNA methyltransferase and p53 status predict temozolomide sensitivity in human malignant glioma cells. *J Neurochem* **96**, 766–776 (2006).
103. Inaba, N. *et al.* The effect of PTEN on proliferation and drug-, and radiosensitivity in malignant glioma cells. *Anticancer Res* **31**, 1653–1658 (2011).
104. Singh, N., Miner, A., Hennis, L. & Mittal, S. Mechanisms of temozolomide resistance in glioblastoma - a comprehensive review. *Cancer Drug Resistance* **4**, 17–43 (2021).
105. Chiche, J. *et al.* Hypoxia-inducible carbonic anhydrase IX and XII promote tumor cell growth by counteracting acidosis through the regulation of the intracellular pH. *Cancer Res* **69**, 358–368 (2009).
106. Proescholdt, M. A. *et al.* Function of carbonic anhydrase IX in glioblastoma multiforme. *Neuro Oncol* **14**, 1357–1366 (2012).
107. Ader, I., Brizuela, L., Bouquerel, P., Malavaud, B. & Cuvillier, O. Sphingosine Kinase 1: A New Modulator of Hypoxia Inducible Factor 1 during Hypoxia in Human Cancer Cells. *Cancer Res* **68**, 8635–8642 (2008).
108. Auffinger, B. *et al.* Conversion of differentiated cancer cells into cancer stem-like cells in a glioblastoma model after primary chemotherapy. *Cell Death Differ* **21**, 1119–1131 (2014).
109. Wang, P., Wan, W., Xiong, S.-L., Feng, H. & Wu, N. Cancer stem-like cells can be induced through dedifferentiation under hypoxic conditions in glioma, hepatoma and lung cancer. *Cell Death Discov* **3**, 16105 (2017).

110. Quiros, S., Roos, W. P. & Kaina, B. Processing of O6-methylguanine into DNA double-strand breaks requires two rounds of replication whereas apoptosis is also induced in subsequent cell cycles. *Cell Cycle* **9**, 168–178 (2010).
111. Perillo, B. *et al.* ROS in cancer therapy: the bright side of the moon. *Exp Mol Med* **52**, 192–203 (2020).
112. Campos-Sandoval, J. A. *et al.* Antioxidant responses related to temozolomide resistance in glioblastoma. *Neurochem Int* **149**, 105136 (2021).
113. Trachootham, D., Alexandre, J. & Huang, P. Targeting cancer cells by ROS-mediated mechanisms: a radical therapeutic approach? *Nat Rev Drug Discov* **8**, 579–591 (2009).
114. Beider, K. *et al.* The sphingosine-1-phosphate modulator FTY720 targets multiple myeloma via the CXCR4/CXCL12 pathway. *Clinical Cancer Research* **23**, 1733–1747 (2017).
115. Wang, S. *et al.* The CXCL12/CXCR4 axis confers temozolomide resistance to human glioblastoma cells via up-regulation of FOXM1. *J Neurol Sci* **414**, 116837 (2020).
116. Yoshida, Y. *et al.* The expression level of sphingosine-1-phosphate receptor type 1 is related to MIB-1 labeling index and predicts survival of glioblastoma patients. *J Neurooncol* **98**, 41–47 (2010).
117. Bien-Möller, S. *et al.* Expression of S1P metabolizing enzymes and receptors correlate with survival time and regulate cell migration in glioblastoma multiforme. *Oncotarget* **7**, 13031–13046 (2016).
118. Cingolani, F. *et al.* Inhibition of dihydroceramide desaturase activity by the sphingosine kinase inhibitor SKI II. *The Journal of Lipid Research* **55**, 1711–1720 (2014).
119. Noack, J., Choi, J., Richter, K., Kopp-Schneider, A. & Régnier-Vigouroux, A. A sphingosine kinase inhibitor combined with temozolomide induces glioblastoma cell death through accumulation of dihydrosphingosine and dihydroceramide, endoplasmic reticulum stress and autophagy. *Cell Death Dis* **5**, e1425 (2014).
120. Gude, D. R. *et al.* Apoptosis induces expression of sphingosine kinase 1 to release sphingosine-1-phosphate as a “come-and-get-me” signal. *The FASEB Journal* **22**, 2629–2638 (2008).
121. Wang, P., Wan, W. W., Xiong, S. L., Feng, H. & Wu, N. Cancer stem-like cells can be induced through dedifferentiation under hypoxic conditions in glioma, hepatoma and lung cancer. *Cell Death Discov* **3**, 132–144 (2017).
122. Noack, J., Choi, J., Richter, K., Kopp-Schneider, A. & Régnier-Vigouroux, A. A sphingosine kinase inhibitor combined with temozolomide induces glioblastoma cell death through

accumulation of dihydrosphingosine and dihydroceramide, endoplasmic reticulum stress and autophagy. *Cell Death Dis* **5**, e1425 (2014).

123. Siddique, M. M., Li, Y., Chaurasia, B., Kaddai, V. A. & Summers, S. A. Dihydroceramides: From bit players to lead actors. *Journal of Biological Chemistry* **290**, 15371–15379 (2015).
124. He, Y. & Kaina, B. Are there thresholds in glioblastoma cell death responses triggered by temozolomide? *Int J Mol Sci* **20**, (2019).
125. Ferraro-Peyret, C., Quemeneur, L., Flacher, M., Revillard, J.-P. & Genestier, L. Caspase-Independent Phosphatidylserine Exposure During Apoptosis of Primary T Lymphocytes. *The Journal of Immunology* **169**, 4805–4810 (2002).
126. Jambrina, E. *et al.* Calcium influx through receptor-operated channel induces mitochondria-triggered paraptotic cell death. *Journal of Biological Chemistry* **278**, 14134–14145 (2003).
127. Sperandio, S., De Belle, I. & Bredesen, D. E. An alternative, nonapoptotic form of programmed cell death. *Proc Natl Acad Sci U S A* **97**, 14376–14381 (2000).
128. Zhang, D. X., Zou, A. ping & Li, P. lan. Ceramide-induced activation of NADPH oxidase and endothelial dysfunction in small coronary arteries. *Am J Physiol Heart Circ Physiol* **284**, (2003).
129. Barth, B. M. *et al.* Inhibition of NADPH oxidase by glucosylceramide confers chemoresistance. *Cancer Biol Ther* **10**, 1126–1136 (2010).
130. Senkal, C. E., Ponnusamy, S., Bielawski, J., Hannun, Y. A. & Ogretmen, B. Antiapoptotic roles of ceramide-synthase-6-generated C 16 -ceramide via selective regulation of the ATF6/ CHOP arm of ER-stress-response pathways . *The FASEB Journal* **24**, 296–308 (2010).
131. Doyle, T., Finley, A., Chen, Z. & Salvemini, D. Role for peroxynitrite in sphingosine-1-phosphate-induced hyperalgesia in rats. *Pain* **152**, 643–648 (2011).
132. Gault, C. R. & Obeid, L. M. Still Benched on its Way to the Bedside: Sphingosine Kinase 1 as an Emerging Target in Cancer Chemotherapy. *Crit Rev Biochem Mol Biol* **46**, 342–351 (2011).

Acronyms and Abbreviations

AV	AnnexinV
BA1	Bafilomycin A1
BiP	Binding immunoglobulin protein
BNIP3	BCL2 interacting protein 3
C1P	Ceramide-1-phosphate
Cer	Ceramide
CerS	Ceramide synthase
CHOP	C/EBP homologous protein
CI	Combination index
CPT	Camptothecin
DES1	Dihydroceramide desaturase 1
DMSO	Dimethyl sulfoxide
DRI	Dose reduction index
ED50	Median effect dose
ELDA	Extreme limiting dilution analysis
ER	Endoplasmic reticulum
FCCP	Carbonyl cyanide-p-trifluoromethoxyphenylhydrazone
FeTPPS	5,10,15,20-Tetrakis(4-Sulfonatophenyl)porphyrinato-Eisen (III)
FITC	Fluorescein isothiocyanate
FSC	Forward scatter
GB	Glioblastoma
GRP78	Glucose regulatory protein 78
GSC	Glioblastoma stem cell
LC3	Microtubule-associated protein 1A/1B-light chain 3
MFI	Median fluorescence intensity
MGMT	O^6-methylguanine-DNA methyltransferase
MMP	Mitochondrial membrane potential
NADPH	Nicotinamide adenine dinucleotide phosphate
PI	Propidium iodide
PS	Phosphatidylserine
PTEN	Phosphatase and tensin homologue
S1P	Sphingosine-1-phosphate
S1PR	Sphingosine-1-phosphate receptor
SD	Standard deviation
SK	Sphingosine kinase

SKI	Sphingosine kinase inhibitor
SKI-II	Dual sphingosine kinase inhibitor
SRB	Sulforhodamine B
SSC	Side scatter
ROS	Reactive oxygen species
TEM	Transmission electron microscopy
TMRE	Tetramethylrhodamine ethyl ester
TMZ	Temozolomide
UPR	Unfolded protein response
zVAD	Z-VAD-FMK

Index of Figures

Index of Tables

Acknowledgements

First and foremost, I would like to thank Anne Régnier-Vigouroux for the opportunity to conduct my doctoral studies in her lab and all support throughout this journey. Thank you so much for believing in me, giving me the freedom to explore my ideas, the freedom to fail, and most importantly for your kindness and friendship.

Thank you to Beate Stradmann and Carsten Geiß for your support in and outside the lab. Thank you so much for your patience, kindness and for sharing your learnings with me. I've learned so much with you!

I would like to thank Ella Kim, for the collaboration, the helpful discussions and training in her lab. Thank you also to Christian Behl for accepting to be my second supervisor and sharing his learnings with me.

Last but not least, thank you to Andreas, my partner in life, for the support and motivation in bringing this thesis to the finish line. Thank you so much for taking care of our child while I was writing this thesis and for celebrating every milestone with me.

List of Publications

Sousa N, Geiß C, Bindila L, Lieberwirth I, Kim E, Régnier-Vigouroux A. Targeting sphingolipid metabolism with the sphingosine kinase inhibitor SKI-II overcomes hypoxia-induced chemotherapy resistance in glioblastoma cells: effects on cell death, self-renewal, and invasion. BMC Cancer, 23(1):762 (2023) doi: 10.1186/s12885-023-11271-w. PMID: 37587449; PMCID: PMC10433583

Granada, L., **Sousa, N**., Lopes, S. and Lemos, M. F. L. Is integrated multitrophic aquaculture the solution to the sectors' major challenges? – a review. Reviews in Aquaculture, 6, 1-18. (2015) doi: 10.1111/raq.12093. (L. Granada and N. Sousa contributed equally to this work).

Poster Presentations

Brain Tumor Meeting. Berlin, Germany, May 23-24, 2019: **Sousa, N**., Régnier-Vigouroux, A. „The sphingosine kinase inhibitor SKI-II and temozolomide synergistically suppress growth and triggers caspase-indepedent cell death in glioblastoma cells under hypoxia.

Frankfurt Cancer Conference. Frankfurt, Germany, September 25-27, 2018: **Sousa, N**.; Berte, N.; Kim, E. and Régnier-Vigouroux, A., „Effect of a sphingosine kinase inhibitor combined with temozolomide on glioblastoma cell plasticity under hypoxia".